

RIKAGAKU KENKYUSHO

the Institute of Physical and Chemical Research

Wako-shi, Saitama Pref., JAPAN

'72

IPCR cyclotron
Progress Report 1972

Vol. 6

Edited by Administration Committee of the IPCR Cyclotron

IPCR Cyclotron Progress Report

Vol. 6

The Institute of Physical and Chemical Research
"RIKAGAKU KENKYUSHO" Wako-shi, Saitama, 351 JAPAN
December, 1972

This volume contains recent information of the IPCR Cyclotron, informal reports and abstracts of papers which will be published at scientific meetings or in publications by staff members, guests, and visitors.

All rights reserved. This report or any part thereof may not be reproduced in any form (including photostatic or microfilm form) without written permission from the publisher.

CONTENTS

	Page
1. INTRODUCTION	1
2. MACHINE OPERATION	2
3. MACHINE DEVELOPMENT AND ACCELERATOR PHYSICS	
3-1. A New Irradiation System	5
3-2. Improvement of the Central Region Geometry and the Extraction Efficiency of Beam	7
3-3. Polarized Ion Source On the Construction of a Strong Field Ionizer and Measurement of Its Ionization Efficiency	12
3-4. A Proposal of New Heavy Ion Accelerator System	15
3-5. The Variable Frequency Linac Project Construction of a Model Cavity	16
3-6. The Variable Frequency Linac Project Quadrupole Magnetic Field Gradient Necessary for Focusing Very Heavy Ions	18
3-7. A Study of Heavy Ion Source for a New Accelerator	20
3-8. A Quadrupole Magnet of Compact Size	21
4. NUCLEAR PHYSICS	
Scattering and Reactions	
4-1. A Study of Transfer Reactions Induced by 90 MeV ^{14}N on ^{52}Cr	23
4-2. Selective Excitation of One Proton Configuration for ^{53}Mn in $^{52}\text{Cr}(^{14}\text{N}, ^{13}\text{C})^{53}\text{Mn}$ and $^{52}\text{Cr}(^{12}\text{C}, ^{11}\text{B})^{53}\text{Mn}$	27
4-3. Gamma Transition from the First 3^- Levels in $^{94,96,98,100}\text{Mo}$	30
4-4. Inelastic Scattering of Deutrons by Even Mo Isotopes	33
4-5. Unbound Isobaric Analog States Induced by $^{50,52,54}\text{Cr}(h,d)^{51,53,55}\text{Mn}$ Reactions	35
4-6. The DWBA and Coupled Channel Analyses of Inelastic Scattering of ^3He from ^{12}C	37

4-7.	$^{20}\text{Ne}(d, ^6\text{Li})^{16}\text{O}$ Reaction	43
4-8.	Inelastic Scattering for the Giant Resonance States	45
4-9.	Effect of Exchange Currents on Orbital g-Factors	47
4-10.	Total Energy Surface for ^{236}U in the Two-Center Model	49
4-11.	On the Mechanism of $(^3\text{He}, t)$ Reaction	53
4-12.	Coupling between Valence Nucleon and Clusterized Core	58
5.	NUCLEAR PHYSICS	
	Nuclear Spectroscopy	
5-1.	The Gamma -Decay of $^{146,150,152}\text{Sm}$ following the $(\alpha, 2n)$ Reaction	66
5-2.	Decay of ^{87}Zr and ^{85}Zr (II)	70
5-3.	Magnetic Moments of High-Spin Isomeric States in Po Isotopes	73
5-4.	A Method of Measuring Alpha -Decays in the Nanosecond Range	76
5-5.	Alpha - and Gamma -Spectroscopy of N=128 Isotones ^{216}Ra , ^{217}Ac , and ^{218}Th	80
5-6.	g-Factor Measurement of the 8^+ State in ^{86}Sr Produced in Kr Gas	84
6.	NUCLEAR INSTRUMENTATION	
6-1.	A Dual Ge(Li) Gamma-Ray Spectrometer for Nuclear Study	87
6-2.	Particle Identification Study for Z = 3 to Z = 7 Particles Using a Power-Law Type Particle Identifier	89
6-3.	On a Model of Wire Spark Chamber with Ferrite Memory Cores for Broad Range Magnetic Spectrometer	92
6-4.	Measurements of Ion Optical Properties of A Particle Analyzer by Particle Beams	96
7.	RADIOCHEMISTRY	
7-1.	The Behavior of Trace Amounts of ^{18}F Atoms Trapped on Metal Surfaces	99

7-2.	A Mössbauer Spectroscopic Study of Chemical States of ^{119}Sn after the EC Decay of ^{119}Sb in Sb_2O_3 and TeO_2	102
7-3.	A Radiochemical Study of Oxidation States of ^{119}Sb after the EC Decay of $^{119\text{m}}\text{Te}$ in TeO_2 and H_6TeO_6	104
7-4.	Radiochemical Studies on Carbon, Nitrogen, and Oxygen in Semiconductor Silicon	106
8.	RADIATION CHEMISTRY AND RADIATION BIOLOGY	
8-1.	Radiolysis of Binary Mixtures of Tetrahydrofuran and Benzene in High LET Region	108
8-2.	LET Dependence of Spatial Distribution of Free Radicals in Irradiated Crystalline Eicosane	110
8-3.	LET Effects on Bacterial Cells	114
9.	SOLID STATE PHYSICS	
9-1.	Positron Annihilation in Ferromagnetic Nickel	119
9-2.	Point Defects in Irradiated Copper and Cu_3Au	122
9-3.	Electron Microscopic Observation on Helium Bubbles in Aluminum Irradiated by Alpha -Particles	125
10.	RADIOISOTOPE PRODUCTION AND ITS APPLICATIONS	
10-1.	Production of Radioisotopes for Medical Use	127
11.	RADIATION MONITORING	
11-1.	Routine Monitoring	130
12.	LIST OF PUBLICATIONS	132
13.	LIST OF PERSONNEL	134
14.	LIST OF OUTSIDE USERS AND THEIR THEMES	137
	AUTHOR INDEX	141

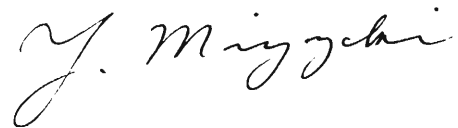
1. INTRODUCTION

In these seven years since the first beam of the cyclotron was obtained, a great number of investigations have been done in various fields of research. The accumulation of these works as well as the worldwide studies revealed that heavier particles as projectiles would become a new powerful probe to search for the regions unexplored yet. To meet the requirements of workers who want to have this new probe, a preliminary study of a new machine for heavy-ion acceleration was made two years ago as described in the 1970 report. Since then, design studies of ion sources and acceleration systems have been started and a concrete project is being drawn up. It is hoped the project will be supported and realized in the near future.

Improvements in various features of the machine are made incessantly. Among them, it should be pointed out that the polarized ion source has been constructed and its testing is now under way.

Most of the works carried out in this year are continuation from the previous year. Besides, some theoretical studies on nuclear physics are included in this report.

The Cyclotron Board has been organized in this year and the former Administration Committee was replaced by the Users' Committee. The Board is expected to facilitate the management of the research programs and the development of the new accelerator project in connection with the situation outside as well as inside of the Institute.



Yukio Miyazaki, Chairman
The Cyclotron Board

2. MACHINE OPERATION

Machine Group

During the period from Oct. 1971 to Oct. 1972 the cyclotron was operated on the 24 h a day basis as in previous years. "On beam" time had totaled 5300 h. Table 1 shows a brief statistics of the period. One-third of the beam time was used for researches using heavy ions. Table 2 shows the scheduled machine time allotment. More than 95 % of the schedule was fulfilled. Table 2 contains also such times as for periodical machine inspection and repair, ion source exchange etc. when the cyclotron stops its work.

After 5-year continuous operation for about 30000 h, some parts of the cyclotron had to be replaced or repaired. One hundred cooling water relays were replaced in the summer overhauling period by new type ones, which had passed one-year life tests. In the same period, nearly 200 rubber hoses which had been used to supply cooling water to the dee system at 1 kV DC potential were replaced by Nylon tubings. After the overhaul a drastic decrease of leakage current was observed. Less electro-deposition trouble in the cooling circuits is expected. The target holder for production of radioisotopes in the accelerating chamber was replaced by a newly designed one. A new dee voltage pick-up electrode was installed at the side of the east dee at the beginning of 1972 and had been used in parallel with the old ones. Ventilation around the ion source control panel was improved to prevent any accident by misoperation of the gas vessels. Beam pipes to each experimental area were provided with new vacuum systems.

Table 1. Machine operation time by indication of working time meter.

Date	Oscillator on	Ion source on
Oct. 1971	22118.0 (h)	24204.8 (h)
Oct. 1972	27411.0 (h)	29880.0 (h)
365 days	5293.0 (h)	5675.2 (h)
Percent of 365 days	60.5 %	66.1 %

Schedule for this period:

Machine time	214 (days)
Overhaul and installation work	40 (days)
Periodical inspection and repair	28 (days)
Vacation, holiday, and Sunday	83 (days)

Table 2. Scheduled machine time and subject of research in this period VII.

Subject	Hours	Percent
Heavy ion reaction	720	Nucl. Phys. 58.2 %
Direct reaction	1056	
In-beam spectroscopy	1200	
Radio-isotope production for nuclear spectroscopy	331	
Nuclear chemistry and radio-isotope production	286	Fields other than Nucl. Phys. 20.1 %
Radiation chemistry and radiation biology	341	
Solid state physics	365	
Mössbauer source	72	
Track detector	11	
Nuclide identification study	67	
Particle analyser calibration	168	Accelerator Phys. and Maintenance 17.7 %
Cyclotron conditioning	12	
Alignment of beam handling system	50	
Machine inspection and repair	672	
Exchange of heavy ion and ordinary ion sources	56	
Reserved for machine time adjustment	48	
Use by other organizations	228	
	5683	100.0 %

As a consequence, vacuum pressure at each channel has been improved by an order of magnitude. The diffused image of beam has disappeared, which was thought to occur in most cases from charge changing process by the residual gas molecules when heavy ions were transported to the end of a long beam pipe. The interlock system for vacuum condition described in the last year's report was installed. It is found useful to maintain a high performance of the vacuum system.

All the planning and design of these modifications have been made by the machine group and operation personnels. Detailed design and manufacturing have been done by the machine shop of this institute. Installation and adjustment have been carried out again by the machine and operation groups.

3. MACHINE DEVELOPMENT AND ACCELERATOR PHYSICS

3-1. A New Irradiation System

A. Shimamura and T. Inoue

The new irradiation system described in this report has been installed for radio-isotope production in the cyclotron chamber and can be used easily by general users without any special training. Target bases are made of copper or aluminum plates of $60 \times 80 \times 10$ mm. These plates can be replaced easily when they are contaminated with radioactive isotopes. The improved point is that the back sides of target bases are directly cooled, making efficient cooling possible. When the targets are in the cyclotron chamber, vacuum sealing of the plates is made by O-rings against water pressure. After the irradiation the remaining cooling water is driven out by air blowing and then the target is taken off. All these operations can be made remotely.

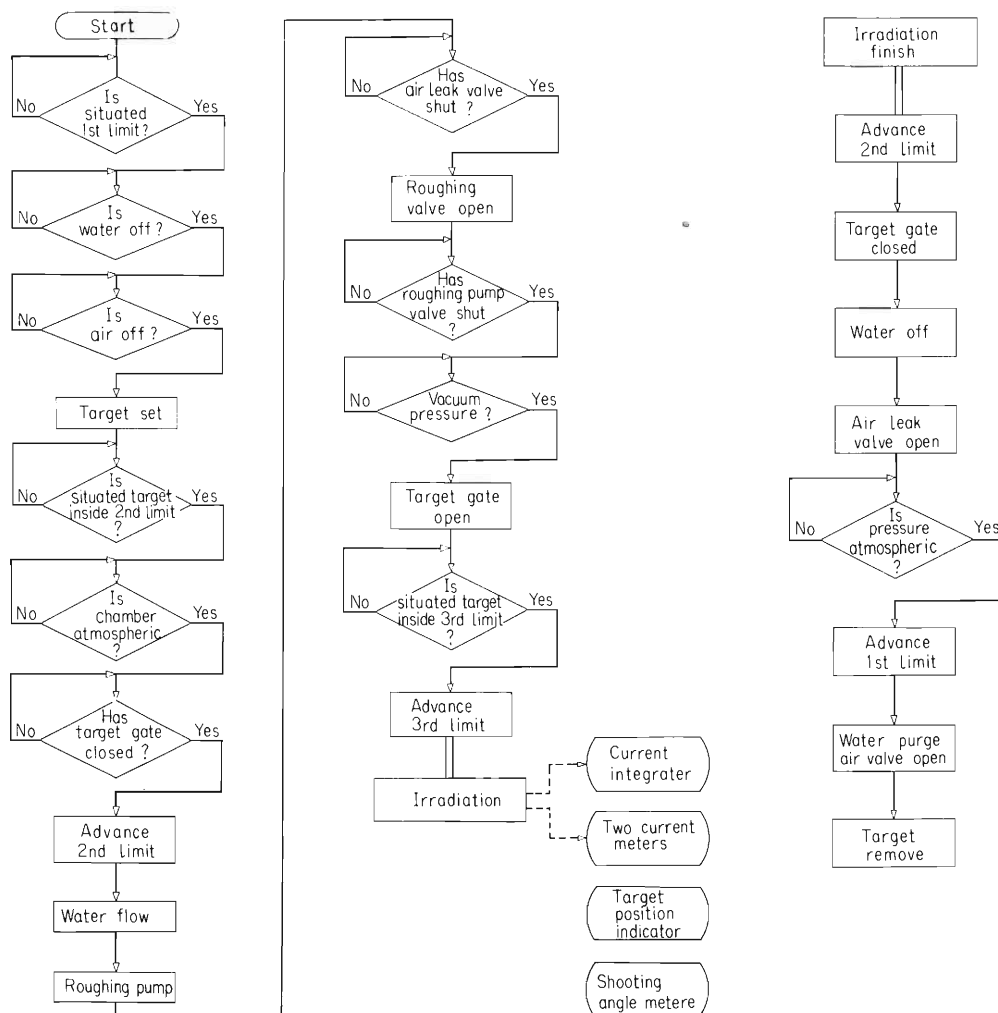


Fig. 1. Flow diagram of sequential operation of the installation.

There are two beam probes provided with slits before and behind the target. The purpose of these beam probes is to let cyclotron beam fall properly on the target. The angle of incidence of the beam on the surface of the target can be varied within $\pm 30^\circ$. Extra rotation of 270° is possible if the irradiation of the other side of the target is desired. The angle is shown on the central control panel by a position indicator. Each of the target and the beam probes are connected to a current integrator and two current meters in the central controlling sets.

The installation is operated step by step in a sequential manner. It has indispensable interlocking at each step and switching onto the next step is possible only when certain conditions of the intermediate section are satisfied. The order of operation is indicated in Fig. 1.

The controlling sets of this installation are located in the cyclotron vault and in the central control desk. One can operate them at both sites without switching the local and remote indicators. We have made the dimensions much smaller than the old one¹⁾ in order to make the space around the cyclotron larger for the convenience of exchange of ion source.

Reference

- 1) A. Hashizume and A. Shimamura: IPCR Cyclotron Progr. Rep., 1, 73 (1967).

3-2. Improvement of the Central Region Geometry and the Extraction Efficiency of Beam

Y. Miyazawa, K. Ogiwara, S. Fujita, M. Hemmi, K. Ikegami,
T. Inoue, T. Kageyama, S. Kohara, H. Nakajima,
A. Shimamura, O. Terajima, and T. Tonuma

The initial orbits in a cyclotron are crucial in determining the properties of the beam at the final orbit. Also, good positioning of the deflector channel as well as a good quality of beam at the maximum radius is necessary to obtain a good extraction efficiency.

To make its concept precise, we define the extraction efficiency as the ratio of the extracted beam current, measured at the downstream of the deflector channel, to the internal beam current measured at 66 cm radius for light ions. For heavy ions, the internal beam current is measured at 70 cm radius rather than at 66 cm because the internal beam current decreases with the radius by the charge exchange loss during the acceleration.

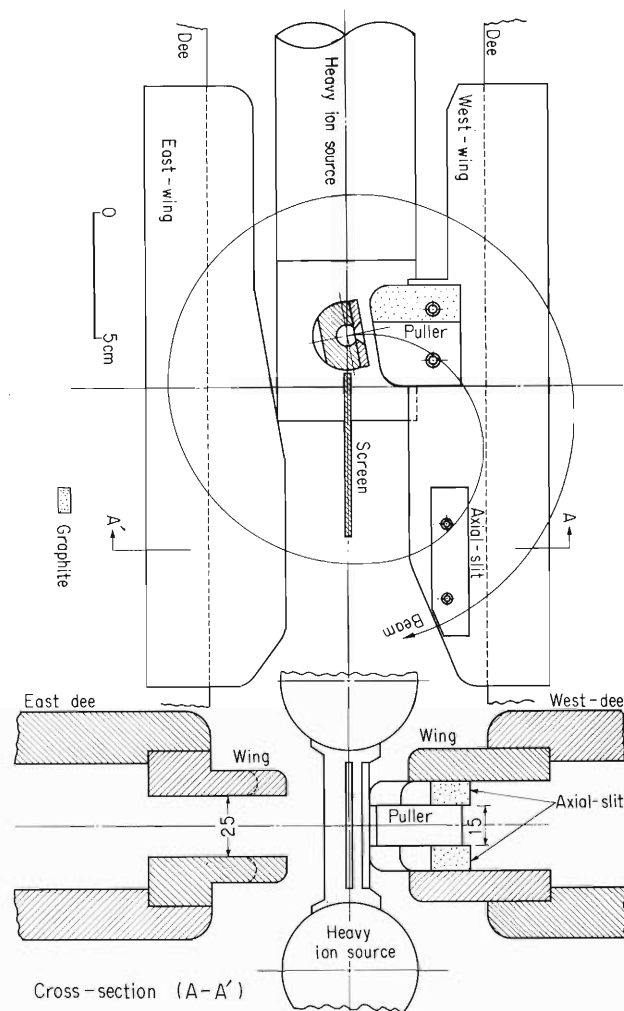


Fig. 1. Schematic drawing of the central geometry in the cyclotron. For the acceleration of heavy ions the screen is not provided.

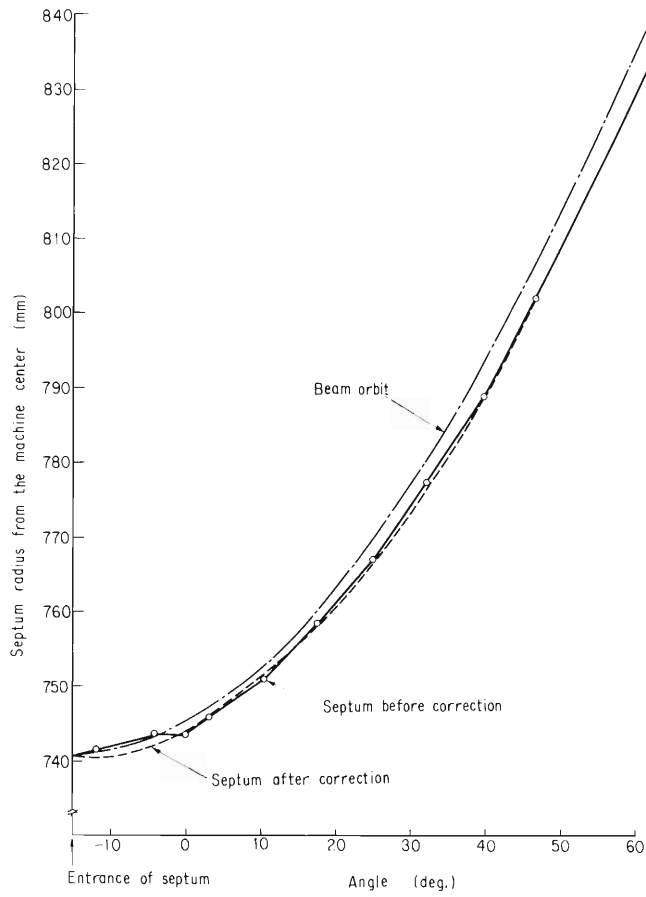


Fig. 2. Correction of the septum at the entrance part.

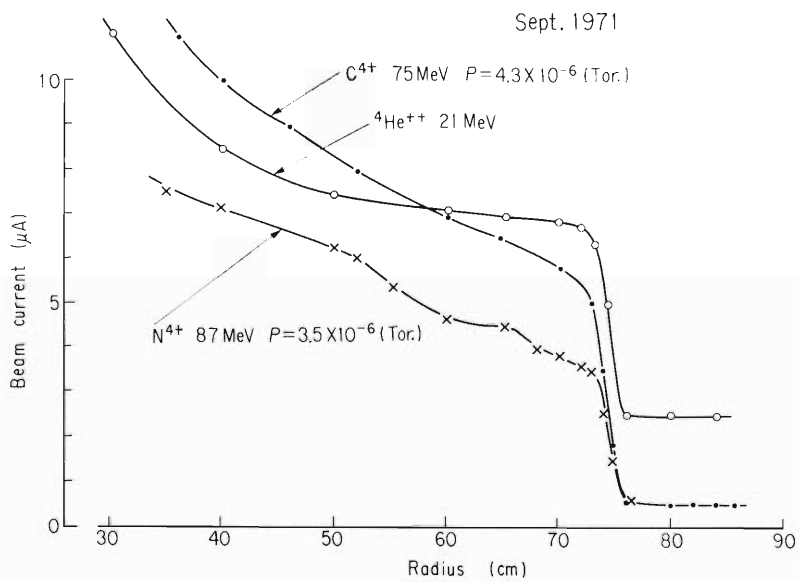


Fig. 3. Beam attenuation curve before corrections.

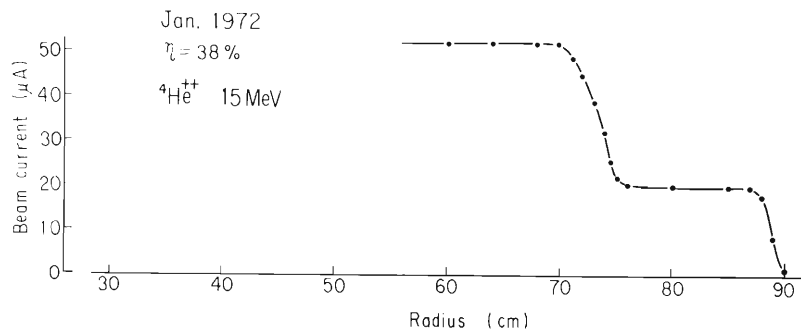


Fig. 4. Beam attenuation curve after corrections of the central region and deflector channel.

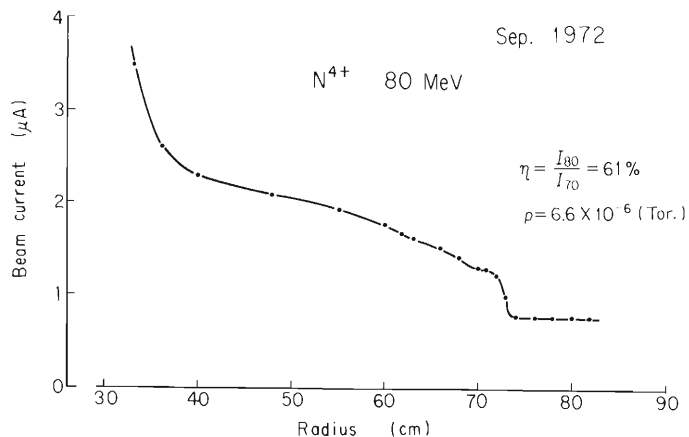
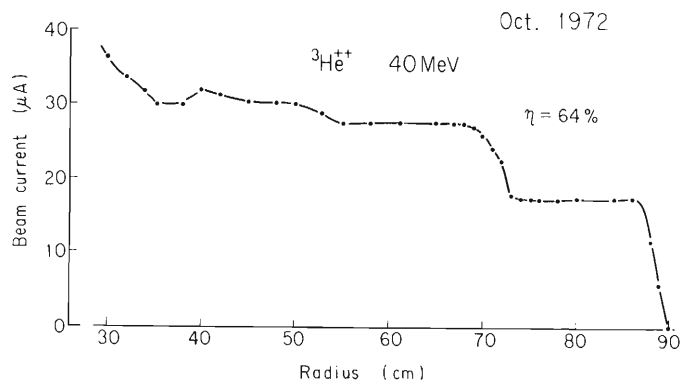
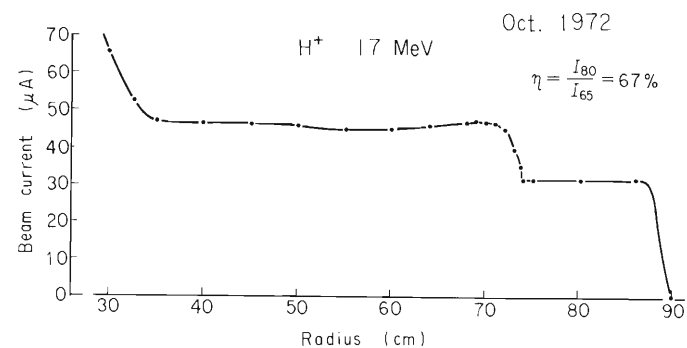


Fig. 5. Beam attenuation curves with the axial slit after corrections of the central region and deflector channel.

Since Feb. 1972, the central region geometry was changed as shown in Fig. 1, so that the first orbit is shielded effectively from the rf-field. The height of east wings is 25 mm. The screen which is made of molybdenum plate (2mm thick, 70 mm wide, and 50 mm high) is screwed on the supporting tube of the light-ion source. The axial slit indicated in Fig. 1 was not provided at that time. For the acceleration of heavy ions, we did not use a screen at the central region.

Besides, the exit part of the deflector was modified to have a larger radius of curvature to fit the orbit. The correction of the septum at the entrance part was done over the angle from -15° to 0° as shown in Fig. 2. By this improvement, the electric discharge at the channel exit was decreased and we could get a larger effective electric field for the beam in the deflector channel.

Figure 3 shows a typical beam attenuation curve before the corrections were done early in this year. In this case, the extraction efficiency was from 20 to 30 % for light ions and only 10 % for heavy ions.

Figure 4 shows a beam attenuation curve after the corrections of the central region and the deflector channel were applied. The extraction efficiency was improved to be about 40 % for light ions and about 20 % for heavy ions on the routine operation basis until the following modification was made.

To eliminate the axially spreading beam, the axial defining slit made of graphite was provided since Sept. 1972 in the west wings as shown in Fig. 1. It clips the height of beam at the first and second turn within 15 mm.

The beam attenuation curves with the axial slit are shown in Fig. 5. With these modifications the extraction efficiency has risen to about 47 % for light ions and about 35 % for heavy ions. These values are attainable without any special procedure in operation. With careful tunings, a maximum extraction efficiency of 67 % has been recorded for light ions and 60 % for heavy ions. The transparency of the deflector channel, which is the ratio of beam leaving the deflector to beam reaching the deflector, is about 70 %.

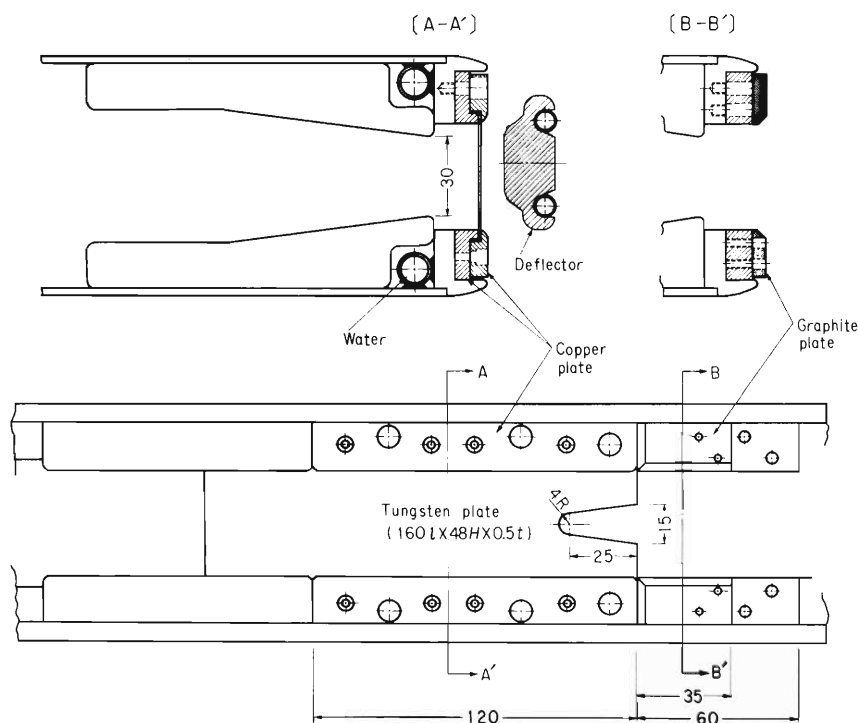
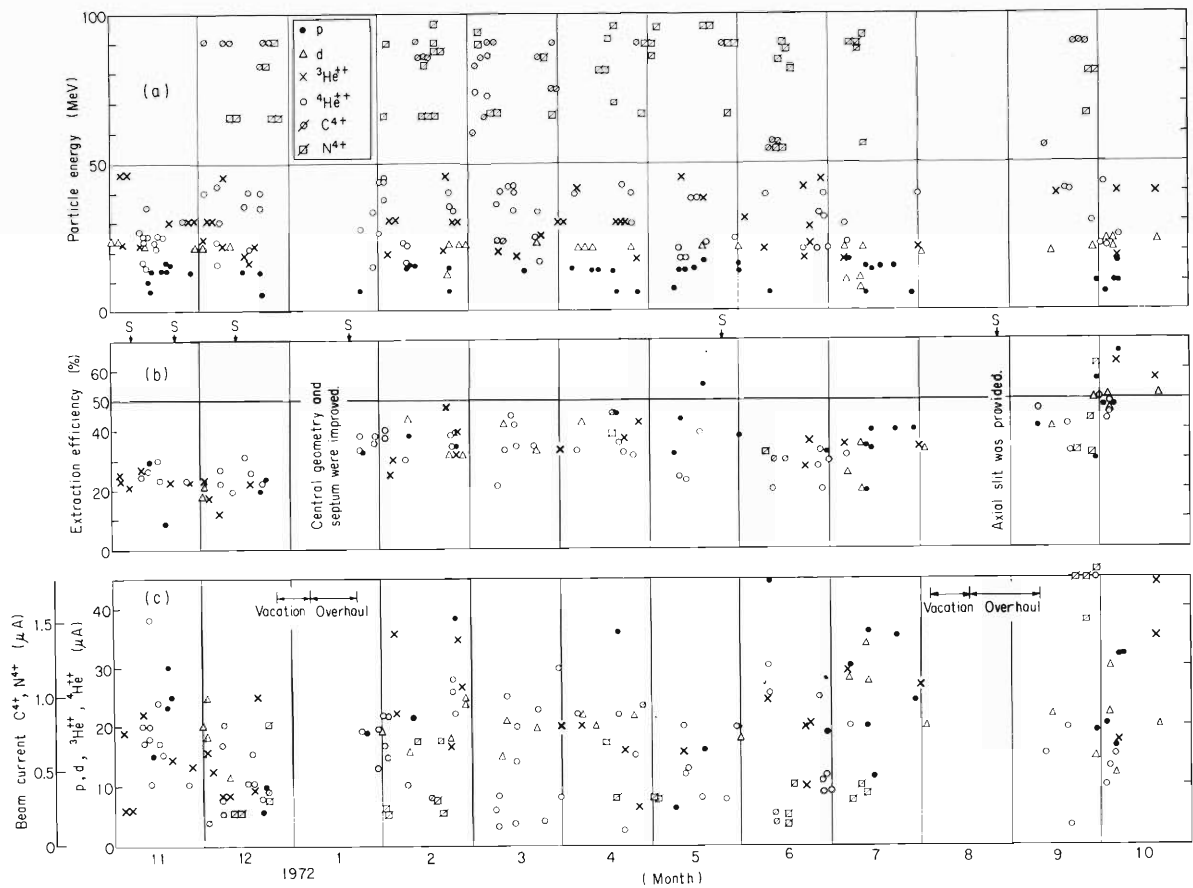


Fig. 6. Deflector cross section and septum shape of the cyclotron.

Figure 6 is the deflector cross section and the septum shape. For the long time continued operation, 1.5 kW can be dissipated in the simple slotted tungsten septum of 0.5 mm thickness.

By the enhancement of the extraction efficiency, the life time of the septum entrance has increased from 600 to 2000 h. Figure 7 shows an actual performance record obtained from the operation diary over the last one year. In this plot, the bad extraction efficiency can be interpreted to be due to misadjustment of the deflector channel and the deflector voltage.



- (a) Particle energies used for experiments.
- (b) Beam extraction efficiency.
- (c) Extracted beam currents which were actually employed in experiments.

Fig. 7. Plot obtained from the operation diary. Arrows represent the repair of septum entrance.

3-3. Polarized Ion Source

On the Construction of a Strong Field Ionizer and Measurement of Its Ionization Efficiency

S. Motonaga, T. Fujisawa, K. Ikegami,
H. Takebe, and M. Hemmi

Measurement of an ionized beam has been made to investigate the properties of a strong field ionizer for an atomic beam type polarized ion source and improvement in order to obtain the higher ionization efficiency is now being attempted.

In a previous measurement of atomic beam, the intensity of $1.5 \times 10^{15}/\text{cm}^2 \cdot \text{sec}$ was obtained. However, in order to get ion beam intensity of the order of μa for the source output further improvements were necessary in each part of the polarized ion source system.

(1) Construction of strong field ionizer

Basic design of the strong field ionizer is similar to that described by Glavish.¹⁾ Mechanical details of the strong field ionizer is shown in Fig. 1. The atomic beam is ionized by electron collision in a cylindrical region 1 cm in diameter and 14.5 cm long, where a magnetic field of about 1500 gauss is applied parallel to the axis. The solenoid and various electrodes of the ionizer have a common axis.

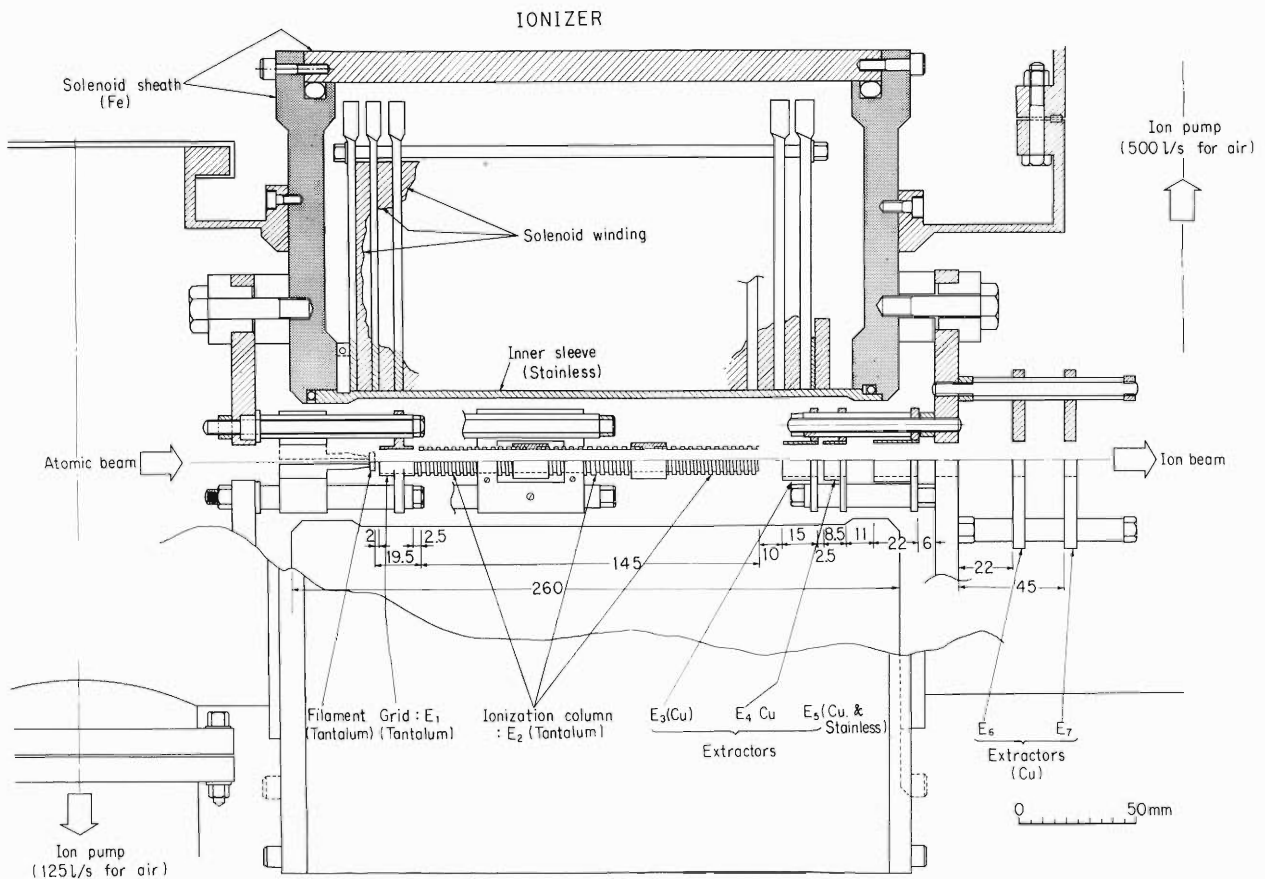


Fig. 1. Strong field ionizer.

The ionizing region is evacuated by two ion pumps to a pressure of the order of 10^{-6} to 10^{-7} Torr, to avoid as far as possible the presence of unpolarized hydrogen from the residual gas in the ionizing region.

The hollow electron beam is produced by a circular filament and accelerated to about 600 V relative to the filament. A negative voltage at E_3 (about 4 kV) repels the electrons backward, so that the electrons can oscillate back and forth throughout the "ionization column", being confined in a cylindrical sheet by the action of magnetic field. With multiple reflection the filament emission of 20 to 50 mA gives rise to a space current up to 100 mA. A photograph of the hollow electron beam is shown in Fig. 2.

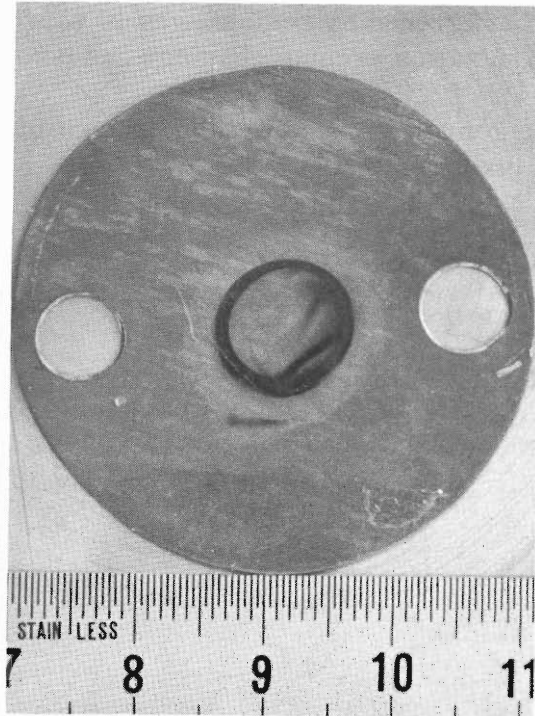


Fig. 2. Photograph of a typical hollow electron beam.

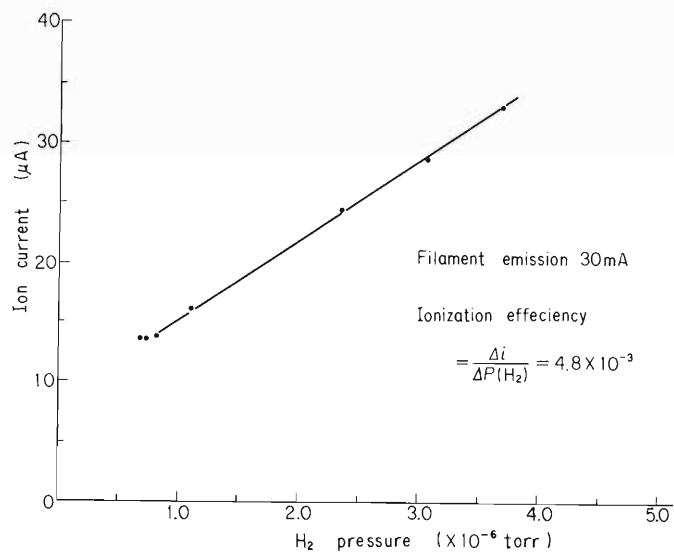


Fig. 3. H_2^+ ion current as a function of H_2 pressure.

The positive ions are extracted by the negative electrode, and a positive ion beam is formed and properly accelerated by means of a system of electrostatic lenses E₅, E₆, and E₇.

(2) Ionization efficiency

When hydrogen gas is admitted to the ionizer vacuum chamber and an increment in pressure of $\Delta P(\text{H}_2)$ produces an increment in H_2^+ ion current of $\Delta i(\text{H}_2^+)$, the ionization efficiency is given by $\Delta i(\text{H}_2^+)/\Delta P(\text{H}_2)$. Typical results are shown in Fig. 3. A measured value of efficiency is obtained at 4×10^{-3} . It is noted, however, that as indicated in the figure, the background by residual gas is very large. The presence of hydrogen molecules in the ionization vacuum chamber can be a source of unwanted background.

In order to reduce the remanent current, development of an ionization column and vacuum devices are now in progress.

Reference

- 1) H.F. Glavish: Nucl. Instr. Methods, 65, 1 (1968).

3-4. A Proposal of New Heavy Ion Accelerator System

M. Odera and H. Kamitsubo

The Cyclotron is now operating on the 24 h a day system over 5000 h per annum. As an only facility in Japan that accelerates heavy ions up to 100 MeV, about 30 % of the machine time are used in the researches by heavy ions. Not only nuclear physicists but also people of radiation chemistry, biology, and solid state physics are using the beam on the regular basis.

As the structure of the heavy ion source is more complex than the ion source for lighter projectiles and wear and tear are heavy owing to the large power dissipated in it, the maintenance work of technical persons has already become to a limit. Yet, there are desires for more heavy ion machine time, more ion species, more energy range, and so on.

In view of the above-mentioned situation a proposal to construct a new heavy ion accelerator was made.¹⁾ It will enable to accelerate ions in a wide range, or preferably all the elements at least to 7.5 MeV per nucleon. The energy can be varied, if not continuously, and the intensity of the beam will be moderate. According to the plan, the system consists of a variable frequency linac²⁾ as a prestripper accelerator and another accelerator as a post-stripper one. The latter will probably be a separate sector type isochronous cyclotron.³⁾

Table 1 shows maximum energies of various ions at the exit of the linac. The energy is amplified at a constant factor, say ten, if a separate sector type was chosen as a post-stripper machine.

Table 1. Energies of ions to be accelerated in the variable frequency linac.

Ion	${}^6\text{Li}^{2+}$	C^{4+}	Ar^{6+}	Kr^{8+}	Xe^{9+}
Energy (MeV)	40	80	120	160	180

References

- 1) Proc. VIth Intern. Cyclotron Conf., Vancouver, B. C. Canada (1972).
- 2) M. Odera: IPCR Cyclotron Progr. Rep., 6, 16 (1972); M. Odera and T. Tonuma: *ibid.*, p. 18 ; M. Odera and M. Hemmi: *ibid.*, p. 21 .
- 3) K. Matsuda: Sci. Papers I.P.C.R., 66, 33 (1972).

3-5. The Variable Frequency Linac Project

Construction of a Model Cavity

M. Odera

To extend the present heavy ion acceleration capability of the Cyclotron facility, we have proposed a new type accelerator complex.^{1), 2)} It consists of a variable frequency linac as a pre-stripper accelerator and another accelerator, probably a separated sector cyclotron, as a post-stripper one.^{2), 3)}

Unlike conventional fixed frequency linacs which accelerate different kinds of ions to the same velocity irrespective of the charge states of particles, this type gives higher velocity to ions of larger charge to mass ratio than to those of smaller ratio. For instance, while Xe^{9+} ion attains 1.4 MeV per nucleon, C^{4+} can reach 6.6 MeV/nucleon or 80 MeV total in the present design. These relatively high energies for lighter projectiles together with wide range of mass available will make the linac useful accelerator by itself alone for research and application.

Figure 1 shows the linac schematically. By changing the volume of the cavity at the voltage and current loop, the frequency can be changed in a wide range. The technique is quite similar to that being used in the present Cyclotron. Of course, there are some problems peculiar to the linac as high frequency and high power technique. Figure 2 is a real scale model cavity constructed to study these points. Test will start from the fall of 1972.

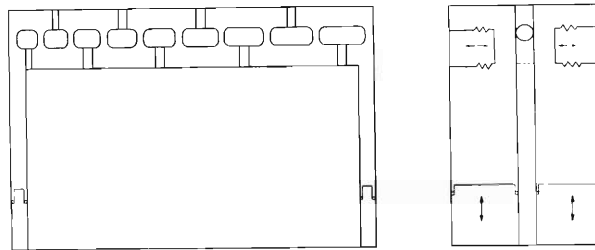
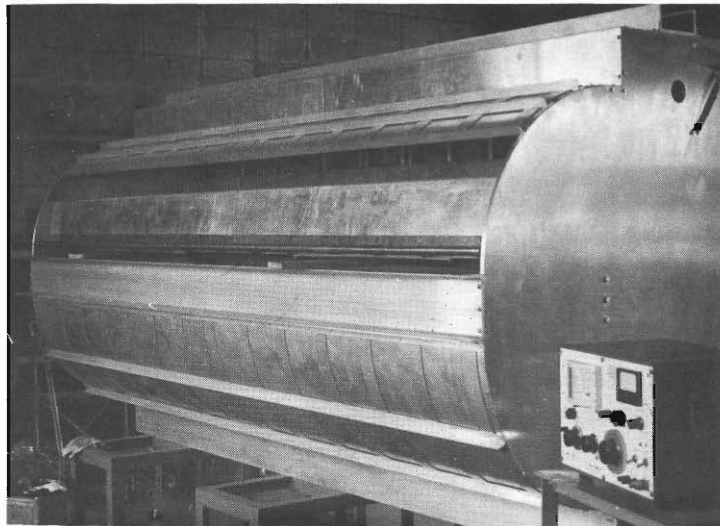
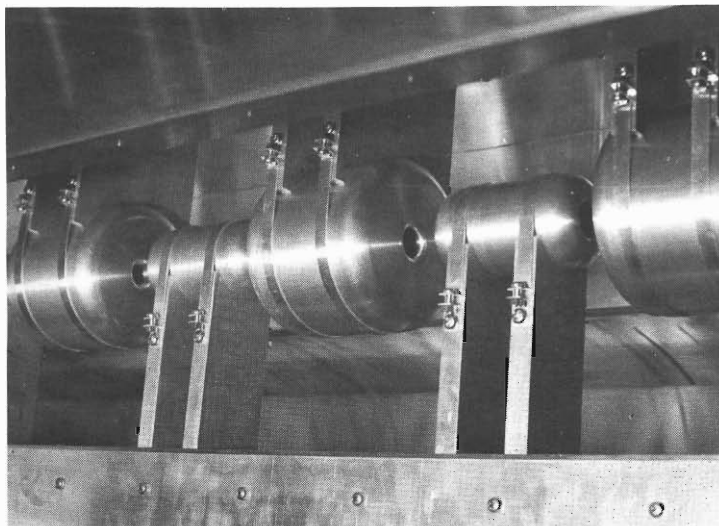


Fig. 1. Variable frequency linac cavity.



(a) The cavity with a side panel removed.



(b) The drift tubes.

Fig. 2. Photograph of the real scale model cavity.

References

- 1) M. Odera: IPCR Cyclotron Progr. Rep., 4, 24 (1970).
- 2) M. Odera and T. Tonuma: Proc. VIth Intern. Cyclotron Conf., Vancouver, B.C. Canada (1972).
- 3) K. Matsuda: Sci. Papers I.P.C.R., 66, 33 (1972).

3-6. The Variable Frequency Linac Project

Quadrupole Magnetic Field Gradient Necessary for Focusing Very Heavy Ions

T. Tonuma, F. Yoshida, and M. Odera

Combination of alternately convergent and divergent magnetic lenses overcomes the radial defocusing force given to an ion beam by the accelerating rf-field at the drift tube gaps in a linear accelerator.¹⁾ The magnetic field gradient of a quadrupole magnet in a drift tube necessary for focusing depends on the voltage of an injector in addition to the ratio of charge to mass of an ion and the rf electric field. Figure 1 shows field gradients required for quadrupole magnets when the voltage of the injector

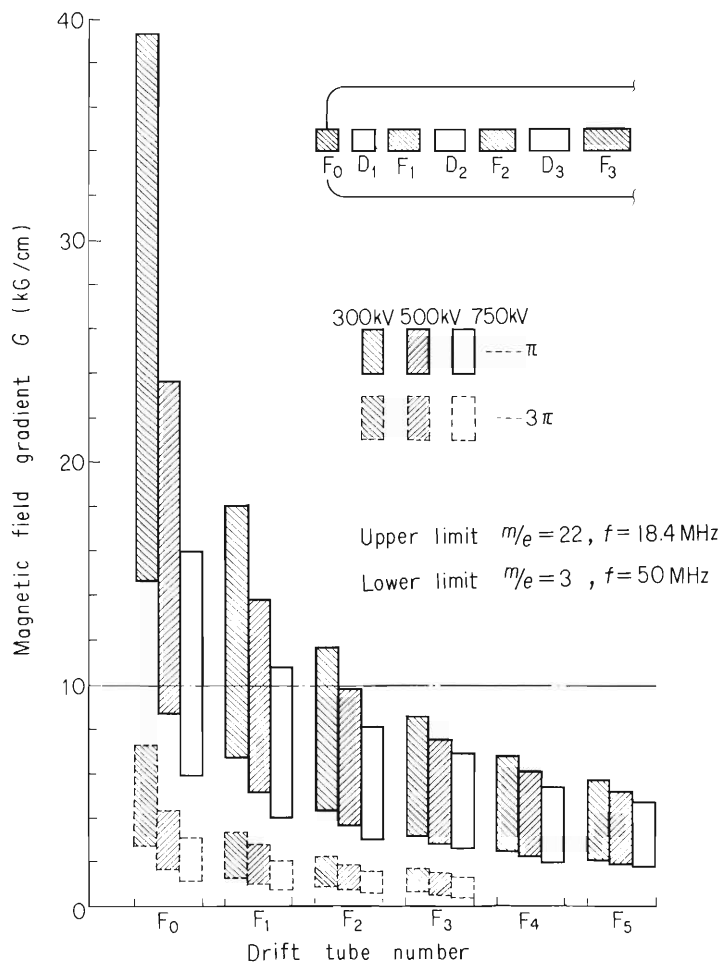


Fig. 1. Magnetic field gradients necessary for focusing. The calculation was carried out by using the following values of parameters: $EV = 1.5 \times 10^4$ kV²/cm, minimum gap 3 cm, transit time factor 0.85, and $\phi_0 = 65^\circ$ for synchronous particles. Here E and V are the electric field and potential difference between drift tubes, respectively.

is 300, 500, and 750 kV, other parameters being kept constant. The field gradients were estimated for quadrupole magnets provided in the first several drift tubes at earth potential. Because the necessary field gradients decrease with increase of ion velocities, the largest value is required for the magnet at the entrance of the linac. Solid lines give the field gradients for which the phase of the rf-field changes by π radian during the passage of the particle through a drift tube. In this case, however, a field gradient of above 10 kG/cm for the first few sections is required for focusing, which is difficult to realize technically. This difficulty is avoided by use of a longer drift tube having a quadrupole magnet in which the phase of rf-field changes by 3π , and the focusing requirement is satisfied with a smaller gradient as shown by dotted lines. In the figure the upper limit and the lower limit of the field gradient correspond to $m/e = 22$, $f = 18.4$ MHz and $m/e = 3$, $f = 50$ MHz respectively and this region contains the field gradient necessary for acceleration of particles expected to be accelerated in the linac.

The result of this calculation may be useful to discuss what voltage should be selected for an injector.

Reference

- 1) T. Tonuma, F. Yoshida, T. Wada, and M. Odera: IPCR Cyclotron Tech. Rep., No. 5 (1972).

3-7. A Study of Heavy Ion Source for a New Accelerator

I. Kohno

Since the construction of a new heavy ion accelerator was planned in this laboratory, an ion source for the new machine has been studied. Previously a multiply-charged heavy ion source of the radial extraction PIG type has been successfully used to accelerate several kinds of ions such as C^{4+} , N^{4+} , N^{5+} , O^{5+} , Ne, Ar, Kr, and Xe,¹⁾ in the cyclotron, therefore the experiences obtained could provide a starting basis for the study of new source. The following improvements should be made to satisfy the requirements of the new machine.

(1) The number of elements to be used for producing multiply-charged ions, must be increased greatly, because the new machine intends to accelerate many kinds of projectiles. For this purpose, the ion sources for solid state samples are being developed. They have a furnace or a sputtering electrode.

(2) The ion beams extracted from the source must have an emittance as small as possible in order to be accepted and accelerated efficiently by the new machine which will be a linac.

As is well known, the linac type accelerator has a relatively small radial phase acceptance. The value of the permissible phase space depends on the voltage of preacceleration before injection into the linac as well as on the source emittance. Tentatively, 100 mm mrad. were chosen as a design goal for a beam extracted by 20 kV. To this end, preparation is now made for the sources of duoplasmatron type and PIG type with axial extraction. The test bench apparatus used for the development of the ion source of the cyclotron²⁾ is being modified in these studies. Ion source for solid state material will be investigated by the test bench in the next year.

References

- 1) I. Kohno, Y. Miyazawa, T. Tonuma, S. Nakajima, T. Inoue, A. Shimamura, K. Yoshida, and T. Karasawa: IPCR Cyclotron Progr. Rep., 3, 6 (1969); I. Kohno, Y. Miyazawa, T. Tonuma, T. Inoue, A. Shimamura, and S. Nakajima: IPCR Cyclotron Progr. Rep., 5, 5 (1971).
- 2) I. Kohno, T. Tonuma, and S. Nakajima: J. Vacuum Soc. Japan, 10, 27 (1967).

3-8. A Quadrupole Magnet of Compact Size

M. Odera and M. Hemmi

A small quadrupole magnet was manufactured and tested. It was aimed to ascertain the possibility of obtaining a high gradient quadrupole field necessary for focusing the heaviest element to be accelerated in the linac under contemplation.¹⁾

Figure 1 is a photograph of the magnet, of which the outer diameter is 12 cm and the aperture for beam is 16 mm. The coil is wound with a copper pipe of 6 mm O.D. and 4 mm I.D. insulated with glass fiber tubings. It is cooled by water flowing inside.

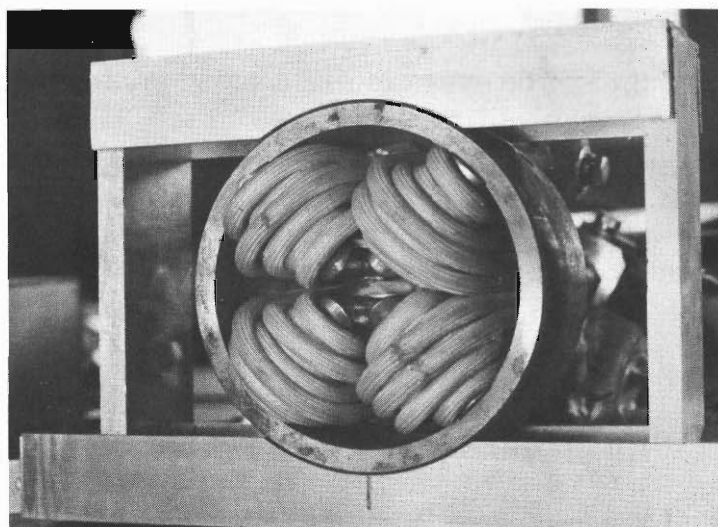


Fig. 1. Photograph of the test quadrupole magnet.

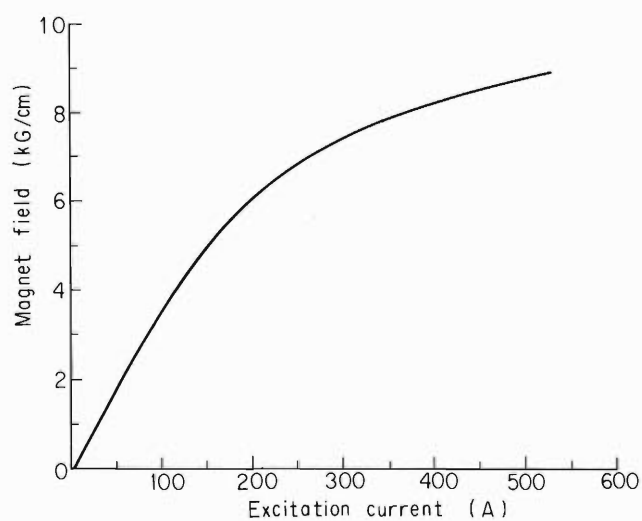


Fig. 2. Excitation curve of the magnetic field gradient.

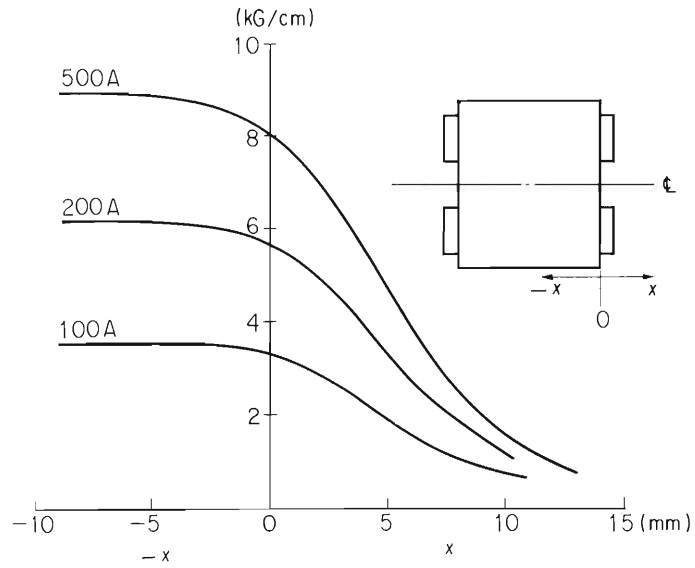


Fig. 3. The extent of constancy of gradient.

Figure 2 shows an excitation curve and Fig. 3 shows the region of constancy of the field gradient along the axis. The radius of curvature of pole tips is 1.125 times the radius of the aperture. The value of gradient is sufficient to focus the heaviest ions to be accelerated in the linac by use of a 3π mode acceleration for the first few sections of drift tubes.²⁾

References

- 1) M. Odera and T. Tonuma: Proc. VIth Intern. Cyclotron Conf., Vancouver, B. C. Canada (1972).
- 2) T. Tonuma, M. Odera, and F. Yoshida: IPCR Cyclotron Progr. Rep., 6, 18(1972).

4. NUCLEAR PHYSICS

Scattering and Reactions

4-1. A Study of Transfer Reactions Induced by 90 MeV ^{14}N on ^{52}Cr

I. Kohno, S. Nakajima, I. Yamane, M. Yoshie,
M. Odera, and H. Kamitsubo

It was reported recently that transfer reactions induced by heavy ions show two types of reaction mechanism. In one case the cross sections for direct reactions giving discrete energy spectra are strongly enhanced, and in the other case energy spectra have not a selectively enhanced peak, but a broader distribution. In order to study the mechanism of reactions to transfer one, two, three or four nucleons in more detail, we measured transfer reactions induced by 90 MeV ^{14}N on ^{52}Cr using the cyclotron.

The method of measurement was described in another paper of this progress report.¹⁾

In Fig. 1 the P.I.O. (Particle Identifier Output) spectrum for $^{52}\text{Cr} + ^{14}\text{N}$ is shown. The relative yield of particles seems to have a relation as reported by Artukh et al.²⁾ and Diamond et al.,³⁾ that the yield of the reaction cross section is proportional to the ground-ground transfer Q-value, Q_{gg} and the change of Coulomb interaction energy $\Delta E_C = (Z_1^i Z_2^i - Z_1^f Z_2^f) e^2 / R$.

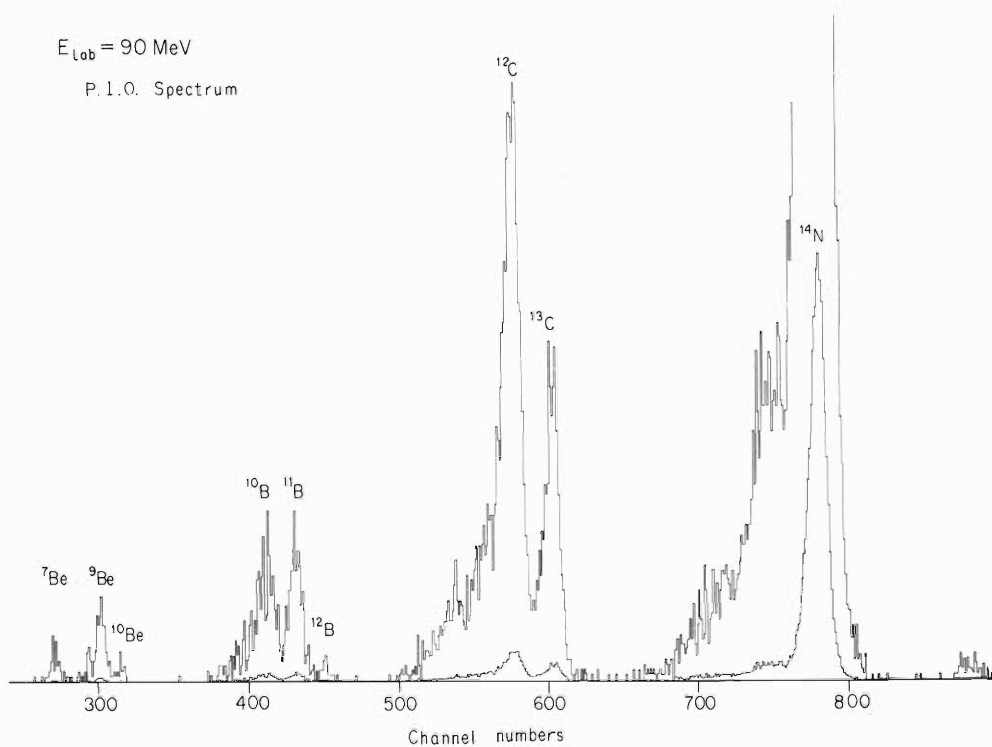


Fig. 1. P.I.O. spectrum resulting from bombardment of ^{52}Cr target with 90 MeV ^{14}N projectiles.

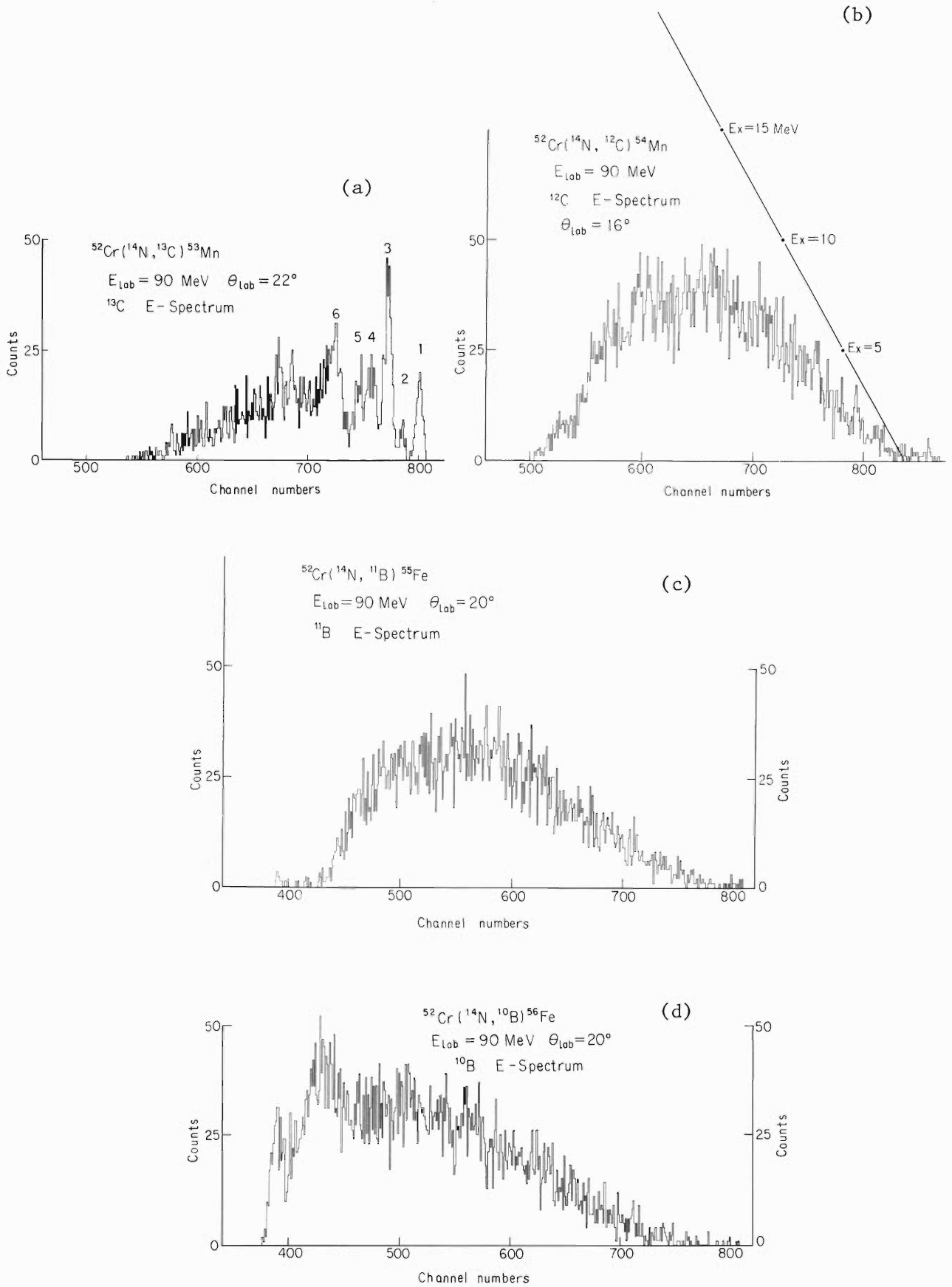


Fig. 2. Energy distributions of (a) ^{13}C , (b) ^{12}C , (c) ^{11}B , and (d) ^{10}B produced by 90 MeV ^{14}N projectiles.

In Fig. 2 the energy distributions of (a) ^{13}C , (b) ^{12}C , (c) ^{11}B , and (d) ^{10}B produced by 90 MeV ^{14}N projectiles are shown. Very different behaviors appear for the energy distributions observed on the products of single proton transfer reactions (^{13}C) and those of multi-nucleon transfer reactions (^{12}C , ^{11}B , ^{10}B). Only in the former, well-resolved peaks corresponding to the levels of ^{53}Mn were observed and the spectrum shows a smaller yield in the lower energy region of ^{13}C particles. But, in the latter spectra, the yields are small at the quasi-elastic part, in which both residual nuclei are near the ground state, and the maximum yields are observed at the positions corresponding to about 15 ~ 20 MeV excited levels of residual nuclei.

Angular distributions of six peaks for a single proton transfer reaction are shown in Fig. 3. They show small oscillations, which would be described by a diffraction model, and the cross sections decrease monotonously with the increase of scattering angles. These features are not similar to the experimental data described by several authors,⁴⁾ who showed a broad maximum for the angular distribution due to the tunneling process. The angular distribution of ^{12}C projectiles after integration over energy from $Q = Q_{\text{gg}}$ to $Q = Q_{\text{gg}} - 20$ MeV is shown in Fig. 4. The angular distribution shows little oscillation, and the yield decreases monotonously with increasing scattering angle. This feature is the same as in the angular distribution of quasi-inelastic transfer reaction described by Galin et al.⁴⁾

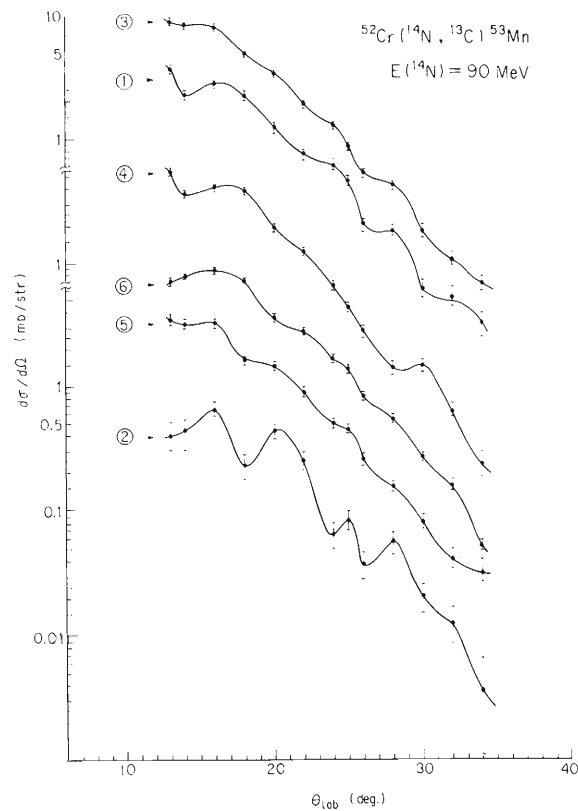


Fig. 3. Angular distributions of six peaks in the energy distribution of ^{13}C produced by 90 MeV ^{14}N projectiles.

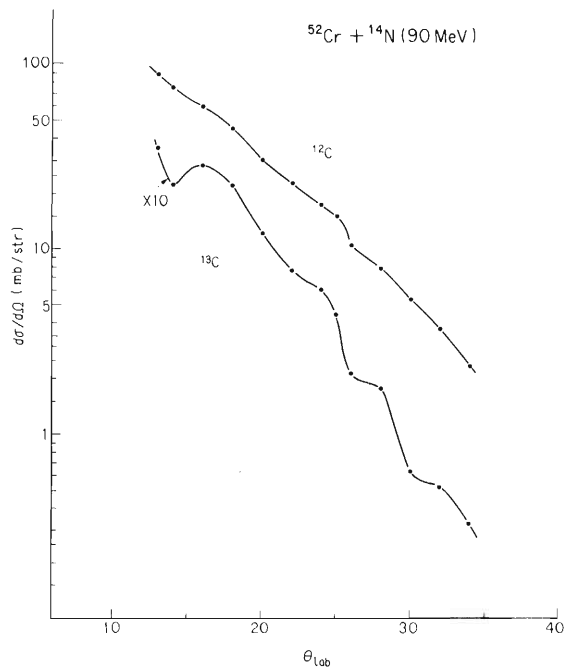


Fig. 4. Angular distributions of ^{12}C projectiles for partial energy spectrum in the range of Q_{gg} to $Q_{gg} - 20$ MeV.

From these observations, it is supposed that in case of a single proton transfer, a direct surface interaction is the main mechanism, but in case of multi-nucleon transfer a grazing collision is more dominant than the surface collision. But, as the data are not decisive to determine the reaction mechanism, this study is to be continued by varying projectile energy and species.

References

- 1) S. Nakajima, I. Kohno, I. Yamane, M. Yoshie, M. Odera, and H. Kamitsubo: IPCR Cyclotron Progr. Rep., 6, 89 (1972).
- 2) A.G. Artukh, V.V. Avdeikov, J. Erö, G.F. Gridnev, V.L. Mikheev, V.V. Volkov, and J. Wilczynski: Nucl. Phys., A160, 511 (1971).
- 3) R.M. Diamond, A.M. Poskanzer, F.S. Stephens, W.J. Swiatecki, and D. Ward: Phys. Rev. Letters, 20, 802 (1968).
- 4) R. Kaufmann and R. Wolfgang: Phys. Rev., 121, 192 (1961); J. Galin, D. Guerreau, M. Lefort, J. Peter, X. Tarrago, and R. Basile: Nucl. Phys., A159, 461 (1970).

4-2. Selective Excitation of One Proton Configuration for ^{53}Mn in $^{52}\text{Cr}(^{14}\text{N}, ^{13}\text{C})^{53}\text{Mn}$ and $^{52}\text{Cr}(^{12}\text{C}, ^{11}\text{B})^{53}\text{Mn}$

S. Nakajima, I. Kohno, I. Yamane, M. Yoshie,
H. Kamitsubo, M. Odera, and T. Mikumo

One proton transfer reactions induced by 90 MeV ^{14}N and 90 MeV ^{12}C ions on a target of ^{52}Cr were studied. The spectra obtained for the reactions ($^{14}\text{N}, ^{13}\text{C}$) and ($^{12}\text{C}, ^{11}\text{B}$) on ^{52}Cr are compared in Fig. 1. Excitations of several single proton states in the residual nucleus are enhanced for both reactions, and these reactions leave ^{13}C and ^{11}B in their ground states. It is noted by comparing the spectra that relative cross sections of several peaks are very different in the two reactions. Especially the cross section ratio $[\text{d}\sigma/\text{d}\Omega(\text{Ex}=2.4 \text{ MeV})] / [\text{d}\sigma/\text{d}\Omega(\text{Ex}=0)]$ is 2.17 for the ($^{14}\text{N}, ^{12}\text{C}$) reaction, but it is 0.51 for the ($^{12}\text{C}, ^{11}\text{B}$) reaction (Table 1).

This feature will be explained from an angular momentum matching of the reaction.¹⁾ By a reaction theory, the following selection rules are applied to the transferred orbital angular momentum ℓ :

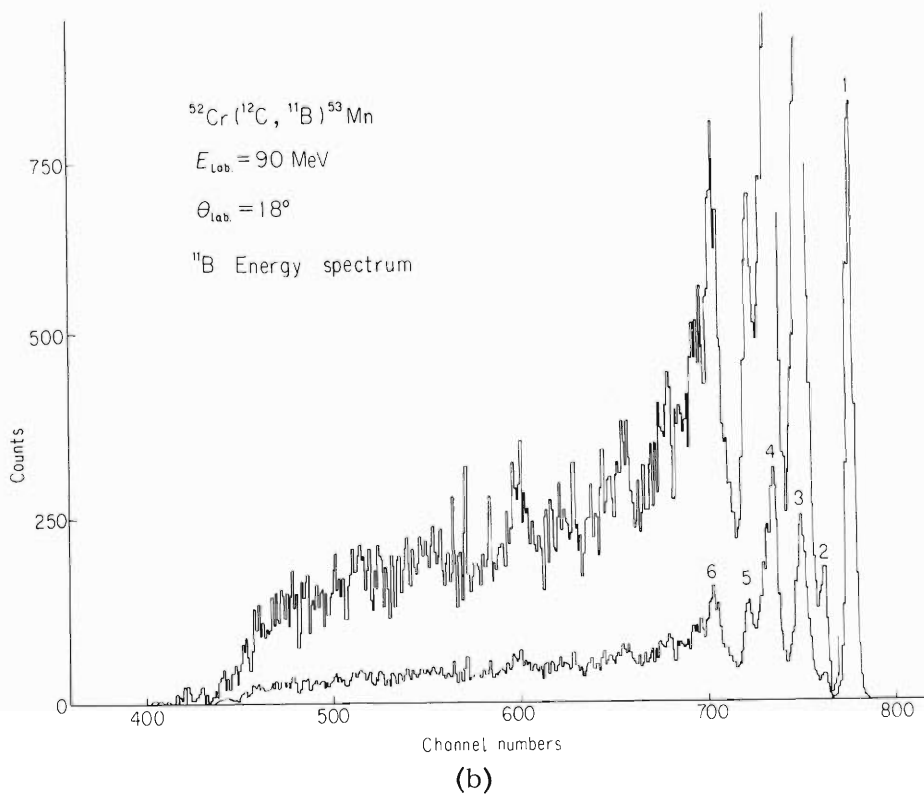
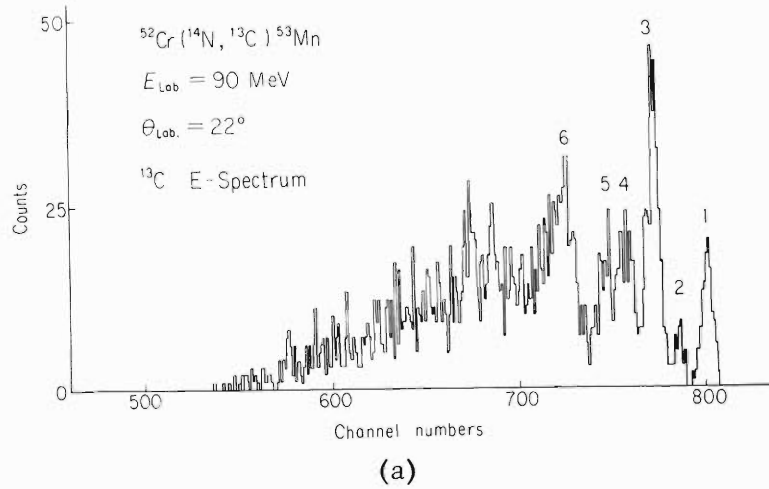
$$\begin{aligned} &| \ell_1 - \ell_2 | \leq \ell \leq \ell_1 + \ell_2, \quad | j_1 - j_2 | \leq \ell \leq j_1 + j_2 \\ &\ell_1 + \ell_2 + \ell = \text{even}, \end{aligned}$$

where ℓ and j are orbital angular momenta and total angular momenta of the transferred nucleon in the projectile (subscript 1) and the residual nucleus (subscript 2). The allowed ℓ transfers for the reactions studied here are listed in Table 2. On the other hand, the difference of the orbital angular momenta of the incoming and outgoing particles at the nuclear surface ΔL , can be calculated for the reaction from the following relations.

$$\Delta L = L_1 - L_2. \quad (1)$$

$$\begin{aligned} L_1 &\simeq K_1 R_1 (1 - 2\eta_1 / K_1 R_1)^{1/2}, \quad L_2 \simeq K_2 R_2 (1 - 2\eta_2 / K_2 R_2)^{1/2}, \\ R_1 &= r_0 (A_1^{1/3} + A_t^{1/3}), \quad R_2 = r_0 (A_2^{1/3} + A_r^{1/3}), \end{aligned}$$

where L_1, L_2, K_1, K_2 stand for orbital angular momenta and wave numbers in the entrance and exit channel. A_1, A_2 are masses of the incident and outgoing particles, and A_t, A_r are that of a target and a residual nucleus. η_1, η_2 are Sommerfeld parameters of the incident and the exit channel. ΔL values of both reactions calculated from Eqn.(1) are also listed in Table 2. The angular momentum matching shows that the cross section ratios of both reactions are probably explicable from this consideration. A small cross section of $E_x = 1.3 \text{ MeV}$ in both reactions is presumably due to the fact that a main configuration of this level comes from the coupling of the 1st 2^+ state of ^{52}Cr and the ground $1f_{7/2}$ state of ^{53}Mn , and that a component of single particle $2p_{3/2}$ state is small.



Numbers of peaks correspond to the first column of Table 1.

Fig. 1. Energy spectra of ^{13}C from the $^{52}\text{Cr}(^{14}\text{N}, ^{13}\text{C})^{53}\text{Mn}$ reaction (a) and of ^{11}B from the $^{52}\text{Cr}(^{12}\text{C}, ^{11}\text{B})^{53}\text{Mn}$ reaction (b).

Table 1. Relative cross section.

Level No.	E_x (MeV)	$n_2 \ell_2 j_2^*$	(^{14}N , ^{13}C)	(^{12}C , ^{11}B)
1	0	$1f_{7/2}$	1	1
2	1.3	$2p_{3/2}$	0.1	0.046
3	2.4	$2p_{3/2}$	2.17	0.51
4	3.7	$1f_{5/2}$	1.7	0.715
5	4.9	$1f_{5/2}$	0.74	0.195
6	6.6	--	3.17	0.34

* See Reference 2)

Table 2. Allowed ℓ values and calculated ΔL values.

E_x (MeV)	$^{52}\text{Cr} (^{14}\text{N}, ^{13}\text{C}) ^{53}\text{Mn}$				$^{52}\text{Cr} (^{12}\text{C}, ^{11}\text{B}) ^{53}\text{Mn}$			
	L_1	L_2	ΔL	allowed ℓ	L_1	L_2	ΔL	allowed ℓ
0	41.1	40.8	0.2	4	40.3	36.3	4.0	4, 2
1.3		40.2	0.9	2		35.7	4.6	2, 0
2.4		39.7	1.4	2		35.2	5.1	2, 0
3.7		39.0	2.1	2		34.7	5.6	4, 2
4.9		38.4	2.7	2		34.1	6.2	4, 2

References

- 1) D.M. Brink: Phys. Letters, 40B, 37 (1972).
- 2) D.D. Armstrong and A.G. Blair: Phys. Rev., 140, B1226 (1965).

4-3. Gamma Transition from the First 3^- Levels in $^{94, 96, 98, 100}\text{Mo}$

T. Inanaga, H. Kamitsubo, T. Fujisawa, T. Wada,
M. Koike, and K. Pingel

Nuclear structure of even mass molybdenum isotopes has been investigated in this laboratory by using inelastic scattering of protons,¹⁾ deuterons,²⁾ and alpha-particles³⁾ and also by some other reactions such as (t, p).⁴⁾ In order to get further information on the properties of low-lying levels, electromagnetic transitions between them were studied. The E2 transitions have been extensively investigated by many authors and gave some insight on the collective nature of those levels. This work was aimed at mainly to measure weak E1 transitions from 3^- states to lower even parity states and to obtain information on the small components contained in these states. Gamma decays from 3^- to lower 2^+ and 4^+ states must be E1 or M2 transitions. In medium weight and heavy nuclei, E1 transitions between low lying states are strongly hindered (about $10^{-4} \sim 10^{-6}$ of Weisskopf-unit), whereas the hindrance factors for M2 transitions are not so large.⁵⁾ Indeed the hindrance factor of E1 transition obtained in this work is about 1.7×10^{-6} in ^{98}Mo . Because the Weisskopf-unit for E1 is larger by the order of 10^7 than that of M2 in this range of gamma energy, we can conclude that most of the transitions from 3^- to 2^+ or 4^+ states have E1 character. It was tried to measure the absolute values for E1 transitions by using the particle-gamma coincidence method.

From the values of β obtained by inelastic scattering to the 3^- states, the $B(E3)$ values can be calculated. If the branching of the gamma transition from the 3^- level to the 0^+ ground state is observed, we can get the absolute values of E1 transition which decays from 3^- to 2^+ or 4^+ by using the above-mentioned $B(E3)$ and branching ratios.

The 3^- levels were excited by $\text{Mo}(p, p')$ inelastic scattering at $E_p = 14.5$ MeV. With this bombarding energy of protons, most of gamma-rays come from the decay of compound nucleus. Therefore the particle-gamma coincidence method was used to make sure that the gamma radiations really decay from these 3^- levels and to reduce backgrounds. Protons were measured by a Si detector and gamma rays were detected

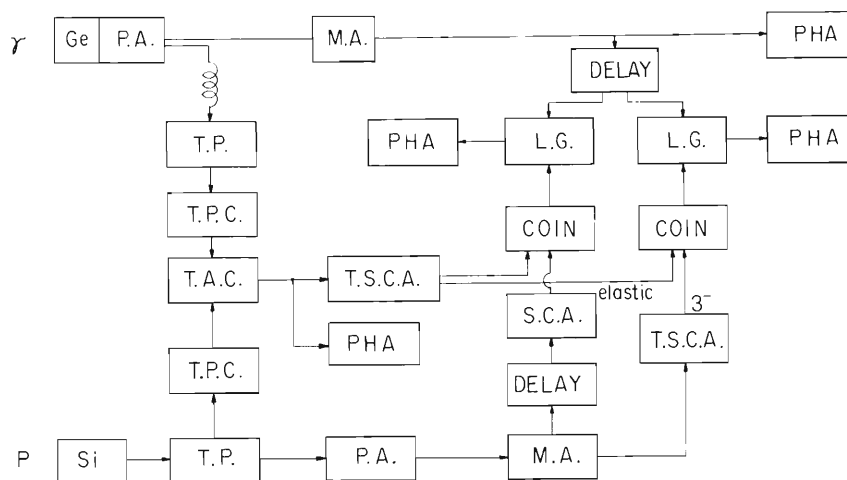


Fig. 1. Block diagram of the electronics.

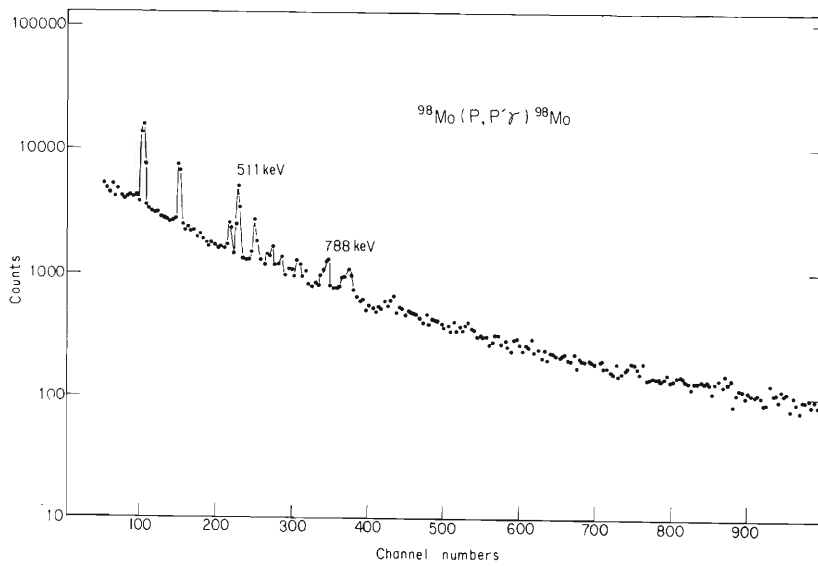


Fig. 2. Single spectrum of γ radiation in $^{98}\text{Mo}(p, p' \gamma)$.

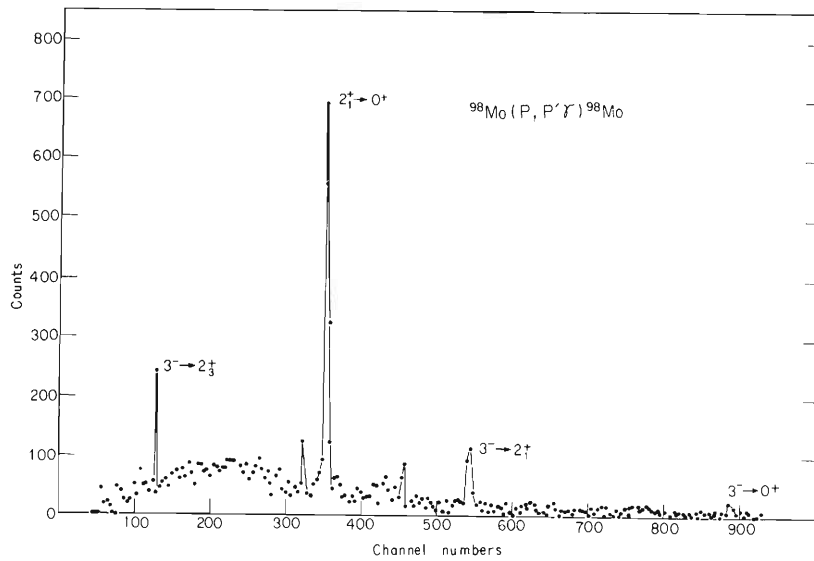


Fig. 3. Coincident γ spectrum between γ -rays and 3^- protons in $^{98}\text{Mo}(p, p' \gamma)$.

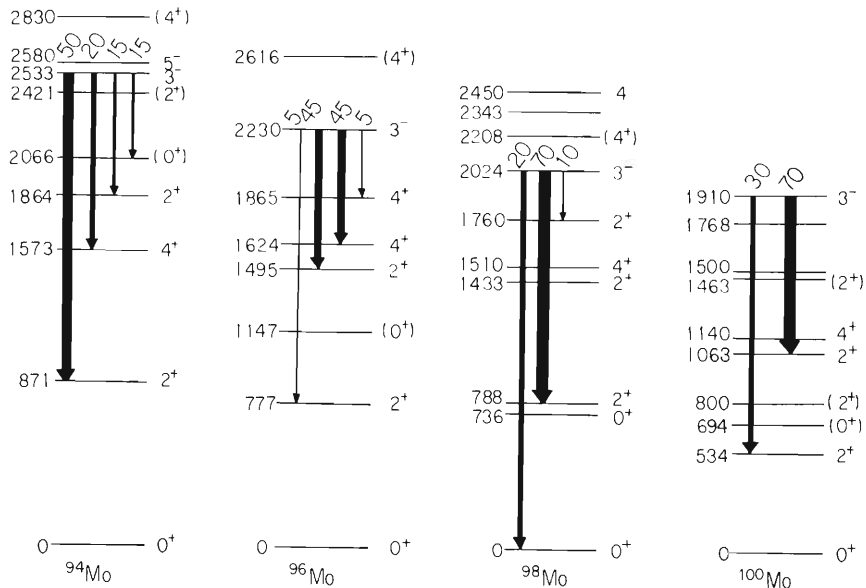


Fig. 4. Low-lying energy levels and 3^- branching ratio of $^{94,96,98,100}\text{Mo}$.

by a 50 cc Ge(Li)-counter which was placed at $\theta_{\text{lab}} = 90^\circ$ in the reaction plane. Figure 1 shows the block diagram of the electronics. Time pick off circuits for both particle and gamma signals were used for the fast coincidence and the timing resolution was about 50 ns. To measure random coincidences, the coincidence between elastically scattered protons and gamma rays were taken.

Figure 2 shows a single spectrum of gamma rays in $^{98}\text{Mo}(p, p' \gamma)^{98}\text{Mo}$ and Fig. 3 for a coincident spectrum. Energy levels and branching ratios are shown in Fig. 4.

A transition from the 3^- to the ground state is only seen in ^{98}Mo . If we use the $B(E3) = 34 \pm 4$ s.p.u. and the transition probability for $3^- \rightarrow 2^-$, the E1 transition is $T = (3.7 \pm 1.0) \times 10^9$ (sec^{-1}) and the hindrance factor is 1.7×10^{-6} .

The coincidence spectrums have no systematic trend from ^{94}Mo to ^{100}Mo . Analysis based on the nuclear structure theory in this mass range is in progress.

References

- 1) T. Wada, K. Matsuda, Y. Awaya, N. Nakanishi, and S. Takeda: IPCR Cyclotron Progr. Rep., 3, 36 (1969).
- 2) T. Wada, H. Kamitsubo, T. Fujisawa, M. Koike, and T. Inanaga: *ibid.*, 6, 33 (1972).
- 3) K. Matsuda, Y. Awaya, N. Nakanishi, and S. Takeda: *ibid.*, 4, 38 (1970).
- 4) S. Takeda, I. Kohno, S. Yamaji, K. Matsuda, N. Nakanishi, Y. Awaya, and S. Kusuno: J. Phys. Soc. Japan, (to be published).
- 5) H. Ejiri, T. Shibata, and K. Satoh: Phys. Lett., 38B, 73 (1972).

4-4. Inelastic Scattering of Deutrons by Even Mo Isotopes

T. Wada, H. Kamitsubo, T. Fujisawa,
M. Koike, and T. Inanaga

The nuclear structure of Mo isotopes was investigated previously by inelastic scattering of protons¹⁾ and alpha-particles²⁾ by using the IPCR cyclotron. The isotopic spin dependence of the excitation process for the first 2^+ and 3^- states was investigated. In the (α, α') scattering, however the energy resolution was not sufficient to resolve the peaks corresponding to the alpha-particles exciting the first 4^+ , and the second 0^+ , 2^+ states.

The incident deuteron beam from the cyclotron was first energy analyzed by a magnet and focused on the target. The incident energy was 21.5 MeV. The targets were the same as those used in the experiment of (p,p') and (α, α') . Scattered particles were detected with a counter telescope system of SSD with thickness $300 \mu\text{m}$ and $2000 \mu\text{m}$, and analyzed with an on-line computer DDP-124.³⁾ The energy resolution was about 100 keV. Figure 1 shows an example of the energy spectrum and Fig. 2 shows the angular distribution of the scattered deuterons. As shown in Fig. 1, the two peaks of two-phonon like states were resolved with the aid of a computer program. The angular distributions of the deuterons exciting the two states showed anti-phase diffraction patterns to each other, while in case of the proton scattering they were in-phase. Further analysis of the present experiment is now in progress.

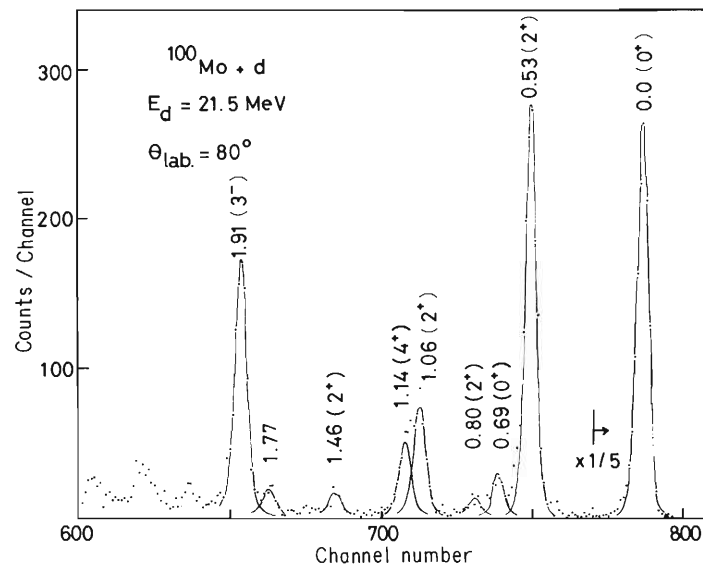


Fig. 1. Energy spectrum of deuterons scattered from ^{100}Mo nuclei. The solid curves are the results of least-square fit with skewed Gaussian.

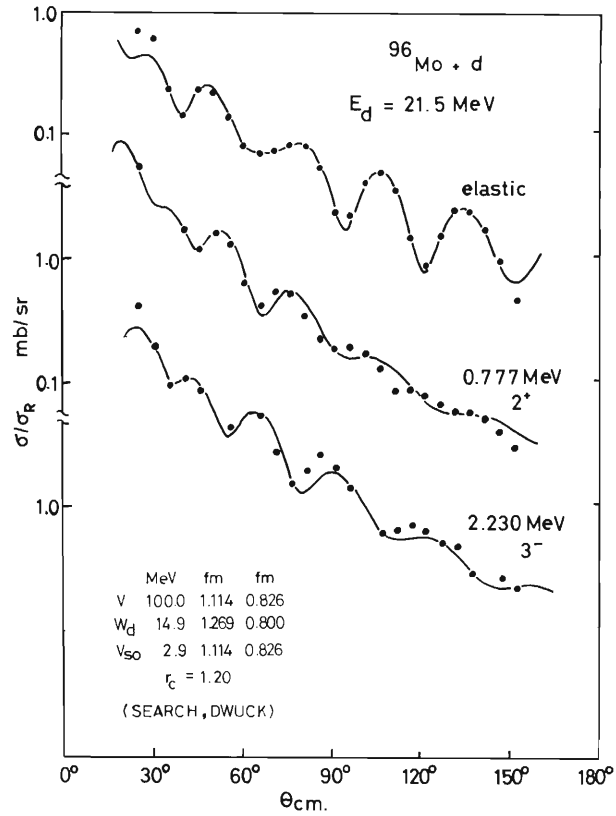


Fig. 2. The angular distributions of scattered deuterons from ^{96}Mo . The solid curves are obtained by calculation with the automatic parameter search code, SEARCH and DWUCK.

References

- 1) T. Wada, K. Matsuda, Y. Awaya, N. Nakanishi, and S. Takeda: IPCR Cyclotron Prog. Rep., 3, 36 (1969).
- 2) K. Matsuda, Y. Awaya, N. Nakanishi, and S. Takeda: J. Phys. Soc. Japan (to be published).
- 3) T. Wada, Y. Chiba, and F. Yoshida: IPCR Cyclotron Progr. Rep., 5, 78 (1971).

4-5. Unbound Isobaric Analog States Induced by $^{50, 52, 54}\text{Cr}$ (h, d)
 $^{51, 53, 55}\text{Mn}$ Reactions

S. Takeda, N. Nakanishi, H. Ohnuma,
 H. Toyama,* and S. Yamada*

Experimental aspects on the isobaric analog states of $^{51, 53, 55}\text{Mn}$ in proton elastic scattering were given by Moses et al.¹⁾ The population of isobaric analog states in the (h,d) reaction provides an additional information to what has been obtained by studies of resonance reactions for the following reason. The analog states cannot be studied in the (p,p) and (p,p') resonance reactions whenever the proton energy in the entrance channel is well below the Coulomb barrier. On the other hand, in a sufficiently high h-energy, these states can be excited in the (h,d) reaction process.

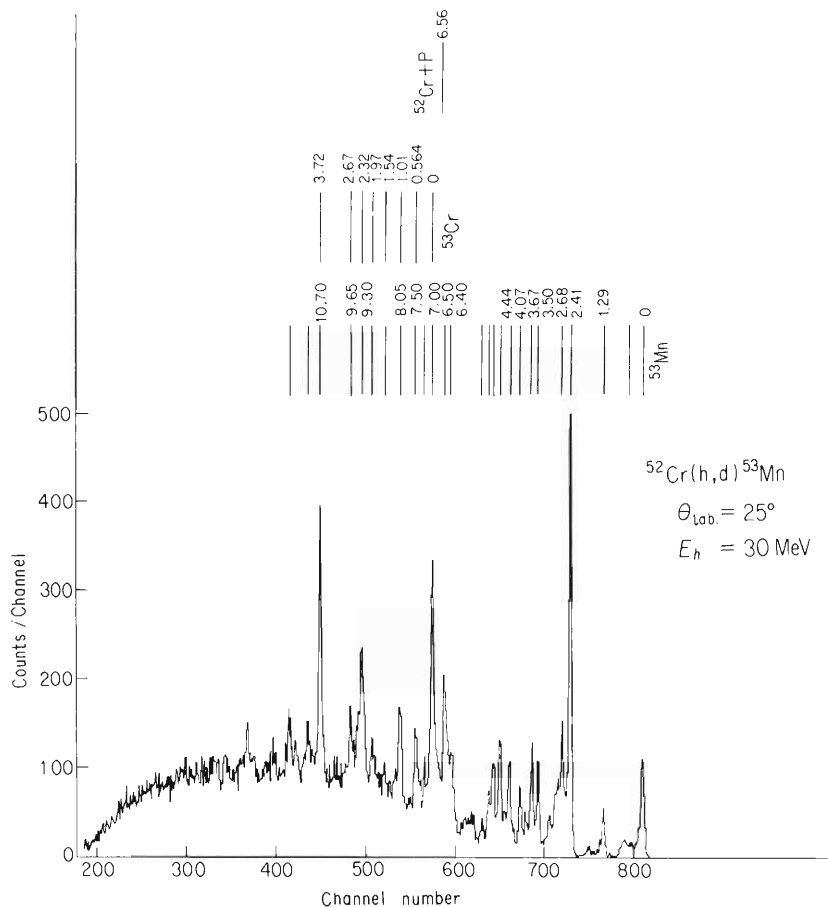


Fig. 1. A deuteron spectrum of the $^{52}\text{Cr}(h,d)^{53}\text{Mn}$ reaction at $E_h=30 \text{ MeV}$ and $\theta_{\text{lab.}} = 25^\circ$.

* Tokyo Institute of Technology.

A typical energy spectrum for $^{52}\text{Cr}(h,d)^{53}\text{Mn}$ is shown in Fig. 1. Several strongly excited states are seen above the Q-value of $^{52}\text{Cr} + p$ including the 9.30 and 9.65 MeV states of ^{53}Mn which were observed by Moses et al. 1) These two states correspond to the 2.32 and 2.67 MeV states of ^{53}Cr respectively. The results for ^{50}Cr and ^{54}Cr are not so much different from those for ^{52}Cr . Angular distributions of emitted deuterons were measured from 10° to 45° . An analysis of the experimental result is now in progress. We are planning to investigate the population of isobaric analog states in the (h,d) reaction and their subsequent proton decay.

Reference

- 1) J.D. Moses, H.W. Newson, and E.G. Bilpuch: Nucl. Phys., A175, 556 (1971).

4-6. The DWBA and Coupled Channel Analyses of Inelastic Scattering of ^3He from ^{12}C

T. Fujisawa, S. Yamaji, K. Matsuda,* S. Motonaga,
F. Yoshida, H. Sakaguchi,** and K. Masui**

The experimental result and optical model analysis of the elastic scattering of ^3He from ^{12}C have been reported previously,¹⁾ and in Table 1 the optical model parameters

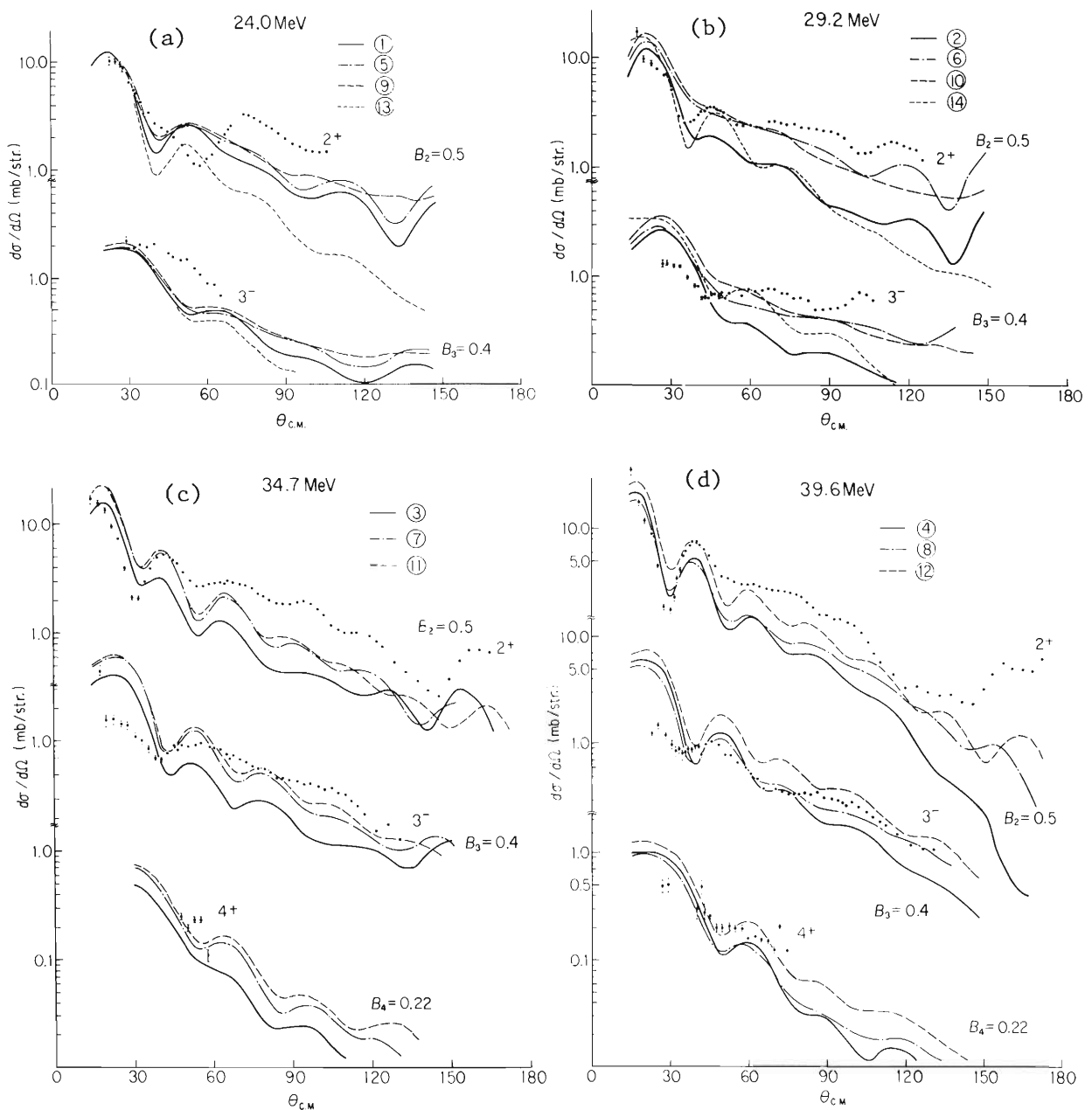


Fig. 1. Angular distributions calculated by the DWBA theory and experimental values. Numbers in circles indicate the potential groups in Table 1.

* Deceased.

** Present address: Department of Physics, Kyoto University.

Table 1. Optical-model parameters that gave best fits. Values of a_{so} γ_{so} are taken equal to those of real part and γ_R is fixed.

Potential number	Incident energy (MeV)	V_0 (MeV)	r_R (fm)	a_R (fm)	W_D (MeV)	r_D (fm)	a_D (fm)	V_{so} (MeV)	θ_{\max} for χ^2 fit	χ^2/N	σ_{Reaction} (mb)
1	24.0	142.3	1.1	.718	13.43	1.314	.823	0	82.5	8.2	1145
2	29.2	135.0	1.1	.700	14.34	1.097	.907	0	72.1	4.5	1116
3	34.7	129.3	1.1	.751	14.72	1.205	.834	0	62.6	17.7	1091
4	39.6	123.0	1.1	.823	17.0	1.416	.657	0	58.5	11.2	1031
5	24.0	141.2	1.1	.656	11.10	1.299	.911	0	129.5	71.2	1192
6	29.2	135.1	1.1	.652	9.468	1.175	1.054	0	127.8	74.8	1237
7	34.7	126.5	1.1	.784	15.33	1.543	.615	0	164.4	62.1	1033
8	39.6	121.2	1.1	.80	14.1	1.268	.787	0	172.2	37.5	1056
9	24.0	139.9	1.1	.681	10.96	1.298	.921	3.61	129.5	67.4	1202
10	29.2	134.0	1.1	.660	10.70	1.323	.882	7.70	127.8	53.1	1131
11	34.7	124.6	1.1	.793	15.14	1.566	.605	4.75	164.4	43.7	1034
12	39.6	124.2	1.1	.808	14.73	1.661	.611	4.48	172.2	28.3	1027
13	24.0	75.1	1.1	.771	9.06	1.424	.886	1.40	129.5	88.0	1167
14	29.2	85.26	1.1	.758	10.70	1.416	.773	8.42	127.8	62.6	1177

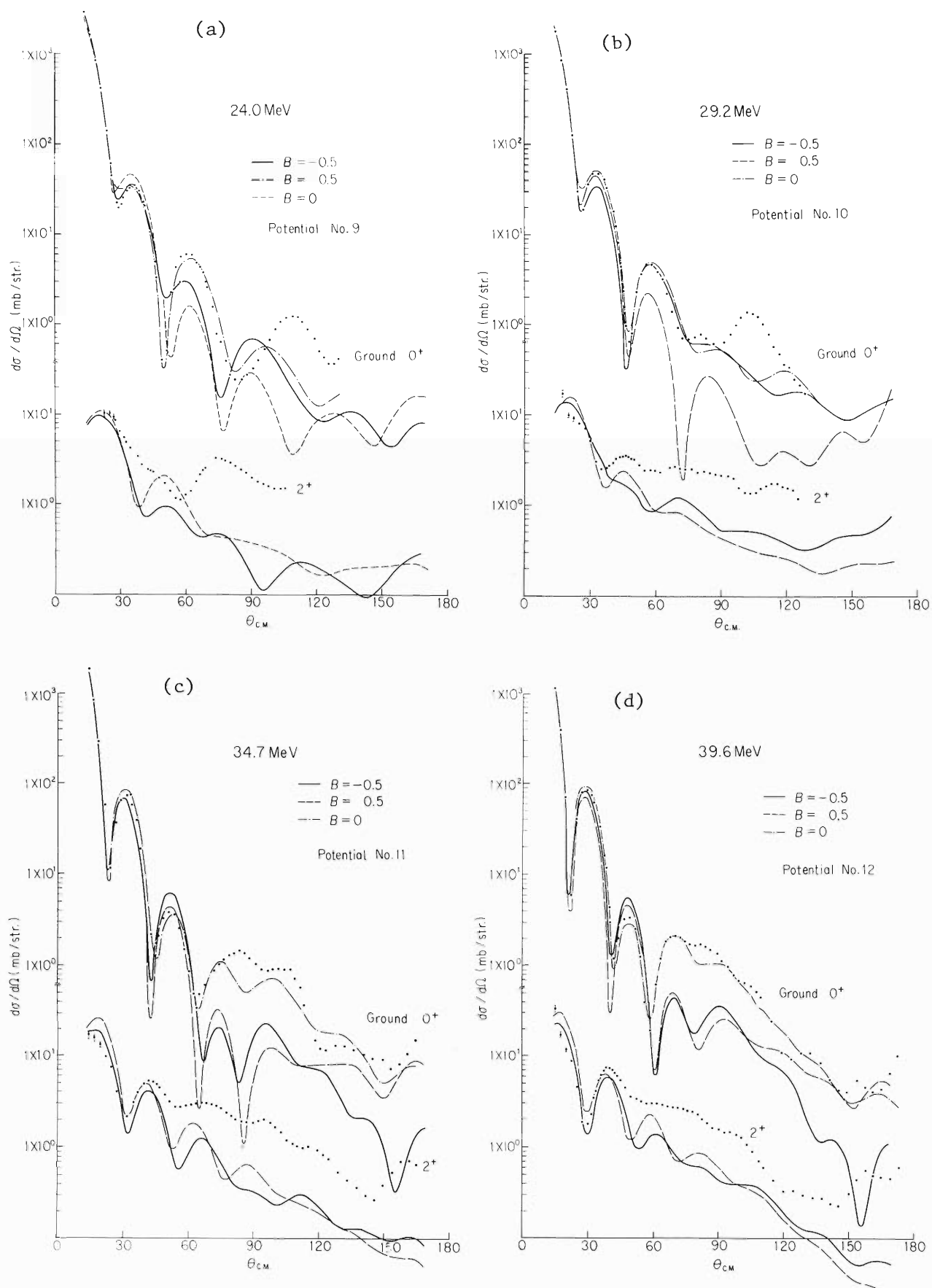


Fig. 2. Angular distributions calculated by the coupled channel theory and experimental values. Numbers indicate the potential groups in Table 1.

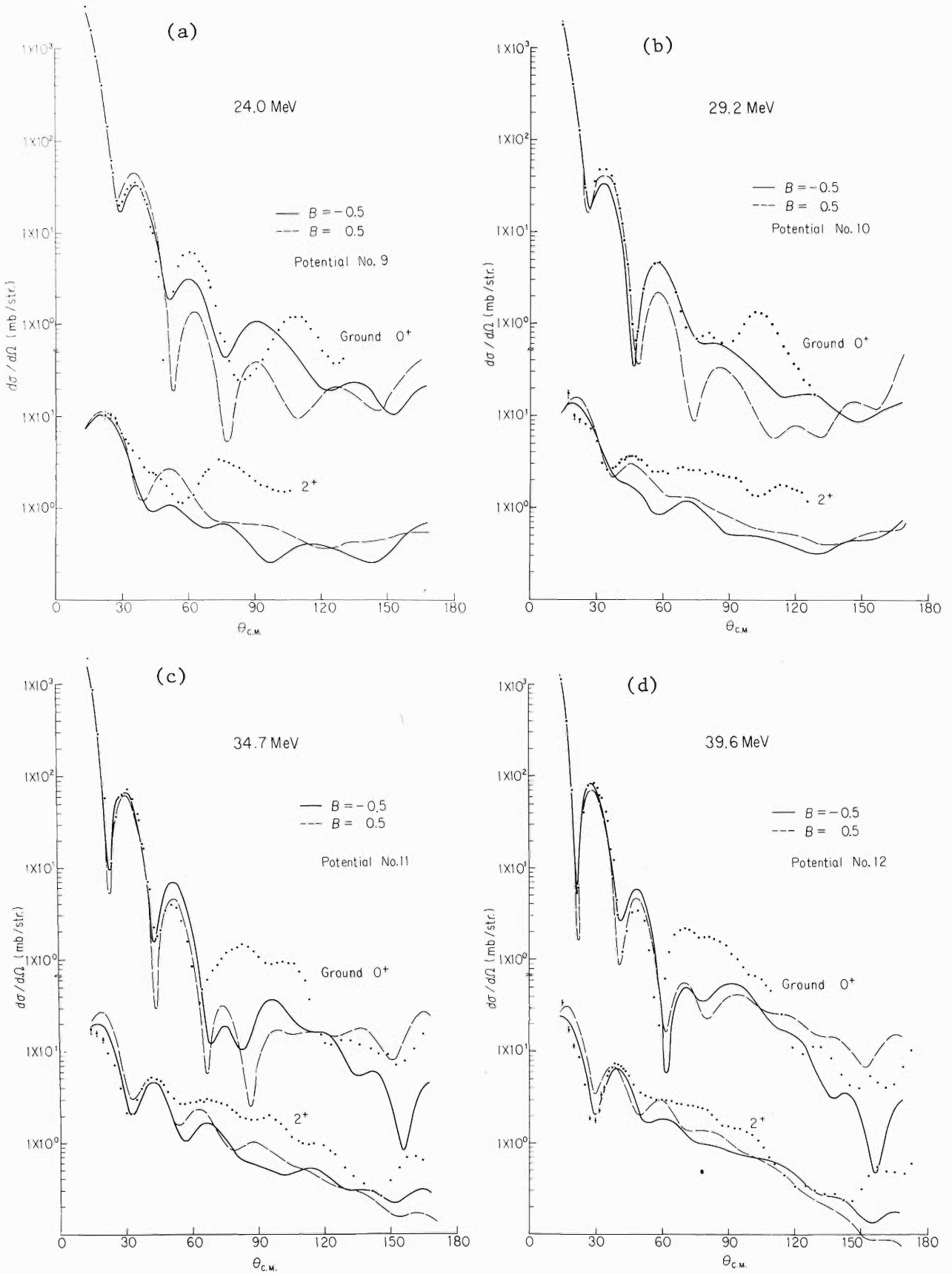


Fig. 3. Angular distributions calculated by the coupled channel theory and experimental values. The depth of the imaginary parts of the potentials are 85% of those indicated by numbers corresponding to Table 1.

were listed. Now the authors describe here analyses of the inelastic scatterings data based on the DWBA and coupled channel theories.

In the calculation of DWBA, the effect of Coulomb potential in the outer region of nucleus was taken into account, because in a preliminary calculation it was found that the prediction of DWBA without the Coulomb potential did not agree with experiments at forward angles. The distortion of spin-orbit potential was of the full Thomas type proposed by Sherif and Blair²⁾ and its value was taken equal to that of real and imaginary potentials. In Fig. 1 the calculated values by DWBA are shown with experimental values. In all the analyses, the potentials with the spin-orbit coupling gave a larger yield than those without the spin-orbit coupling. We can see a difference between the two potentials but cannot say which is better, because the fits are not exact. The values of β_2 , β_3 , and β_4 are about 0.5, 0.4, and 0.22 respectively. It seems that the deformation parameters β_2 and β_3 are too large for the perturbation theory. If we want a more exact calculation, we must consider the coupling between the states.

Formalism of a coupled-channel calculations was presented by Tamura and others and applied successfully to nuclear reactions.^{3)~7)} A coupled-channel analysis of the ground and the first 2^+ states was tried assuming the latter state as a rotational band. In a preliminary calculation, it was found that the effect of Coulomb potential improved the fit at forward angles and the complex form factors were better than the real ones; so in all the analyses the form factors were taken complex and the effect of Coulomb force was included. The assumed values of the coupling coefficient β_2 were ± 0.3 , ± 0.5 , and ± 0.7 in the preliminary calculation, and it seemed that the best value was -0.5 . Figure 2 shows the predicted curve by the coupled-channel calculation using the optical parameters that gave the best fit for elastic scattering. It is remarkable that the predicted elastic scattering cross section was changed appreciably by coupling to the inelastic channel.¹⁾ According to our spin flip experiments of ^3He -particle which excited the first 2^+ state of ^{12}C and the collective DWBA analysis, the spin orbit potential, of which the depth was shallower than that of the best fit potential, gave better fit to the spin flip probability.⁸⁾ Therefore, the calculation with the optical potential, of which the spin-orbit potential depths were 3.5 and 2.5 MeV, were carried out at 39.6 MeV, but the situation was not improved.

It seems reasonable that the depth of imaginary part of the optical potential in the coupled-channel analysis is shallower than in the optical model analysis only of elastic scattering, because the imaginary part means the channel other than the elastic channel and in the coupled-channel analysis the inelastic channel has been included already. The authors found that it is better to take the depth of imaginary potential at about 85 % of the depth given by an optical model analysis. The results are shown in Fig. 3. We see that the elastic channel as well as the inelastic channel is improved and that the negative value of β_2 gives better results at 34.7 and 39.6 MeV. The other authors also reported that the sign of β_2 of ^{12}C was negative in the coupled-channel analysis of the $^{12}\text{C}(p, p')^{12}\text{C}$ reaction or the analysis of the $^{12}\text{C}(\alpha, \alpha')^{12}\text{C}$ reaction with the theory of Austern and Blair.^{6), 9)}

In the analyses FACOM 270/30 and 230/60 computers were used.

References

- 1) T. Fujisawa, H. Kamitsubo, S. Motonaga, K. Matsuda, F. Yoshida, H. Sakaguchi and K. Masui: IPCR Cyclotron Progr. Rep., 4, 46 (1970).
- 2) H. Sherif and J.S. Blair: Phys. Letters, 26B, 489 (1968).
- 3) T. Tamura: Rev. of Modern Phys., 37, 679 (1965).

- 4) R.L. Robinson, J.L.C. Ford, Jr., P.H. Stelson, T. Tamura, and C.Y. Wong: Phys. Rev., 187, 1609 (1969).
- 5) N. Lingappa and G.W. Greenless: Phys. Rev., C2, 1329 (1970).
- 6) O. Mikoshiba, T. Terasawa, and M. Tanifuji: Nucl. Phys., A168, 417 (1971).
- 7) T. Tamura: ORNL-4152 unpublished computer program Jupiter 1 for coupled-channel calculation; M. Wakai, S. Igarashi, O. Mikoshiba, and S. Yamaji: JAERI-memo, p. 3833 (1969).
- 8) T. Fujisawa, S. Motonaga, H. Kamitsubo, Y. Chiba, and T. Wada: IPCR Cyclotron Progr. Rep., 5, 44 (1971).
- 9) J. Specht, G.W. Schweimer, H. Rebel, G. Schatz, R. Lönken, and G. Hauser: Nucl. Phys., A171, 65 (1971).

4-7. $^{20}\text{Ne}(d, ^6\text{Li})^{16}\text{O}$ Reaction

M. Odera, S. Takeda, and S. Nakajima

$^{20}\text{Ne}(d, ^6\text{Li})$ reaction was investigated as a part of study of the α pick-up reactions from s-d shell nuclei.¹⁾ The energy of deuteron was 23.5 MeV. The pressure in the gas target was read by an α -tron gauge.²⁾ The absolute value was obtained using a conversion factor for neon given in the manual of the gauge. The pressures in the vicinity of 50 Torr were used throughout. The Q-value of the reaction is -3.26 MeV. The particle identification system was described previously.¹⁾

Figure 1 shows the spectra from neon and oxygen and Fig. 2 shows the angular distributions obtained. The 6.03 MeV 0^+ and 6.14 MeV 3^- states of oxygen were not resolved. Unfortunately, in the peak corresponding to 6.91 MeV 2^+ of ^{16}O , those peaks from 1.98 MeV 2^+ of ^{18}O originated from ^{22}Ne and from 4.43 MeV 2^+ state of ^{12}C originated from ^{16}O seem to be mixed. Lack of oscillation of the angular distribution may stem from this mixing.

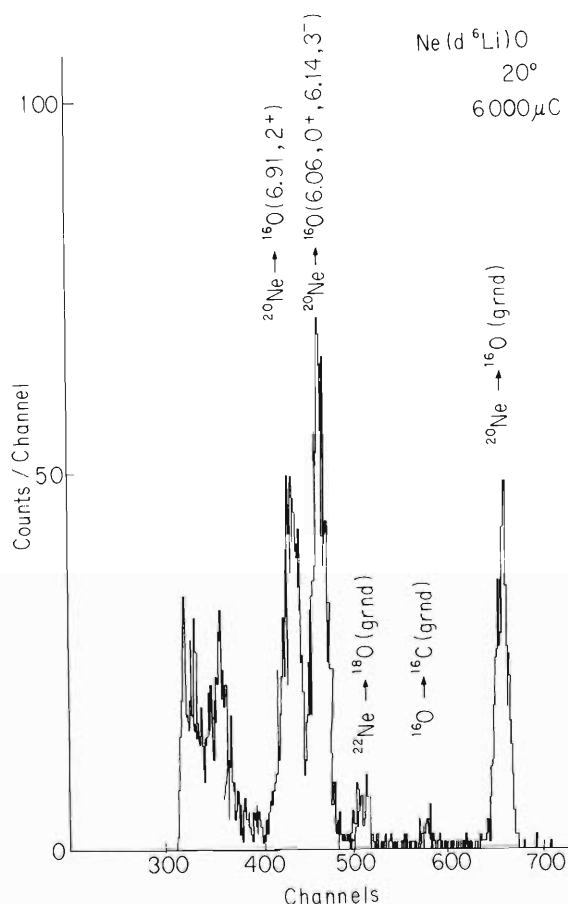


Fig. 1. (a) ^6Li spectrum of $\text{Ne}(d\ ^6\text{Li})\text{O}$ reaction at laboratory angle of 20° .

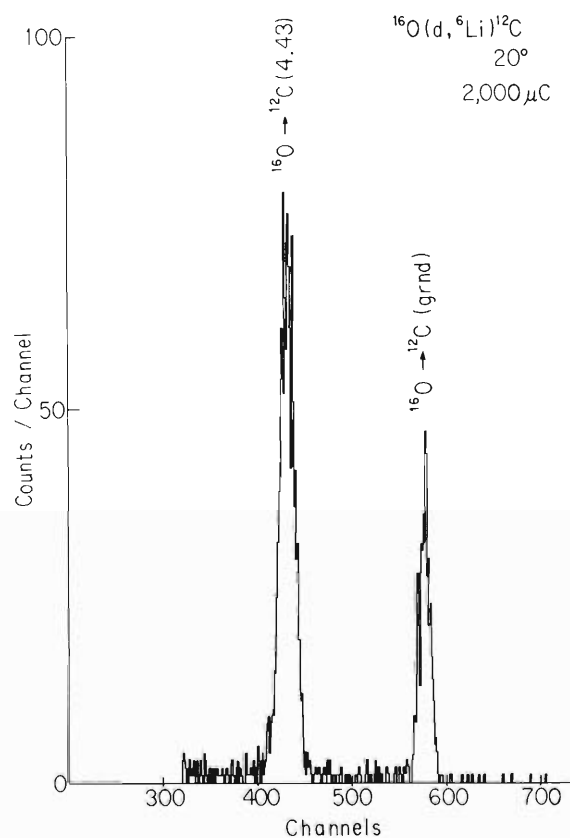


Fig. 1. (b) ^6Li spectrum of $^{16}\text{O}(d\ ^6\text{Li})^{12}\text{C}$ reaction at laboratory angle of 20° .

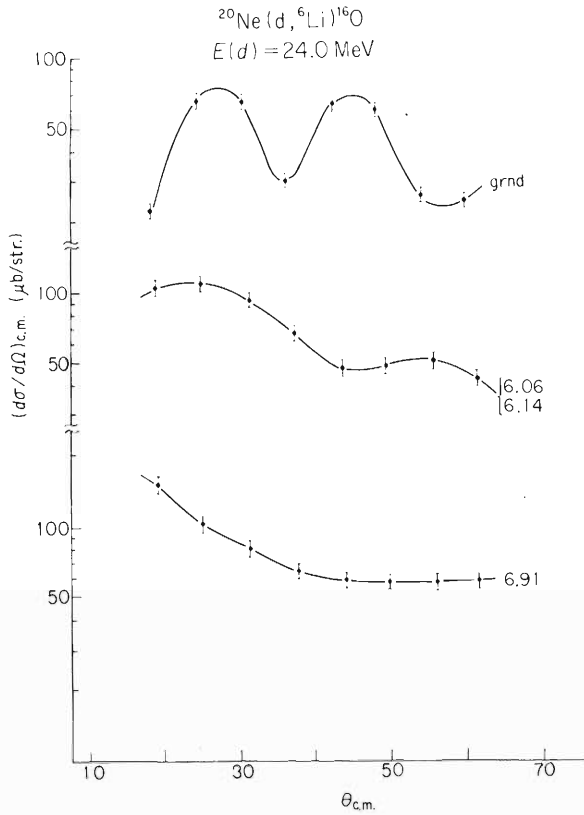


Fig. 2. Experimental angular distributions obtained for $^{20}\text{Ne}(d, ^6\text{Li})^{16}\text{O}$ reactions. Numbers for each curve indicate the states of residual ^{16}O nucleus.

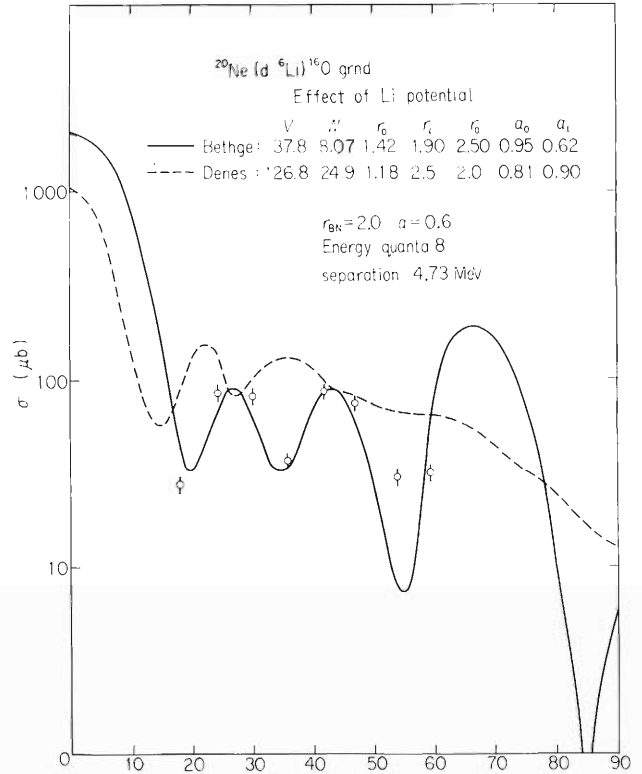


Fig. 3. Zero-range DWBA fit of the ground state transfer. Effects of Li potential are compared. Optical parameters of the deuteron channel are $V = 92.2$, $W = 35.8$, $r_V = 0.965$, $r_W = 1.46$, $a_V = 0.89$, $a_W = 0.813$, $r_C = 1.30$.

Figure 3 shows the zero-range DWBA fit of the ground state transition based on the simple-minded α cluster transfer assumption.^{1), 3)} Fit of 2nd peak assuming pick-up from p-shell has failed completely in this simple prescription.

References

- 1) M. Odera, S. Takeda, and I. Kohno: IPCR Cyclotron Progr. Rep., 4, 29 (1970).
- 2) Alphatron type 820. Norton Vacuum Equip. Div. 160 Charlemont St. Newton. Mass. USA.
- 3) L.J. Denes, W.W. Dehnick, and M. Drisko: Phys. Rev., 148, 1097 (1966).

4-8. Inelastic Scattering for the Giant Resonance States

H. Kamitsubo, T. Wada, T. Fujisawa, T. Inanaga,
M. Koike, and T. Mikumo

Recent experiments¹⁾ of electron scattering at Tohoku University have shown an evidence for the excitation of the giant resonance states of dipole and quadrupole type in closed shell nuclei. They have also observed that many states above 10 MeV were

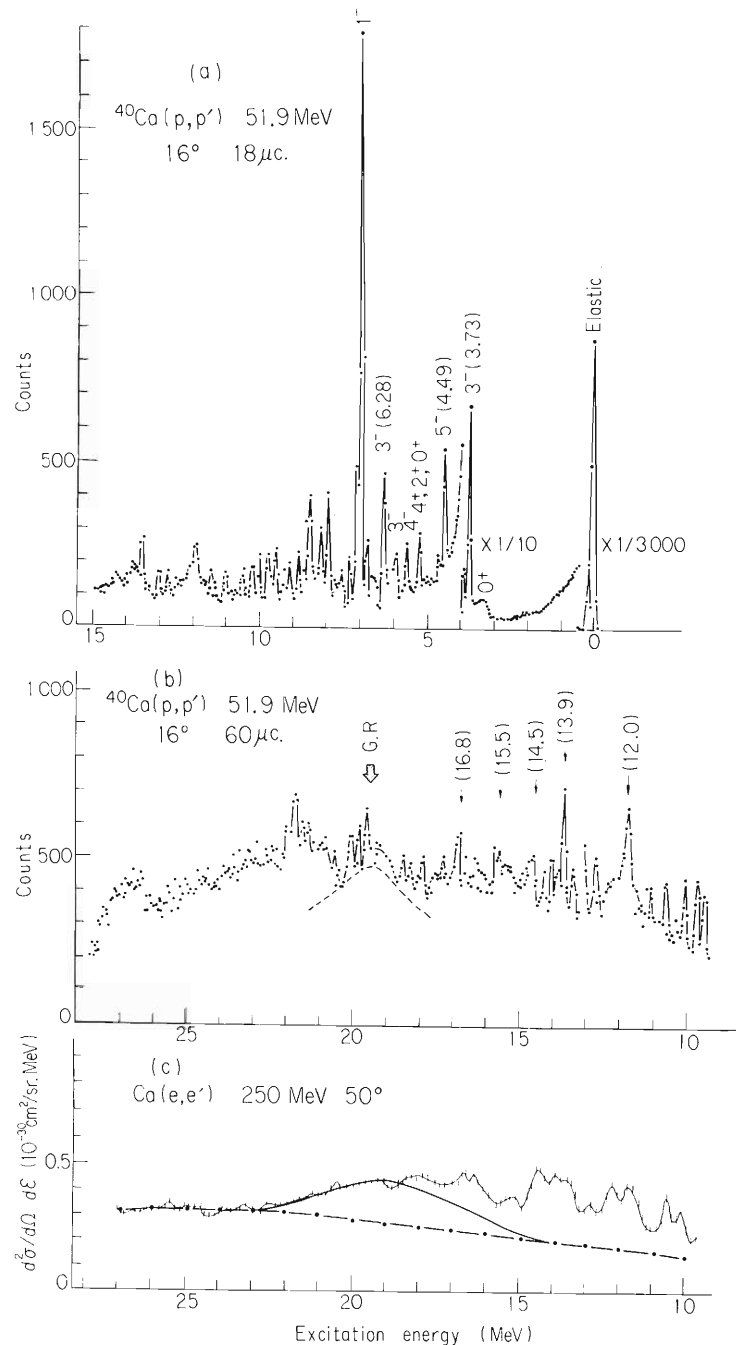


Fig. 1. Energy Spectra of 52 MeV protons from ^{12}C target. They were measured at two different field strengths of the particle analyzer (a and b). One of the electron spectra obtained at Tohoku University is also shown for comparison (c).

excited strongly and most of them seem to have E2 character. In this laboratory, we made a plan to study these states by means of inelastic scattering of 50 MeV alpha-particles from the cyclotron and also 52 MeV protons from the FM cyclotron at INS, Tokyo University, for the purpose of obtaining more definite information on these states.

It was shown²⁾ that by comparing results of the inelastic scattering of protons and alphas, one can get spin flip and iso-spin flip components in the transitions to those states. It is also expected that we can determine their spins, parities, and reduced transition probabilities from angular distribution measurements by applying a correct distorted wave approximation.³⁾

However there are some difficult problems in obtaining accurate inelastic scattering cross sections for such highly excited states. In the particle spectrum over the energy range of our interest, backgrounds due to a weak stray beam can be added. Therefore the beam must be carefully aligned and a slit system must be used. Also low energy particles scattered by the contamination of light elements in the target become large sources of errors. In the α -scattering experiments with some target elements, large peaks due to the in-flight decay of ^5He and ^5Li formed in the pick-up process was observed in the same energy range as the giant resonance states.⁴⁾

We measure energy-spectra of 52 MeV protons from ^{12}C , ^{40}Ca , ^{51}V , Cu(natural), and ^{208}Pb in order to examine the above technical and physical problems. The scattered protons were detected with the INS particle analyzer system. We observed the broad peaks which correspond to the giant resonance states in ^{12}C and ^{40}Ca but could not obtain any positive evidence of the excitation of those states in other nuclei. These spectra are used as the standards for the α -scattering experiment. Figure 1 shows the proton spectra from a Ca target. The electron spectrum obtained at Tohoku University is also shown for comparison. Above 10 MeV one can see many sharp peaks and some broad ones, most of which are also observed in electron scattering. Further study by 52 MeV protons and 50 MeV alphas are in progress.

References

- 1) Y. Torizuka, Y. Kojima, T. Saito, K. Itoh, A. Nakada, S. Mitsunobu, M. Nagao, K. Hosoyama, and S. Fukuda: Proc. Int. Conf. Photoreaction, Sendai (1972).
- 2) Y. Awaya, K. Matsuda, T. Wada, N. Nakanishi, S. Takeda, and S. Yamaji: J. Phys. Soc. Japan, 33, 881 (1972).
- 3) G.R. Satchler: Nucl. Phys., A195, 1 (1972).
- 4) G. Chenevert, N.S. Chant, I. Halpern, C. Glashausser, and D.L. Hendrie: Phys. Rev. Letters, 27, 434 (1971).

4-9. Effect of Exchange Currents on Orbital g-Factors

S. Yamaji, M. Hirata,* and J. Fujita**

Recently a simple relation was derived by the authors between the change of orbital g-factors due to exchange currents and the sum rule for E1 photoabsorption on the basis of an assumption that the momenta of nucleons inside a nucleus have the Fermi-type distribution;¹⁾

$$2 (\delta g_{\ell}^p)_{\text{exch.}} = \kappa (\approx 0.4) \text{ for } N \approx Z, \text{ in which } \kappa \text{ is defined by}$$

$$\int \sigma \gamma(E1) dw = (\pi^2 \alpha^2 A / 2M) (1 + \kappa)$$

The purpose of this note is to reexamine the validity of the above relation by use of a shell model. In Table 1 the results of the zeroth-order shell calculation are shown for $\hbar\omega = 41 A^{-1/3}$ MeV.

Table 1. (For Rosenfeld mixture, we use $V = -28$ MeV and $r_0 = 1.414$ fm)

Nucleus	Nuclear force	OPEP		Rosenfeld	
		δg_{ℓ}	κ	δg_{ℓ}	κ
¹⁵ N	p 1/2 ⁻¹ (p)	0.116	0.196	0.232	0.393
¹⁷ O	d 5/2 (n)	-0.064	0.199	-0.129	0.399
³⁹ K	d 3/2 ⁻¹ (p)	0.108	0.196	0.217	0.395
⁴¹ Ca	f 7/2 (n)	-0.069	0.199	-0.139	0.399
⁸⁷ Sr	g 9/2 ⁻¹ (n)	-0.068	0.187	-0.137	0.375
⁸⁹ Y	p 1/2 (p)	0.160	0.187	0.320	0.376
⁸⁹ Y	g 9/2 (p)	0.083		0.166	
⁹¹ Zr	d 5/2 (n)	-0.087	0.188	-0.175	0.377
²⁰⁷ Pb	p 1/2 ⁻¹ (n)	-0.122	0.183	-0.244	0.367
²⁰⁹ Bi	h 9/2 (p)	0.099	0.183	0.199	0.367

* Department of Physics, Hiroshima University.

** Department of Physics, Tokyo University of Education.

From this Table we can draw several conclusions that a) the relation $\kappa / |\delta g_\ell| \approx 2$ holds approximately; b) the one-pion exchange potential (OPEP) explains only half of the $\kappa_{\text{exp.}} \approx 0.4$; c) for heavy nuclei, the isoscalar part of δg_ℓ is important.

The point b) arises from the fact that the central space-exchange part of the OPEP is weaker by a factor of 2 than that of the phenomenological nuclear potential such as the Rosenfeld force which can explain that $\kappa \approx 0.4$. However, it should be noticed that the tensor part of the OPEP is partly changed into the central potential as the second-order effects;

$$V_{\text{central}}^{\text{eff.}} \approx (\tau\tau) \frac{2 \langle V_T^2 \rangle}{\Delta \epsilon} P_{\text{triplet.}}$$

It is already known²⁾ that the effective value of the energy denominator is about 240 MeV. In order to study this effect, we carried out the first-order perturbation calculation for the configuration mixing with $2 \hbar\omega$ jumps. The results are shown in Table 2.

Table 2

Nucleus	$\Delta(\delta g_\ell)$	$\Delta\kappa$
^{15}N	-0.0016	0.011
^{17}O	-0.00022	0.011

Actually the effect of configuration mixing due to tensor forces is seen to be small in so far as the lower levels are concerned.

Finally it should be remarked that, in order to compare our results with experiments, we must subtract the second-order effects (mainly normalization effects) $(\delta g_\ell)'$ from the above $(\delta g_\ell)_{\text{exch.}}$

References

- 1) J.I. Fujita and M. Hirata: Phys. Letters, 37B, 237 (1971);
J.I. Fujita, S. Yamaji, and M. Hirata: J. Phys. Soc. Japan, 33, 541 (1972).
- 2) G.E. Brown: "Unified Theory of Nuclear Models", 2nd. ed., North-Holland, Amsterdam (1967).

4-10. Total Energy Surface for ^{236}U in the Two-Center Model

S. Yamaji, S. Suekane,*
and K. Harada**

A two-center model has recently been developed by Greiner et al.^{1)~5)} This model allows a smooth transition from the ground state of one nucleus to a system of two completely separated fragment nuclei and is suitable for the description of fission phenomena.^{6)~8)} We have made the computation code for the model including the spin-orbit interaction and by using it we have calculated the total energy surface for ^{236}U .

The Hamiltonian of this model is

$$H = T + \frac{m}{2} \left\{ \begin{array}{l} \omega_{1z}^2 (z-z_1)^2 + \omega_{1\rho}^2 \rho^2 \\ \omega_{2z}^2 (z-z_2)^2 + \omega_{2\rho}^2 \rho^2 \end{array} \right. - \kappa \hbar \left\{ \begin{array}{l} \tilde{\omega}_{10} [2(\vec{\ell} \cdot \vec{s}) + \mu \{ \vec{\ell}^2 - \frac{1}{2} (n_{1z} + 2n_{\rho} + |n_{\varphi}|) (n_{1z} + 2n_{\rho} + |n_{\varphi}| + 3) \}] z \geq 0 \\ \tilde{\omega}_{20} [2(\vec{\ell} \cdot \vec{s}) + \mu \{ \vec{\ell}^2 - \frac{1}{2} (n_{2z} + 2n_{\rho} + |n_{\varphi}|) (n_{2z} + 2n_{\rho} + |n_{\varphi}| + 3) \}] z < 0, \end{array} \right. \quad (1)$$

where

$$\tilde{\omega}_{i0} = \omega_{iz} \left(1 - \frac{4}{3} \delta_i\right)^{-1/3} \left(1 + \frac{2}{3} \delta_i\right)^{1/3} \quad (i=1, 2), \quad (2)$$

$$\delta_i = \frac{3}{2} \frac{\beta_i^2 - 1}{2\beta_i^2 + 1} \quad (i=1, 2), \quad (3)$$

$$\beta_i = \frac{\omega_{i\rho}}{\omega_{iZ}}, \quad (4)$$

Six shape parameters $\omega_{1\rho}$, $\omega_{2\rho}$, ω_{1z} , ω_{2z} , z_1 , z_2 are expressed with the deformation parameters of fragment nuclei β_1 and β_2 , the center separation z_0 , the mass ratio $\alpha (= A_1/A_2)$, the mass of the parent nucleus A , the nuclear radius parameter r_0 and the oscillator parameter $\tilde{\omega}_0$ by the following six conditions:

- (i) The nuclear surface is continuous at the matching plane $z = 0$.
- (ii) $z_0 = z_1 - z_2$. (5)
- (iii) The volume conservation is applied for the equipotential surface that coincides with the nuclear surface.
- (iv) The volume ratio is equal to the mass ratio α .

* Osaka City University.

** Japan Atomic Energy Research Institute.

$$(v) \quad \beta_1 = \omega_{1\rho} / \omega_{1z}.$$

$$(vi) \quad \beta_2 = \omega_{2\rho} / \omega_{2z}.$$

This Hamiltonian is solved by diagonalization in the basis of eigenstates of a corresponding two-center oscillator potential that meets the requirement

$$\omega_{\rho}^2 = (\omega_{1\rho}^2 + \omega_{2\rho}^2) / 2,$$

$$H^0 = T + \frac{m}{2} \omega_{\rho}^2 \rho^2 + \frac{m}{2} \begin{cases} \omega_{1z}^2 (z-z_1)^2 & z \geq 0 \\ \omega_{2z}^2 (z-z_2)^2 & z < 0. \end{cases} \quad (6)$$

The notations n_{iz} , n_{ρ} , n_{φ} of Eqn. (1) are used for quantum numbers of eigenstates of Eqn. (6).

The total energy E_{tot} is given by

$$E_{\text{tot}} = E_S + E_V + E_{\text{cm}} + E_C \quad (7)$$

where E_S , E_V , and E_{cm} are the simple sum, the virial term and the correction of the center-of-mass motion. They are expressed as follows.

$$E_S = \frac{3^{\text{occ}}}{4} \sum_{\lambda} \epsilon_{\lambda}, \quad (8a)$$

$$E_V = \frac{1}{4} \left(2 \sum_{\lambda} t_{\lambda} - \sum_{\lambda} \epsilon_{\lambda} \right), \quad (8b)$$

$$E_{\text{cm}} = -\frac{1}{A} \left(\sum_{\lambda} t_{\lambda} + \sum_{\lambda\mu}^{\text{occ}} \langle \varphi_{\lambda} \varphi_{\mu} \left| \frac{\vec{P}_1 \cdot \vec{P}_2}{2m} \right| \varphi_{\lambda} \varphi_{\mu} \rangle_{\text{antsym}} \right). \quad (8c)$$

Coulomb energy E_C was calculated by Beringer's method.⁹⁾ The notations ϵ_{λ} and ϕ_{λ} stand for the eigenvalue and the eigenfunction of Eqn. (1), and t_{λ} represents the expectation value of the kinetic energy operator $p^2/2m$ of the eigenstate ϕ_{λ} .

The total energy surface for ^{236}U was calculated in the frame-work of the symmetric two-center model. The energy surface in this symmetric case can be shown in a two-dimensional representation as a function of two parameters β ($=\beta_1 = \beta_2$) and z_0 . The nuclear radius parameter r_0 and the oscillator parameter $\hbar \tilde{\omega}_0$ were taken to be 1.2 fm and $41 A^{-1/3}$ ($= 6.63458$) MeV, respectively. The values of the spin-orbit parameters κ and μ are the same as those of Ref. 4). The diagonalization was performed with single particle states which had the principal quantum number $N \leq 10$.

The total energy surface in the case of $\delta = 0.0$ is shown in Fig. 1. The correction term E_{cm} was not calculated.

It is seen that the present calculation reproduces the experimental fission barrier height ($E_{\text{bar}} = 5.8$ MeV) fairly well. The virial term E_V plays an important role in giving a reasonable barrier height, though the result of Albrecht et al.⁴⁾ which corresponded to $(E_S + E_C)$ gave too high barrier height. This conclusion was pointed out by Maharry and Davidson⁷⁾ and also obtained by our exact treatment of the spin-orbit interaction and the ℓ^2 term.

In order to see the behavior of the terms E_S and E_V in the cases of $\delta = -0.38, 0.0, 0.38$ the magnitude of each term is shown in Fig. 2, separately. In Fig. 3, the total nuclear energy surface is shown as a function of two parameters δ and z_0 .

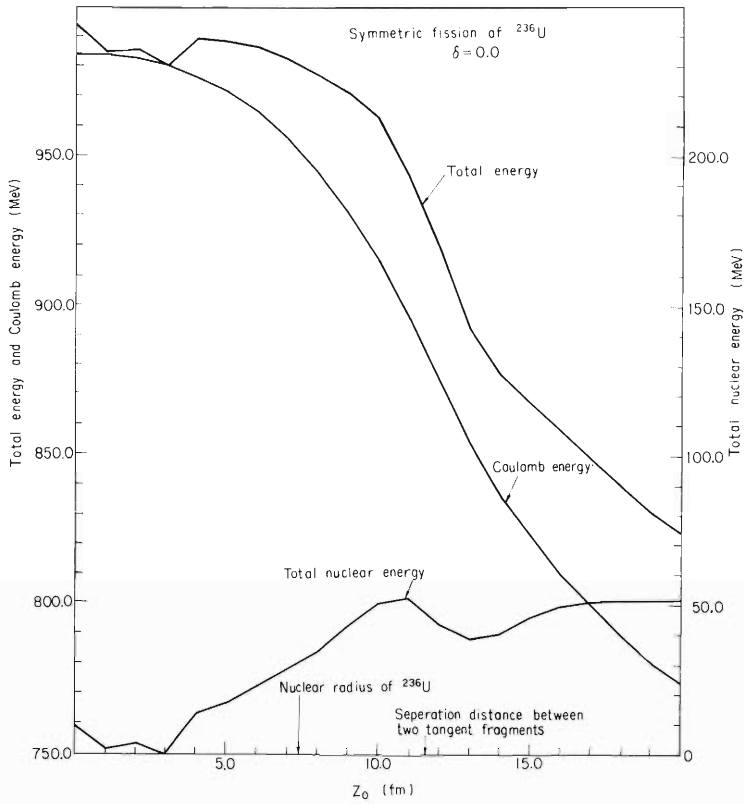


Fig. 1.
 The energy surface of ^{236}U in the symmetric two-center model. The total nuclear energy which is the sum of the terms E_S , E_V , and E_{cm} at $z_0 = 3.0$ fm was set to be 0.0 MeV. The term E_{cm} was neglected. Coulomb energy was calculated with the assumption that the density distribution was the same as the two-center potential.

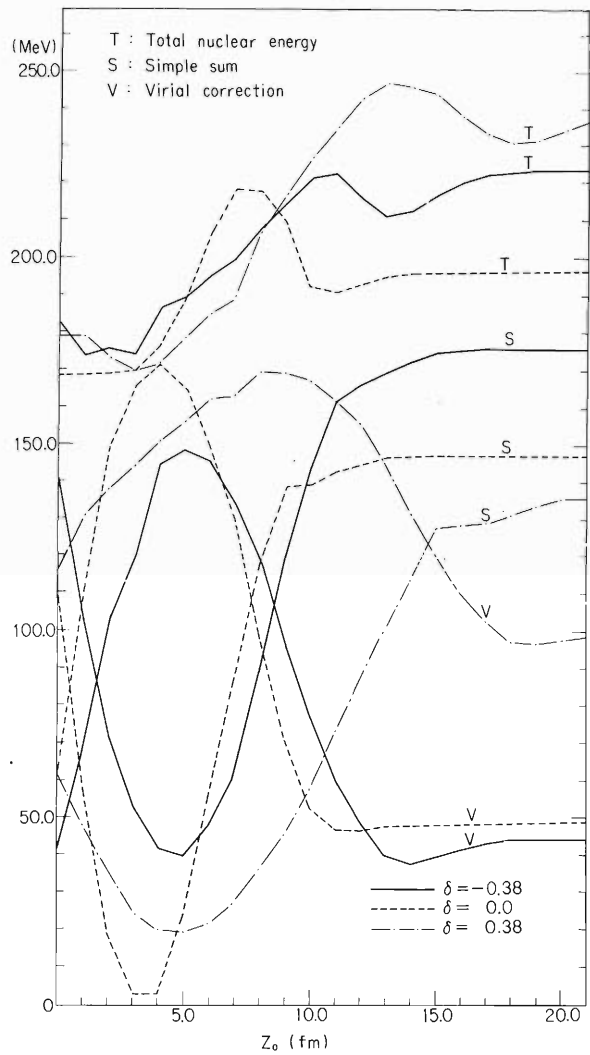


Fig. 2.
 The total nuclear energy and its components, the simple sum E_S and the virial term E_V .

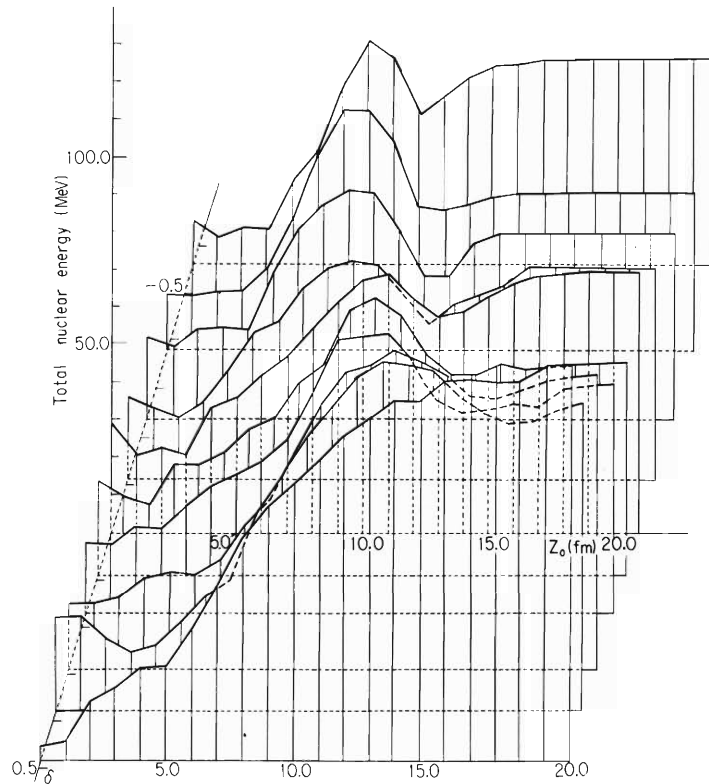


Fig. 3. The total nuclear energy surface as a function of the deformation parameter of each fragment nucleus δ and the center separation z_0 .

As the second barrier has disappeared in inclusion of the Coulomb energy E_C as is seen from Fig. 1, a more careful treatment of the Coulomb energy seems to be necessary. The study of the nuclear fission based on the asymmetric two-center model in which the potential shape is improved by rounding the neck is now in progress.

References

- 1) P. Holzer, U. Mosel, and W. Greiner: Nucl. Phys., A138, 241 (1969).
- 2) D. Scharnweber, U. Mosel, and W. Greiner: Phys. Rev. Letters, 24, 601 (1970).
- 3) K. Albrecht, D. Scharnweber, W. Greiner, and U. Mosel: Phys. Letters, 32B, 229 (1970).
- 4) D. Scharnweber, W. Greiner, and U. Mosel: Nucl. Phys., A164, 257 (1971).
- 5) U. Mosel, J. Maruhn, and W. Greiner: Phys. Letters, 34B, 587 (1971).
- 6) U. Mosel and H.W. Schmitt: Nucl. Phys., A165, 73 (1971).
- 7) D.E. Maharry and J.P. Davidson: Nucl. Phys., A183, 371 (1972).
- 8) M.G. Mastafa, U. Mosel, and H.W. Schmitt: Phys. Rev. Letters, 28, 1536 (1972).
- 9) R. Beringer: Phys. Rev., 131, 1402 (1963).

4-11. On the Mechanism of (${}^3\text{He}, t$) Reaction

M. Toyama

A number of experiments on the (${}^3\text{He}, t$) reaction have been done recently and interesting facts have been pointed out. In particular, the excitation of isobaric analog of the target ground state (hereafter referred to as GIAS-excitation) has been interpreted with apparent success by means of DWBA with quasi-elastic charge exchange mechanism. However, the DWBA analyses of other (${}^3\text{He}, t$) reactions on the assumption of charge exchange mechanism exhibited many serious problems.

(1) A very large deformation parameter for the Lane potential is needed in order to account for the scattering to excite the analog of the first excited 2^+ states of the target nucleus¹⁾ (hereafter referred to as 2^+ IAS-excitation).

(2) The strength of the iso-spin part of the effective two-body interaction is required to depend strongly on the transferred angular momentum, I_t , in order to account for the magnitude of the observed cross section for exciting the configuration states.^{2), 3)}

(3) For the excitation of anti-analog states, the positions of peaks and valleys in the angular distribution disagree entirely with the calculated ones.⁴⁾

(4) GIAS-excitation was observed at a few energy points and analyzed by DWBA using microscopic form factors.⁵⁾ The strength of the two-body interaction potential needed to account for the observed magnitude of the cross section is strongly dependent on the incident energy.

These problems cast serious doubt on the applicability of a conventional DWBA to the analyses of (${}^3\text{He}, t$) reactions. Alternative mechanisms have been proposed to save the difficulties. For the first problem it was pointed out that the two-step process via the first excited 2^+ states or the analog state of the target ground state is important.^{6)~8)} For the second and the third problems it was found in case of ${}^{48}\text{Ca}({}^3\text{He}, t){}^{48}\text{Sc}$ or ${}^{40}\text{Ar}({}^3\text{He}, t){}^{40}\text{K}$ that the two-step process, (${}^3\text{He}-\alpha-t$), is important.^{9)~11)} In this process the projectile picks up a neutron to become an α -particle in the first step and then the α -particle is stripped of a proton to become a triton which is emitted. In the Ref. 9), 10), and 11), it was also pointed out that the two-step process, (${}^3\text{He}-\alpha-t$), is important even in the quasi-elastic scattering. For the fourth problem the DWBA analysis with a complex effective potential gives an agreement with the observed cross sections.¹²⁾

The purpose of the present paper is to investigate the (${}^3\text{He}-\alpha-t$) mechanism further, especially to answer the following questions.

A. In the excitation of configuration states, is it generally true for any target that the I_t dependence of the potential strength required in the DWBA fitting for the experiment is mostly due to the (${}^3\text{He}-\alpha-t$) process?

B. Do the cross sections of GIAS-excitation due to the two-step process, (${}^3\text{He}-\alpha-t$), have the proportionality to the number of excess neutrons, $(N-Z)$?

C. Can the magnitude of observed cross sections of GIAS-excitation be accounted for

if the coherent sum of the DWBA and (${}^3\text{He}-\alpha-t$) amplitudes are used for the scattering amplitude?

D. Can the energy dependence of the potential strength in DWBA with a real reaction potential be removed by taking into account the two-step process?

In this paper these problems are investigated by analyzing the data on ${}^{46,48,50}\text{Ti}({}^3\text{He}, t){}^{46,48,50}\text{V}$ at $E_{{}^3\text{He}} = 24.6$ MeV,¹³⁾ ${}^{90}\text{Zr}({}^3\text{He}, t){}^{90}\text{Nb}$ at $E_{{}^3\text{He}} = 21.7, 29.7,$ and 37.5 MeV,⁵⁾ and ${}^{90}\text{Zr}({}^3\text{He}, t){}^{90}\text{Nb}$ at $E_{{}^3\text{He}} = 21$ ¹⁴⁾ and 37.7 MeV³⁾ using the second order perturbation theory for calculating the (${}^3\text{He}-\alpha-t$) process.⁹⁾ In the Ref. 7) and 9), a perturbation method is used. According to the Ref. 8) and 11), the difference in the numerical results between the perturbation method and the coupled channel method is not large for these reactions.

In these calculations, the Blatt-Jackson potential of Gaussian type¹⁵⁾ was used as the effective nucleon-nucleon interaction for the DWBA term. The normalization factor D_0 in the zero-range approximation for the two-step process was taken to be that given by Ref. 16) obtained from the analysis ${}^{54}\text{Cr}({}^3\text{He}, \alpha){}^{53}\text{Cr}$ at $E_{{}^3\text{He}} = 18$ MeV.

The results of calculations are shown in Figs. 1 through 4. In each of these figures, the dotted line represents the calculated cross section given by the DWBA term only and the broken line represents the one given by the two-step process, (${}^3\text{He}-\alpha-t$), only and the full line represents the coherent sum of the two. These seem to indicate that the two-step process, (${}^3\text{He}-\alpha-t$), is the main process in some of the (${}^3\text{He}, t$) reactions. The answers to the questions A through D seem to be the following:

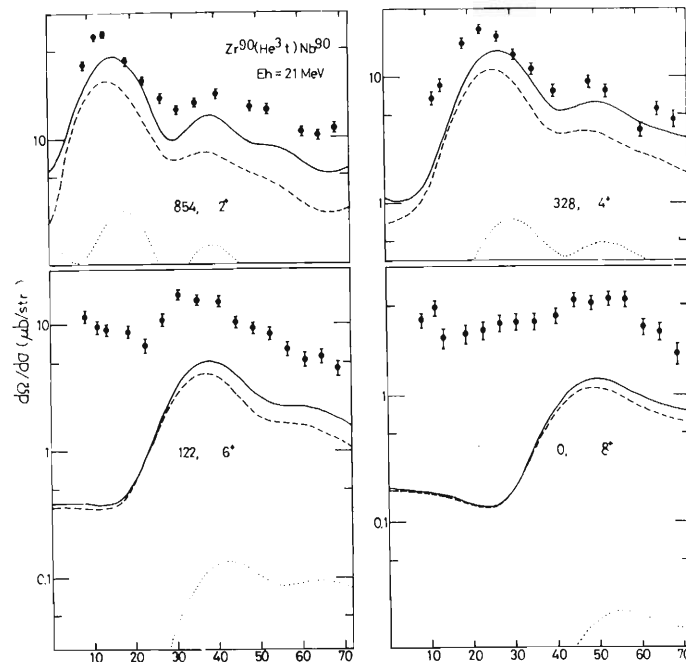


Fig. 1. Differential cross sections for the ${}^{90}\text{Zr}({}^3\text{He}, t){}^{90}\text{Nb}(2^+, 4^+, 6^+, 8^+)$ reaction at $E_{{}^3\text{He}} = 21$ MeV. The dotted line represents the calculated cross section given by the DWBA term only and the broken line represents the one given by the two-step process, (${}^3\text{He}-\alpha-t$), only, and the full line represents the coherent sum of the two.

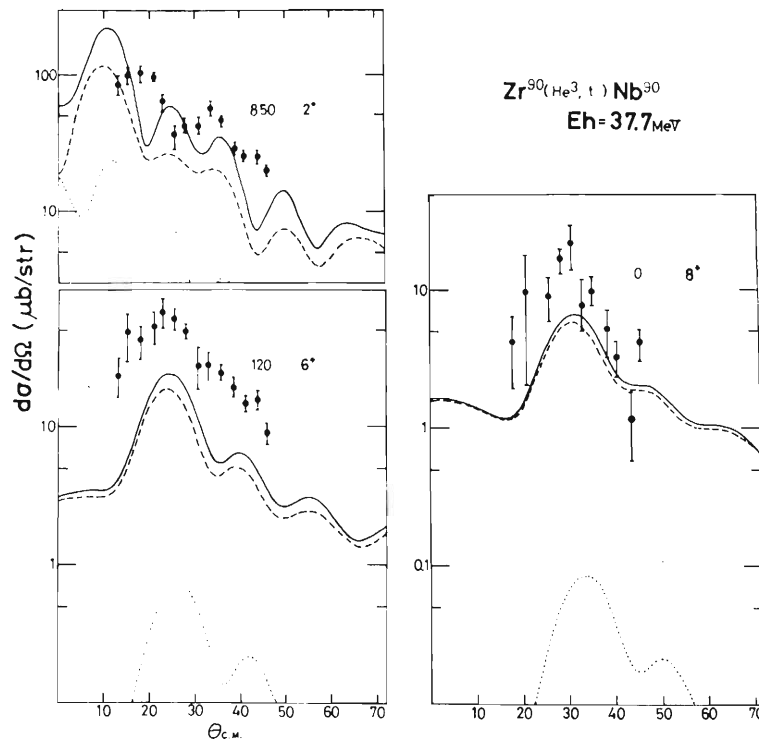


Fig. 2. Differential cross sections for the $^{90}\text{Zr}(^3\text{He}, t)^{90}\text{Nb}(2^+, 6^+, 8^+)$ reactions at $E_{^3\text{He}} = 37.7$ MeV.

A'. In the excitation of configuration states with even spin, it is true not only for $^{48}\text{Ca}(^3\text{He}, t)^{48}\text{Sc}$ but also for $^{90}\text{Zr}(^3\text{He}, t)^{90}\text{Nb}$ that the I_t dependence of the potential strength required in the DWBA fitting for the experiment is mostly due to the $(^3\text{He}-\alpha-t)$ process.

B'. The cross sections given by the two-step process, $(^3\text{He}-\alpha-t)$, for GIAS-excitation is roughly proportional to the number of excess neutrons, if the ground state of the target nucleus has valence nucleons only in the single j orbit outside a closed shell core.

C'. The magnitude of observed cross sections in GIAS-excitation is accounted for by the coherent sum of the DWBA and $(^3\text{He}-\alpha-t)$ amplitudes, if the Blatt-Jackson potential is used for the two-nucleon potential in the DWBA term.

D'. The energy dependence of the potential strength in DWBA is reduced by taking into account the two-step process. The cross section, however, is sensitive to the parameter of the optical potential and the value of D_0 . Experimental data on $^{90}\text{Zr}(^3\text{He}, ^3\text{He})^{90}\text{Zr}$, $^{90}\text{Zr}(t, t)^{90}\text{Zr}$, $^{90}\text{Zr}(\alpha, \alpha)^{90}\text{Zr}$ and $^{90}\text{Zr}(^3\text{He}, \alpha)^{89}\text{Zr}$ at each energy are not sufficient to decide the optical potentials and D_0 , making it difficult to draw definite conclusions.

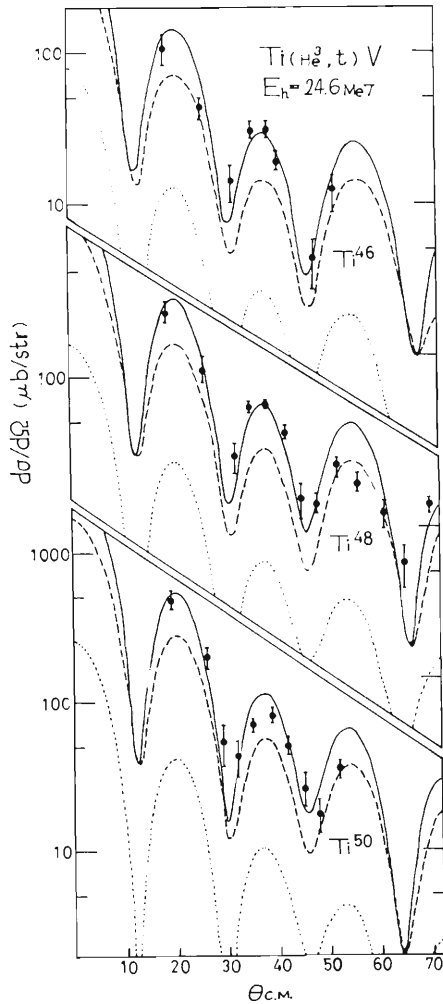


Fig. 3. Differential cross sections for the $^{46,48,50}\text{Ti}({}^3\text{He}, t){}^{46,48,50}\text{V}(\text{GIAS})$ reactions at $E_{3\text{He}} = 24.6$ MeV. For the symbols see Fig. 1.

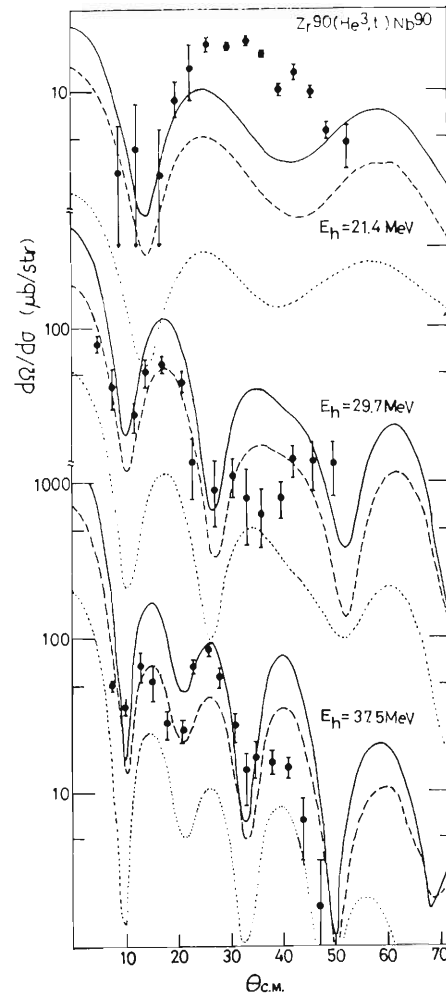


Fig. 4. Differential cross sections for the ${}^{90}\text{Zr}({}^3\text{He}, t){}^{90}\text{Nb}(\text{GIAS})$ reactions at $E_{3\text{He}} = 21.4$ MeV, 29.7 MeV and 37.5 MeV. For the symbols see Fig. 1.

References

- 1) G.R. Satchler, R.M. Drisko, and R.H. Bassel: Phys. Rev., 136, B637 (1964); P.D. Kunz, E. Rost, R.R. Johnson, G.D. Jones, and S.I. Hayakawa: *ibid.*, 185, 1528 (1969).
- 2) P. Kossani-Demay, P. Roussel, H. Faraggi, and R. Schaeffer: Nucl. Phys., A148, 181 (1970); R. Schaeffer: *ibid.*, A158, 321 (1970).
- 3) S.I. Hayakawa, W.L. Fadner, J.J. Kraushaar, and E. Rost: *ibid.*, A139, 465 (1969).
- 4) R. Hinriches, R. Sherr, G. Crawley, and I. Proctor: Phys. Rev. Letters, 25, 829 (1970).
- 5) W.L. Fadner, J.J. Kraushaar, and S.I. Hayakawa: Phys. Rev., C5, 859 (1972).
- 6) W.E. Frahn and G. Wiechers: Nucl. Phys., A113, 593 (1968).
- 7) M. Toyama and N. Onishi: Prog. Theor. Phys., 47, 460 (1971).

- 8) V.A. Madsen, M.J. Stomp, V.R. Brown, J.D. Anderson, Louisa Hansen, Calvin Wong, and J.J. Wesolowski: *Phys. Rev. Letters*, 28, 629 (1972)
- 9) M. Toyama: *Phys. Letters*, 38B, 147 (1972).
- 10) R. Schaeffer and G.F. Bertsch: *ibid.*, p. 159.
- 11) W.R. Coker, T. Udagawa, and H.H. Wolter: *ibid.*, 40B, 49 (1972).
- 12) W.L. Fadner, J.J. Kraushaar, and S.I. Hayakawa: *ibid.*, 40B, 49 (1972).
- 13) P.G. Roos, C.A. Ludemann, and J.J. Wesolowski: *ibid.*, 24B, 656 (1967).
- 14) R.C. Bearse, J.R. Comfort, J.P. Schiffer, M.M. Stautberg, and J.C. Stoltzfus: *Phys. Rev. Letters*, 23, 864 (1969).
- 15) J.M. Blatt and J.D. Jackson: *Phys. Rev.*, 76, 18 (1949); C.W. Wong and C.Y. Wong: *Nucl. Phys.*, A91, 433 (1967).
- 16) R. Stock, P. Bock, P. David, H.H. Duhm, and T. Tamura: *Nucl. Phys.*, A104, 136 (1967).

4-12. Coupling between Valence Nucleon and Clusterized Core

N. Takigawa

The structure of ${}^9\text{Be}$ is studied to clarify the situation of coupling between a valence nucleon and the clusterized core.¹⁾ We examine this problem on the basis of variational principle by taking a microscopic model. We assume such variational passes that allow the nucleus to have a cluster structure consisting of either a valence neutron coupled to a clusterized core, or α - and ${}^5\text{He}$ particles, and in an opposite limit of variation to have such structure that is suggested by the intermediate coupling shell model.²⁾

At the outset, we assume that the valence neutron is coupled strongly to the core; i.e. that the Hartree Fock field can be defined in the total system, because there appears experimentally a strong coupling type of ground state rotational band with negative parity. The following trial wave functions, which are based on the LCCO approximation, will be appropriate to represent such a picture of strong coupling:

$$|\phi_9^N\rangle_{\text{s.int.}} = \mathbf{a}^+ \pi_u (M_{\ell=1}) n \uparrow |\phi_8^M\rangle_{\text{int.}} \quad \text{and} \quad |\phi_9^P\rangle_{\text{s.int.}} = \mathbf{a}^+ \sigma_{g\bar{O},N}^+ (2) n \uparrow |\phi_8^M\rangle_{\text{int.}}$$

with

$$|\phi_8^M\rangle_{\text{int.}} = \mathbf{a}^+ \sigma_{gn}^+ \uparrow \mathbf{a}^+ \sigma_{gn}^+ \downarrow \mathbf{a}^+ \sigma_{gp}^+ \uparrow \mathbf{a}^+ \sigma_{gp}^+ \downarrow \mathbf{a}^+ \sigma_{in}^+ \uparrow \mathbf{a}^+ \sigma_{in}^+ \downarrow \mathbf{a}^+ \sigma_{up}^+ \uparrow \mathbf{a}^+ \sigma_{up}^+ \downarrow |0\rangle.$$

Each single particle wave function is assumed to be expressed as a linear combination of low-lying cluster orbitals around two cluster centers, which are denoted by parameters \mathbf{d}_1^C and \mathbf{d}_2^C , for example,

$$|\sigma_g^+\rangle = N \sigma_g^+ \left\{ \exp\left[-\frac{1}{2b^2}(\mathbf{r}-\mathbf{d}_1^C)^2\right] + \exp\left[-\frac{1}{2b^2}(\mathbf{r}-\mathbf{d}_2^C)^2\right] \right\}$$

$$|\pi_u(M_{\ell=1})\rangle = -\frac{1}{\sqrt{2}}(|\pi_{ux}\rangle + i|\pi_{uy}\rangle)$$

with

$$|\pi_{ux}\rangle = N \pi_{ux} \left\{ (x-d_{1x}^v) \exp\left[-\frac{1}{2b^2}(\mathbf{r}-\mathbf{d}_1^v)^2\right] + (x-d_{2x}^v) \exp\left[-\frac{1}{2b^2}(\mathbf{r}-\mathbf{d}_2^v)^2\right] \right\}.$$

It is assumed tentatively that $\mathbf{d}_1^C = \mathbf{d}_1^v = (0, 0, -d/2)$ and $\mathbf{d}_1^C + \mathbf{d}_2^C = 0$. The wave function $\sigma_{g\bar{O},N}^+ (2) \rangle$ is the second one with label σ_g^+ , and is orthogonalized to the first σ_g^+ representation.

$$|\sigma_{g\bar{O},N}^+ (2) \rangle = N \sigma_{g\bar{O},N}^+ (2) \{ |\sigma_g^+(2) \rangle - \lambda^+ |\sigma_g^+ \rangle \},$$

where

$$\lambda^+ = \langle \sigma_g^+ | \sigma_g^+(2) \rangle$$

with

$$|\sigma_g^+(2) \rangle = N \sigma_g^+(2) \left\{ (Z-d_{1z}^v) \exp\left[-\frac{1}{2b^2}(\mathbf{r}-\mathbf{d}_1^v)^2\right] - (Z-d_{2z}^v) \exp\left[-\frac{1}{2b^2}(\mathbf{r}-\mathbf{d}_2^v)^2\right] \right\}.$$

It can be shown easily that the wave functions $|\Phi_9^N\rangle$, $|\Phi_9^P\rangle$, and $|\Phi_8^M\rangle$ coincide, in the

limit of without clusterization (of d being zero), with the shell model states $(000)^4(001)^4 \frac{1}{\sqrt{2}} \{ (100)+i(010) \}$, $(000)^4(001)^4(002)$ and $(000)^4(001)^4$, labelled by the oscillator quanta in x, y , and z directions.

Our variational Hamiltonian is given by

$$H = \sum_i t_i - T_{c.m.} + \sum_{i < j} V_{ij},$$

where $T_{c.m.}$ is the operator of the center of mass motion. We assumed two types of effective interactions; Volkov force no.1 with Majorana strength $m=0.60$ and Hasegawa and Nagata force No. 1.³⁾ All of the qualitative results were found to be consistent in both cases, although some quantitative discrepancies were observed. The former interaction gives larger equilibrium values of b and d , but both interactions will give almost the same spectroscopic factor, because it is a function of the ratio d/b . The Volkov force gives ${}^9\text{Be}$ less binding energy than ${}^8\text{Be}$ mainly because it cannot give sufficient binding energy to odd system ${}^5\text{He}$.

Figure 1 shows the variational energy surfaces in these states as functions of parameter d . The figure includes, for comparison, the energy surfaces in the states

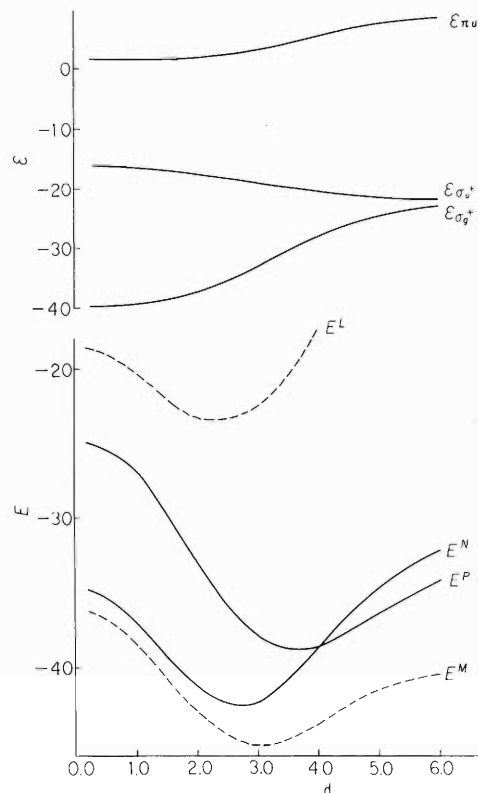


Fig. 1. Energy surfaces as functions of the degree of clusterization d . The parameter b was fixed to 1.5 fm, which gives the energy minimum for the state $|\Phi_9^N\rangle$. The index N denotes the curve is for the state $|\Phi_9^N\rangle$ and so forth. The energies were calculated by use of Volkov force no.2 with $m=0.60$. In the upper half, the single particle energy spectrum is shown as a function of d to show the effect of clusterization.

of ${}^8\text{Be}$ with maximal and lower spatial symmetries. The wave function of the latter is defined by

$$|\phi_8^L\rangle_{\text{int.}} = X^+([431]^{13}\pi)|\phi_8^M\rangle_{\text{int.}}$$

with

$$X^+([431]^{13}\pi) = \sum(s_\alpha s_\beta \tau_\alpha \tau_\beta) \mathbf{a} \pi_\nu (M_{\ell=1})_{s_\alpha \tau_\alpha} \tilde{\mathbf{a}} \sigma_\nu^+ s_\beta \tau_\beta \langle \frac{1}{2} \frac{1}{2} s_\alpha s_\beta | 1-1 \rangle \langle \frac{1}{2} \frac{1}{2} \tau_\alpha \tau_\beta | 00 \rangle.$$

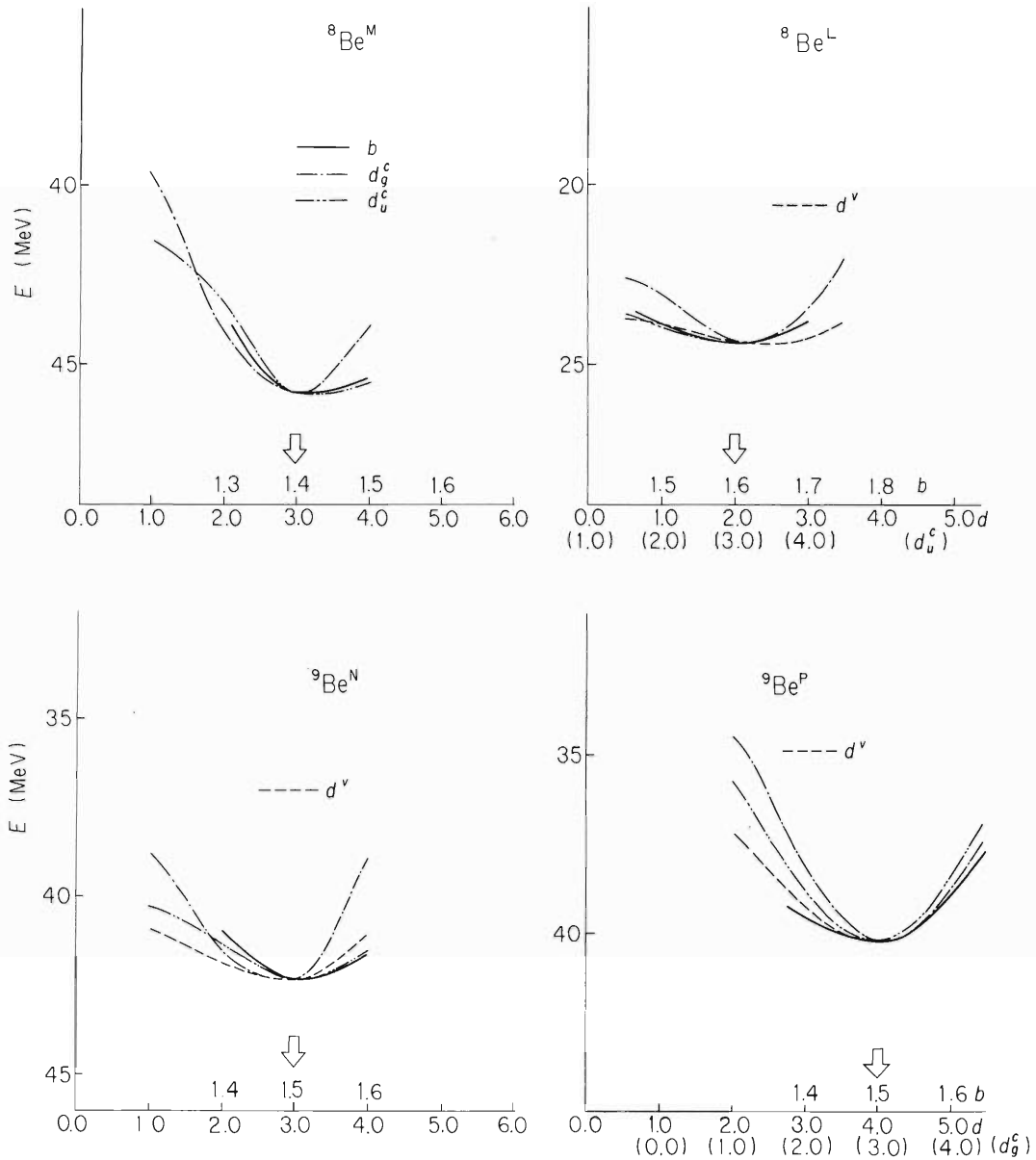


Fig. 2. Energy surfaces as functions of the parameters b and d . The solid line was obtained by varying b and choosing the other parameters so as to give the energy minimum. The other lines were obtained similarly. The arrow indicates the values of parameters, which give the lowest energy in each state.

We see that a large degree of clusterization in the state $|\Phi_8^M\rangle$ persists stably in the nucleus ${}^9\text{Be}$, although some change of it (somewhat reduction in the negative parity state) is caused by adding a valence neutron. This is contrary to the situation in the state $|\Phi_8^I\rangle$, where clusterization is much reduced (b becomes larger and d becomes smaller) by an additional valence nucleon and a hole in the core.

This finite degree of clusterization in the nucleus ${}^9\text{Be}$ will explain the energy gap between two peaks observed in the $(p,2p)$ reaction,⁴⁾ which becomes smaller in this nucleus in comparison with the general trend in the surrounding nuclei, because the inverse of this gap is proportional to the time during which a nucleon is trapped by a definite side or cluster of the total system. This proximity in energy of two single particle levels is mainly caused by missing of gap in kinetic energy in these states due to large clusterization. Similar effect through the kinetic energy appears in proximity of total energies of states with negative and positive parity. We may have a better variational wave function by varying independently the parameter d in each single particle orbit. Figure 2 shows such energy surfaces that are obtained by varying a parameter, say b , and by taking values of all the other parameters so as to give the lowest energy at each value of b . We see there quantitative refinement, but no qualitative change.

We can take another type of variational wave function if we allow the parameter d^V in the wave function of valence nucleon to have a different value from that of clustering parameter of the core d^C ,

$$|\phi_9^P\rangle_{S'.\text{Int.}} = \mathbf{a}^+ \sigma_{\bar{0},N}^+(2') n \uparrow |\phi_8^M\rangle_{\text{Int.}},$$

where the single particle wave function is defined by

$$|\sigma_{\bar{0},N}^+(2')\rangle = N \sigma_{\bar{0},N}^+(2') \{ |\sigma_{\bar{0}}^+(2')\rangle - \langle \sigma_{\bar{0}}^+(2') | \sigma_{\bar{0}}^+ \rangle | \sigma_{\bar{0}}^+ \rangle \}$$

with

$$|\sigma_{\bar{0}}^+(2')\rangle = N \sigma_{\bar{0}}^+ \left\{ \exp\left[-\frac{1}{2b^2}(\mathbf{r}-\mathbf{d}_1^v)^2\right] + \exp\left[-\frac{1}{2b^2}(\mathbf{r}-\mathbf{d}_2^v)^2\right] \right\}, \quad (\{\mathbf{d}^v\} \neq \{\mathbf{d}^c\}).$$

Our new trial wave function $|\Phi_9^P\rangle_{S'.\text{Int}}$ coincides with the previous one $|\Phi_9^P\rangle_{S.\text{Int}}$ in the limit of $\mathbf{d}^C = \mathbf{d}^V$. But this choice will become more suitable if the coupling between the valence neutron and the clusterized core is weak and they move almost independently with each other. This wave function represents a separated system composed of ${}^8\text{Be}$ and a nucleon in the case when d^V is infinite and d^C is finite. Figure 3 shows the variational energy surfaces in these states as functions of the parameter d . We have somewhat larger variational energy by taking the wave function $|\Phi_9^P\rangle_{S'.\text{Int}}$. This may suggest that the valence nucleon is coupled relatively weakly to the ${}^8\text{Be}$ core in the positive parity state. We have equilibrium minimum in all variational surfaces at large d , which seems to support the experimental information, which is positive as for the existence of the low-lying anomalous parity state.

We assumed in the preceding paragraphs that the valence neutron is coupled strongly to the core independently of its parity. Especially, we have assumed that the clusterization parameter \mathbf{d}^V in the wave function of valence nucleon is parallel to \mathbf{d}^C , which specifies the direction of the core. It should be noticed, however, that experimentally there has been found a clear rotational band of strong coupling type only for the case of negative parity. In explaining the missing of rotational band with positive parity we adopt a weak coupling picture⁵⁾ to the positive parity states (see Fig. 4), although we may attribute the missing to large effect of decoupling because of its K value, $K = 1/2$, if we stick to our previous picture of strong coupling.⁶⁾

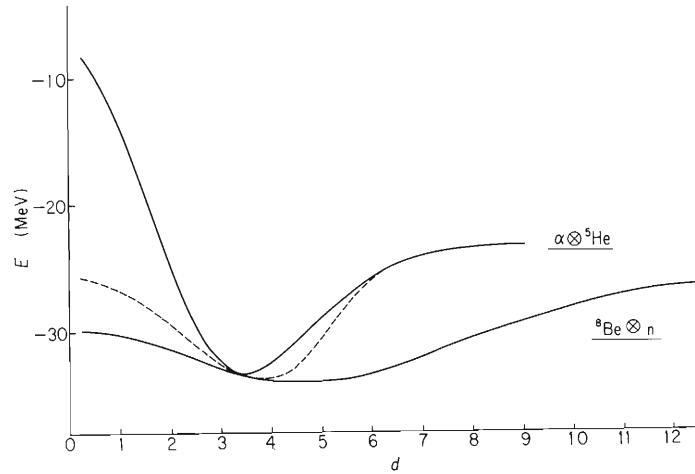


Fig. 3. Energy surfaces as functions of the parameter d . The size parameter b was fixed to 1.31 fm, and the energies were calculated by use of Volkov force no.1 with $m=0.60$. The upper solid curve is obtained for the wave function $|\Phi_9^P\rangle_{S.Int.}$ by varying the parameter d with restriction of $d^C=d^V=d$. The dashed curve and the lower solid curve are obtained for the same wave function and for the wave function $|\Phi_9^P\rangle_{S'.Int.}$ respectively, but by taking the best value of the parameter d^C at each value of the parameter d^V , which becomes to be about 3.0 fm in almost all cases. This value corresponds to that value for the free ${}^8\text{Be}$ system.

We have examined the situation in which the valence nucleon feels the orientation of the core by rotating only the valence nucleon relatively to the core. The expectation value of Hamiltonian are shown in Table 1 as a function of the rotation angle θ . We see a large energy gap between the cases of $\theta=0$ and $\theta=\pi/2$ only in the state of negative parity. The valence nucleon seems, on the other hand, to take all values of θ with relatively small energy change in its positive parity state. This difference between opposite parity states is caused mainly by the Pauli principle. The situation may be understood if we consider the case near the limit of shell model. The negative parity single particle wave function of valence nucleon becomes a combination of shell model configurations mainly with $3\hbar\omega$ or larger quanta in the case when θ is $\pi/2$ instead of $1\hbar\omega$ configurations in the case when θ is zero, because lower configurations are already occupied by particles in the core. The single particle wave function, on the other hand, is mainly $2\hbar\omega$ configuration independently of θ in the positive parity state.

Our interest, thus, lies in the examination if we have a lower variational energy by making the wave function of the valence nucleon have a good angular momentum by itself in the case of positive parity. This situation is very different from that for the ground state with negative parity, where only its z -component is a good quantum number. The wave function thus obtained may be called a weak coupling "intrinsic" state. A result is given in Table 2 by assuming the following approximate wave function;

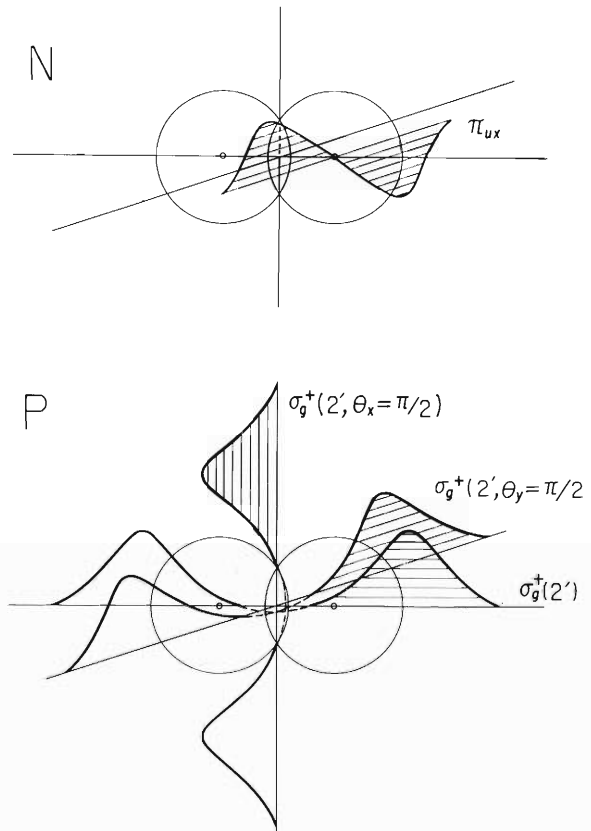


Fig. 4. Angular momentum projection scheme in the total system. The figure indicates that in the anomalous parity state, the valence nucleon may have a good angular momentum by itself, which is then coupled to that of the latter to form the final angular momentum.

The quantities $E_{//}$, E_{\perp} and E_w are the expectation values of Hamiltonian in the states

$$\mathbf{a}_{\bar{O}.N.}^+(\sigma_g^+(2', \theta=0))|\Phi_8^M\rangle, \mathbf{a}_{\bar{O}.N.}^+(\sigma_g^+(2', \theta_y=\pi/2))|\Phi_8^M\rangle \text{ and } |\Phi_9^P\rangle_{w.int.}$$

respectively. This table shows that the weak coupling "intrinsic" state gives almost the same binding energy as that of strong coupling one. This may suggest that the strong coupling intrinsic state is not so stable in the case of anomalous parity. This tendency of preference for a weak coupling type of angular momentum projection in anomalous parity state may occur more distinctly in the system, where there are alpha-like valence nucleons' group because of their gain in the intrinsic correlation energy in addition to the kinematical effect mentioned above.⁷⁾

Table 1. Energy changes as functions of the parameter θ . The table shows that the valence nucleon feels the orientation of the core strongly only in the negative parity state.

$b = 1.6$			N			P			
d_g^c	d_u^c	d^v	0°	45°	90°	0°	45°	90°	
0.2	0.2	0.2	T	137.6	137.6	151.1	145.7	144.8	143.9
			V	-176.4	-176.4	-132.7	-175.4	-172.1	-168.9
			E	-38.74	-38.73	18.50	-29.60	-27.27	-24.93
			ΔE		0.01	57.24		2.33	4.67
3.0	3.0	3.0	T	115.4	115.6	127.7			
			V	-159.2	-155.7	-151.3			
			E	-43.79	-40.20	-23.54	-39.37	-36.62	-32.92
			ΔE		3.59	20.25		2.75	6.45
3.0	4.0	4.0	T				112.4	111.3	109.9
			V				-153.3	-148.2	-142.8
			E				-40.96	-36.92	-32.78
			ΔE					4.04	8.18
0.2	0.2	0.6	T	136.3		142.1			
			V	-166.2		-161.8			
			E	-29.84		-19.77	-22.34		-20.80
			ΔE			10.07			1.54

Table 2. Comparison between intrinsic energies in the states with strong and weak coupling scheme of angular momentum projection.

d^v	d^c	E	E	EW
0.2	3.5	-30.08	-30.08	-30.08
4.0	3.5	-33.83	-26.34	-32.83
9.0	3.0	-29.14	-26.58	-28.02

References:

- 1) K. Ikeda et al.: Progr. Theor. Phys. Suppl. (1972) to be published;
A. Arima et al.: Advances Nucl. Phys., 5 to be published.
- 2) F.C. Barker: Nucl. Phys., 83, 418 (1966).
- 3) A.B. Volkov: *ibid.*, 74, 33 (1965);
A. Hasegawa and S. Nagata: Progr. Theor. Phys., 45, 1786 (1971).
- 4) G. Jacob and Th. A.G. Maris: Rev. Mod. Phys., 38, 121 (1966).
- 5) T. Sebe: Progr. Theor. Phys., 30, 290 (1963);
D. Kurath and R.D. Lawson: Nucl. Phys., 23, 5 (1961).
- 6) F.S. Stephens, R.M. Diamond, J.R. Leigh, T. Kammuri, and K. Nakai: Phys. Rev. Lett. 29, 438 (1972)
- 7) N. Takigawa and A. Arima: Nucl. Phys., 168, 593 (1971);
Y. Suzuki, H. Horiuchi and K. Ikeda: Progr. Theor. Phys., 47, 1517 (1972);
F. Nemoto and K. Bando: *ibid.*, p. 1210.

5. NUCLEAR PHYSICS

Nuclear Spectroscopy

5-1. The Gamma-Decay of $^{146, 150, 152}\text{Sm}$ following the $(\alpha, 2n)$ Reaction

A. Hashizume, Y. Tendow, T. Katou,
and H. Kumagai

The energies of the lowest excited states of even-even nuclei with angular momentum of 2^+ , 4^+ , 6^+ and 8^+ etc. change suddenly from ^{146}Sm to ^{152}Sm , because these nuclei lie across the spherical to permanent deformed regions. The excited energies of these so-called quasi-rotational bands up to the 8^+ or 10^+ states were established and reported previously.^{1),2)} Our concern is related to the relative transition intensities in these ground state bands as the last process of de-excitation of the compound nuclei. These nuclei formed by bombarding with alpha-particles have rather large angular momentum which should be dissipated with evaporation of particles or emitting γ -rays until they decay to the ground state. This large loss of angular momentum of nuclei could not be explained by the conventional statistical theory.

The enriched targets $^{144, 148, 150}\text{Nd}$ were bombarded with alpha-particles of 18 MeV to 45 MeV in 2.5 MeV steps and γ -rays were observed with a Ge(Li) detector. Figure 1 shows energy levels of ground state bands in $^{146, 150, 152}\text{Sm}$ which are in good agreement with the results in Ref. 2). The transitions in the ground state band were considered to be pure E2 and the intensities of electrons in the transitions were estimated from the table of the conversion coefficients by Hager and Seltzer. The relative transition intensities ($I_\gamma + I_e$) of $4^+ \rightarrow 2^+$, $6^+ \rightarrow 4^+$ etc. to $2^+ \rightarrow 0^+$ transition in the $(\alpha, 2n)$ reaction are plotted in Fig. 2 (a), (b), and (c) as a function of bombarding

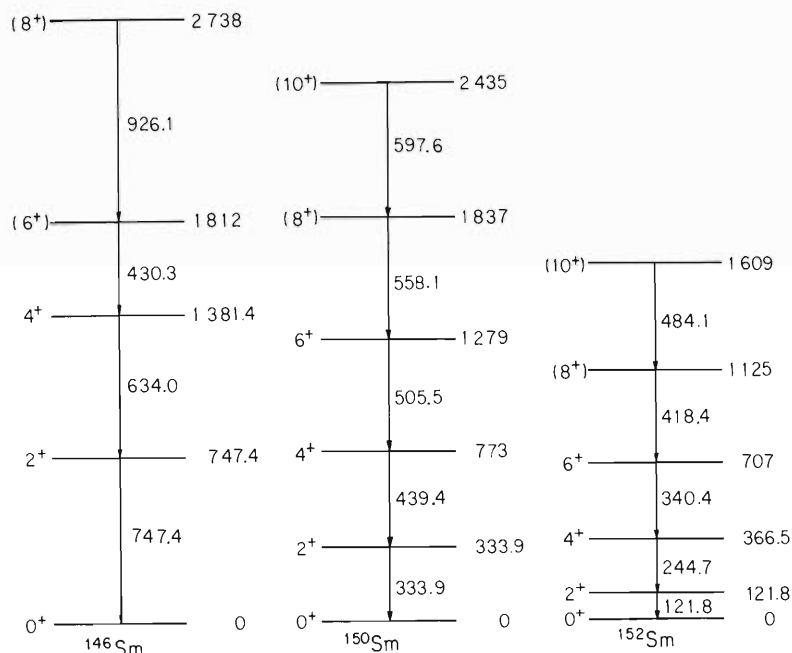


Fig. 1. Energy levels of ground state bands in $^{146, 150, 152}\text{Sm}$ nuclei.

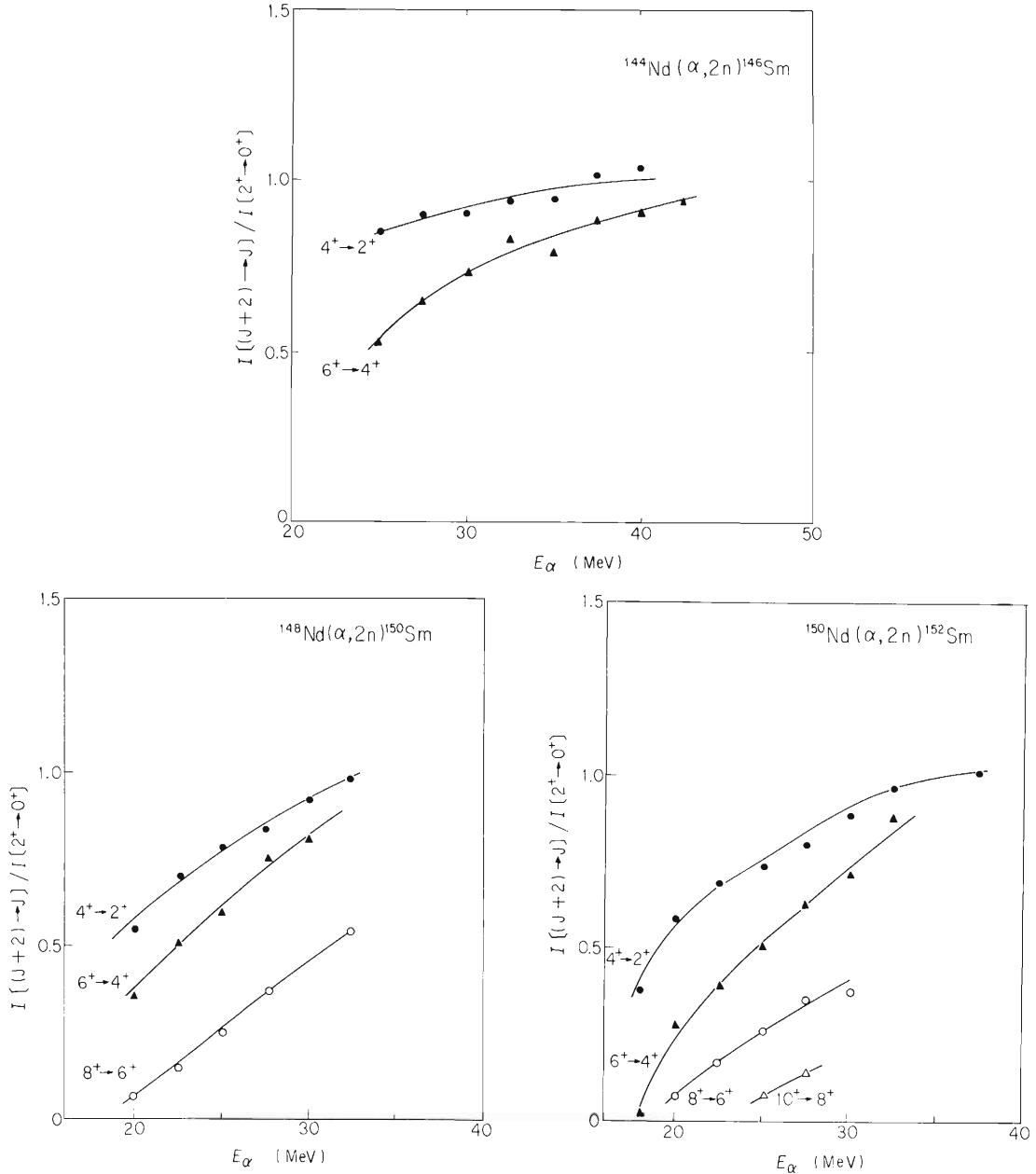


Fig. 2. (a) Transition intensity ratios of $(J+2) \rightarrow J$ to $2^+ \rightarrow 0^+$ in ^{146}Sm were plotted as a function of bombarding energy of alpha-particles. (b) The same as in Fig. 2(a) for ^{150}Sm , (c) The same as in Fig. 2(a) for ^{152}Sm .

energy. From Fig. 2 it is seen that the change of the relative intensities in terms of the bombarding energies in ^{150}Sm and ^{152}Sm is nearly the same in spite of the difference of the excited energies of the ground state bands. However, the change is slow in ^{146}Sm as shown in Fig. 2 (a). Rough estimate of the angular momentum introduced in compound nuclei by classical model gives a value of about 8 (in units of \hbar) for $E_\alpha = 25$ MeV and 11 for $E_\alpha = 30$ MeV. And the nucleus does not essentially change the angular momentum distribution by neutron evaporation. The difference in relative intensities of γ -rays between ^{146}Sm and ^{150}Sm or ^{152}Sm can be attributed to the difference of angular momenta introduced in the compound nuclei. When the samarium nuclei get to have rotational structure, the curve of the excitation energies of

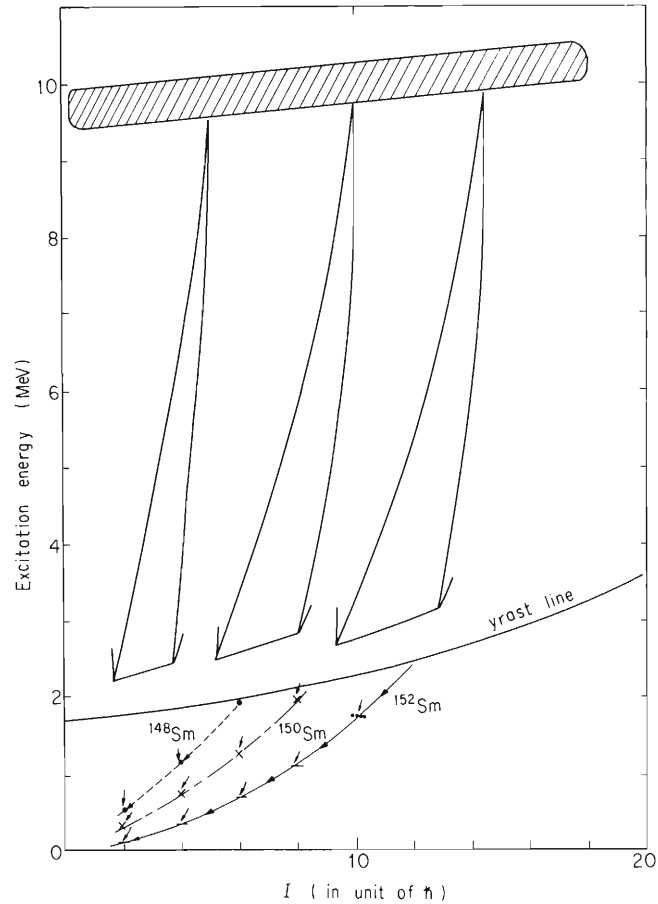


Fig. 3. Schematical representation of the last process of de-excitation of compound nuclei.

the ground state band as a function of angular momentum rises more slowly compared with the ^{146}Sm , showing that there are more side feeding γ -rays in ^{152}Sm when the bombarding energy of alpha-particles is low. These circumstances are shown schematically in Fig. 3. In case of ^{152}Sm , the K-selection rule may play a role, but a more precise examination is required to confirm this effect.

The intensity ratios between the ground state band transition and the side feeding γ -rays depend on three processes: 1) energy and especially angular momentum distributions of compound states, 2) evaporation of neutrons, and 3) cascade γ -rays as the last step to reach the ground state band. The first two problems were recently treated statistically by Jägare³⁾ and Ejiri,⁴⁾ and there are many experimental studies^{5)~7)} in the rotational region by exciting the nucleus with alpha-particles. In comparison with the statistical model, the population of the high spin states in the ground state band is small and deviates from the theoretical estimate. Some stress was pronounced on the γ -ray decay near the yrast-level by Ferguson et al.⁸⁾ Further experimental analysis and theoretical studies are in progress.

References

- 1) H. Morinaga: Nucl. Phys., 75, 385 (1966).
- 2) I. Adam, L-E Fröberg, J. Kownacki, H. Ryde, and Z. Sujkowski: Annual Rep. of Res. Inst. Phys., Sweden, P.36 (1970).
- 3) S. Jägare: Nucl. Phys., A95, 481 (1967).
- 4) H. Ejiri: Bull. Am. Soc., 13, 700 (1968).
- 5) C. D. Kavaloski, W. J. Kossler, and C. F. Williamson: Nucl. Phys., A124, 401 (1969).
- 6) A. S. M. De Jesus, S. J. Mills, and W. L. Rautenbach: *ibid.*, A172, 323 (1971).
- 7) A. Johnson, H. Ryde, and J. Sztarkier: Phys. Letters, 34B, 605 (1971).
- 8) S. M. Ferguson, H. Ejiri, and I. Halpern: Nucl. Phys., A188, 1 (1972).

5-2. Decay of ^{87}Zr and ^{85}Zr (II)

T. Katou, Y. Awaya, Y. Tendow,
A. Hashizume, and T. Hamada

The results of gamma-ray studies on the decay of ^{87}Zr and ^{85}Zr were reported previously,¹⁾ in which the γ - γ coincidence measurements of ^{87}Zr by using a Ge(Li) detector and a NaI(Tl) detector were described along with the energies and relative intensities of the gamma-rays. The information obtained by previous γ - γ coincidence works, however, was not so clear-cut because there were many gamma-rays which could not be resolved by the NaI(Tl) detector.

Table 1. Result of the γ - γ coincidence for ^{87}Zr .

Gate E γ	511	772	794(+797)	1024	1159	1203	1210	1227
611							+	
633								
772					+			
794								
797				+				
973							+	
1024			(+)		+			
1048								+
1159		+		+				
1203								+
1210								
1227	+					(+)		
1388								+
1410		+	+	+				
1657				+				
1808			+					

(+) means that coincidence of these gamma rays is not very certain.

In this paper, the γ - γ coincidence measurements were made for ^{87}Zr and ^{85}Zr by using a 23 cm^3 Ge(Li) detector and a 29 cm^3 Ge(Li) detector. In the study of coincidence between annihilation gamma-rays and others, the triple coincidence technique using the 23 cm^3 Ge(Li) detector and two 7.6 cm in height and 7.6 cm in diameter NaI(Tl) detectors were employed to reduce accidental events. The block diagrams of the coincidence circuits are shown in Fig. 1. The results of measurements are shown in Tables 1 and 2. Because of poor statistics, ambiguities are left in some cases and only definite results are given in these tables. The present results on ^{87}Zr show that there are few misassigned transitions in the previously proposed decay scheme and a revised one is under construction.

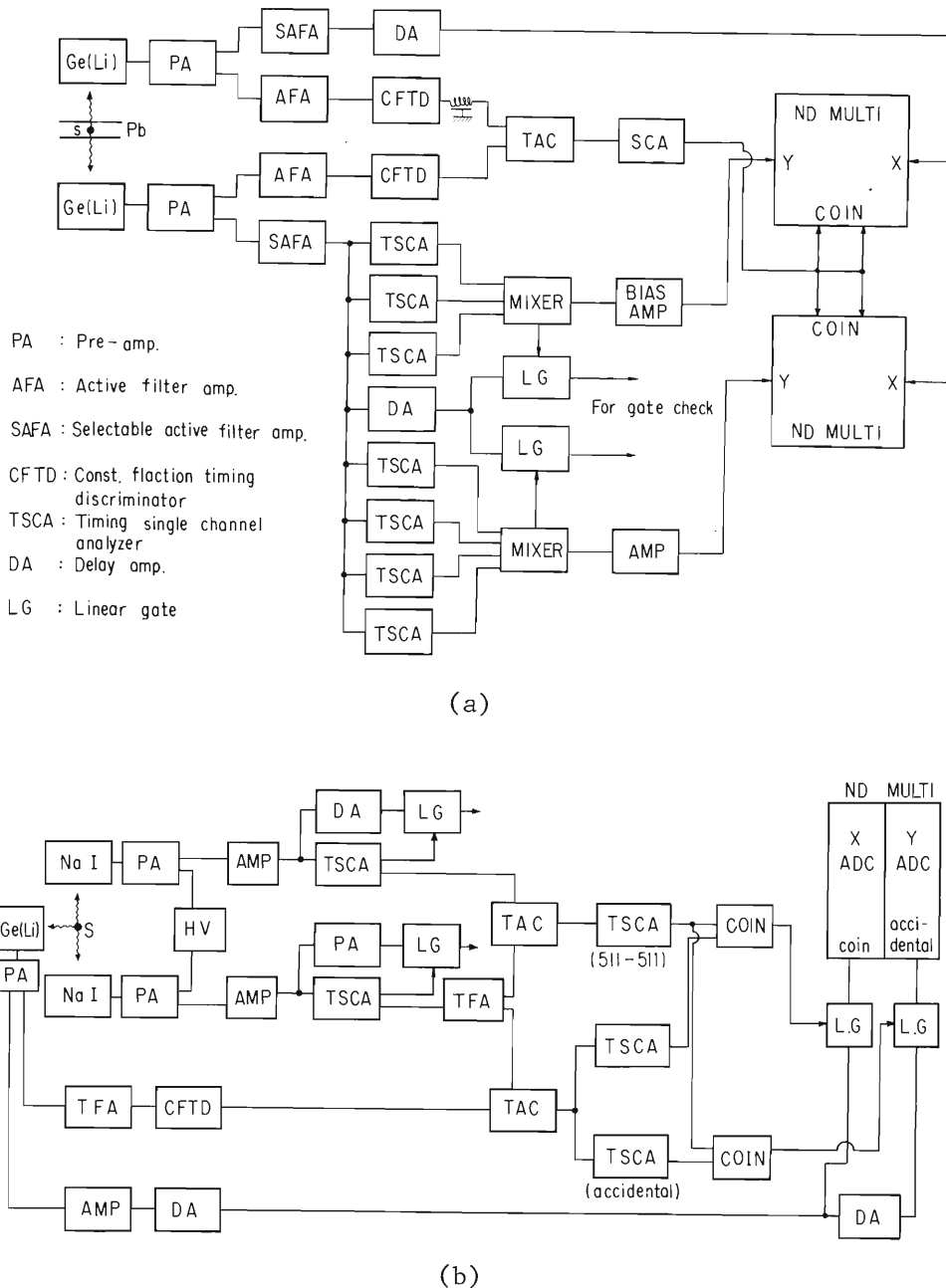


Fig. 1. Block diagrams of γ - γ coincidence systems, a) is used for the coincidence measurement using a 23 cm^3 Ge(Li) detector and a 29 cm^3 Ge(Li) detector, and b) is used for the triple coincidence measurement.

Table 2. Result of the γ - γ coincidence for ^{85}Zr .

E_{γ} \ Gate	265.4	415.1	453.1	511	E_{γ} \ Gate	265.4	415.1	453.1	511
265.4					1171.1				
356.8		+			1191.1		+		
415.1				+	1198.5				
453.1				+	1410.5		+		
621.5					1729.5			+	
635.4					1767.4	(+)	+		
781.3		+			1875.1			+	
799.2			+		1936.8	(+)	+	+	
910.4					1954.1				
964.7					2143.0				
1159.9			+		2387.7				

Reference

- 1) Y. Awaya, T. Katou, Y. Tendow, A. Hashizume, and T. Hamada: IPCR Cyclotron Progr. Rep., 5, 57 (1971).

5-3. Magnetic Moments of High-Spin Isomeric States in Po Isotopes

Y. Yamazaki, O. Hashimoto, S. Nagamiya,
T. Nomura, K. Nakai, and T. Yamazaki

The g -factors of the 8^+ state of ^{204}Po and of the 13^- state¹⁾ of ^{210}Po have been determined, and the g -factors of the 8^+ states of $^{210}, ^{208}, ^{206}\text{Po}$ and of the $17/2^-$ state of ^{209}Po have been remeasured.^{2)~4)} These isomeric states were populated via (particle, xn) reactions with the beams from the cyclotron. Targets and reactions used here are listed in Table 1. Gamma-rays following the (particle, xn) reactions were detected by two NaI(Tl) counters placed at angles 60° and 135° except for the case of ^{204}Po in which a Ge(Li) detector was used. The stroboscopic resonance method⁵⁾ was used for the 8^+ states of $^{210}, ^{208}, ^{206}, ^{204}\text{Po}$ and the $17/2^-$ state of ^{209}Po , and the time-differential spin-rotation method for the 13^- state of ^{210}Po . In the stroboscopic resonance method a magnetic field applied perpendicularly to the beam-detector plane was automatically swept near the resonance field calculated from the expected g -factor of each state and the interval between the natural cyclotron beam bursts. In case of the

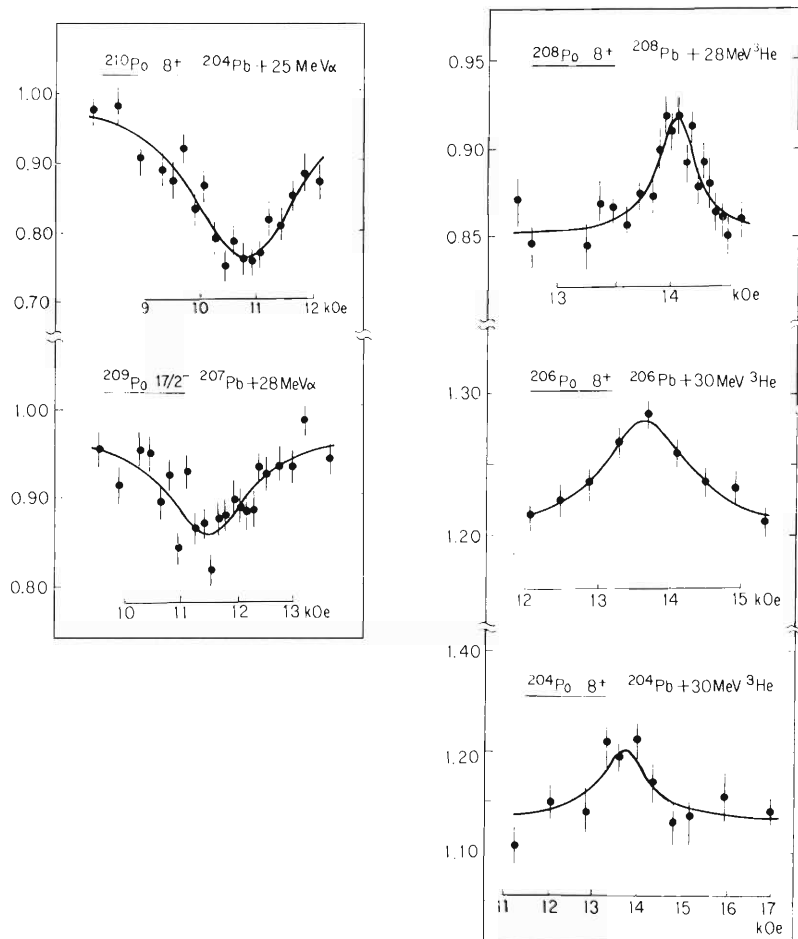


Fig. 1. Stroboscopic resonances for the 8^+ states of $^{210}, ^{208}, ^{206}, ^{204}\text{Po}$ and the $17/2^-$ states of ^{209}Po .

Table 1. Reactions to populate the states whose g factors were measured.

	J^π	Particle	Reaction	Energy (MeV)
^{210}Po	8^+	α	$^{208}\text{Pb}(\alpha, 2n)$	25
^{209}Po	$17/2^-$	α	$^{207}\text{Pb}(\alpha, 2n)$	28
^{208}Po	8^+	^3He	$^{208}\text{Pb}(^3\text{He}, 3n)$	28
^{206}Po	8^+	^3He	$^{206}\text{Pb}(^3\text{He}, 3n)$	30
^{204}Po	8^+	^3He	$^{204}\text{Pb}(^3\text{He}, 3n)$	30
^{210}Po	8^+	α	$^{208}\text{Pb}(\alpha, 2n)$	33

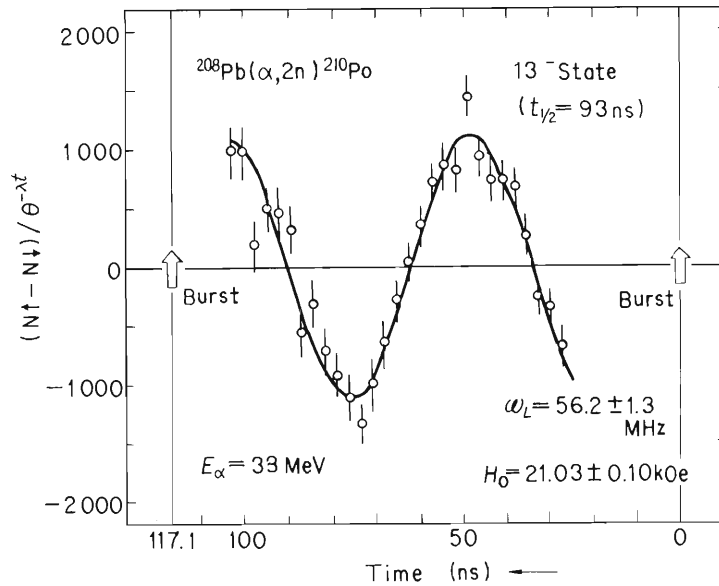


Fig. 2. Time-differential pattern for the 13^- state of ^{210}Po .

time-differential spin-rotation method used for the 13^- state of ^{210}Po , a magnetic field of 21.03 ± 0.10 kOe was applied up and down perpendicularly to the beam-detector plane, and the time calibration was performed by observing two prompt peaks in the time spectrum. Figures 1 and 2 show the experimental results. The g-factors obtained are listed in Table 2 together with the calculated g-factors deduced from the known g-factors of single particle states by use of the additivity relation.

The experimental g-factors agree with the calculated values. This fact suggests that the main configurations of all the 8^+ states are $(\pi h_{9/2}^2)8^{+.6), 7)$. It is somewhat remarkable that the 8^+ states of $^{206}, ^{204}\text{Po}$, which are far from the single closed shell, have rather pure configurations. Furthermore, the additivity relation of the g-factor holds well even for the core excited state such as the 13^- state of ^{210}Po , supporting the assignment of Blomqvist et al.¹⁾ that the 13^- state of ^{210}Po arises from $(\pi h_{9/2}^2)8^+$ coupled to the 5^- state of the ^{208}Pb core. The reason why all of these states have such pure configurations may be ascribed to the fact that these states have high spins.

Table 2. The experimental g-factors together with the expected main configurations of the states and the calculated g-factors.

	J^π	$T_{1/2}$ (ns)	Configuration	g_{exp}	g_{cal}^*
^{210}Po	8^+	110	$\pi h_{9/2}^2$	0.901 ± 0.013	0.910
^{209}Po	$17/2^-$	100	$\pi h_{9/2}^2 \nu p_{1/2}^{-1}$	0.897 ± 0.015	0.926
^{208}Po	8^+	380	$\pi h_{9/2}^2 (\nu p_{1/2}^{-2}) 0^+$	0.911 ± 0.010	0.910
^{206}Po	8^+	212	$\pi h_{9/2}^2 (\nu p_{1/2}^{-2} \nu f_{5/2}^{-2}) 0^+$	0.905 ± 0.018	0.910
^{204}Po	8^+	140	$\pi h_{9/2}^2 (\nu p_{1/2}^{-2} \nu f_{5/2}^{-2}) 0^+$	0.905 ± 0.040	0.910
^{210}Po	13^-	93	$(\pi h_{9/2}^2) 8^+ \otimes 5^- (^{208}\text{Pb})$	0.546 ± 0.012	0.563

* Deduced from the known g factors by use of the additivity relation of the g factor.

The decrement of $g(^{210}\text{Po}, 8^+)$ from $g(^{209}\text{Bi}, 9/2^-)$ may be due to the blocking effect on the $(\pi h_{9/2}^2 h_{11/2}^{-1}) 1^+$ type core polarization.⁸⁾ The increment of $g(^{208}\text{Po}, 8^+)$ from $g(^{210}\text{Po}, 8^+)$ may be due to the $(\nu p_{3/2}^{-1} p_{1/2}) 1^+$ type core polarization.⁸⁾ A mixture of the $(8^+ \times \nu p_{3/2}^{-1}) 17/2^-$ configuration decreases the value of $g(^{209}\text{Po}, 17/2^-)$, and so this small mixture is expected from the small difference between g_{exp} and g_{cal} of the $17/2^-$ state of ^{210}Po .

References

- 1) J. Blomqvist, D. Fant, K. Wikstrom, and I. Bergstrom: *Physica Scripta*, 3, 9 (1971).
- 2) T. Yamazaki, T. Nomura, T. Katou, T. Inamura, A. Hashizume, and T. Tendow: *Phys. Rev. Letters*, 24, 317 (1970).
- 3) T. Yamazaki, T. Nomura, S. Nagamiya, and T. Katou: *ibid.*, 25, 547 (1970).
- 4) S. Nagamiya, T. Nomura, and T. Yamazaki: *Nucl. Phys.*, A159, 653 (1970).
- 5) J. Christiansen, H.E. Mahnke, E. Recknagel, D. Riegel, G. Weyer, and W. Witthuhn: *Phys. Rev. Letters*, 21, 554 (1968); S. Nagamiya and K. Sugimoto: Osaka University Report, OULNS, 69-3 (1969).
- 6) T. Yamazaki: *Phys. Rev.*, C1, 290 (1970).
- 7) S. Nagamiya and T. Inamura: *Nucl. Phys.*, A182, 84 (1972).
- 8) A. Arima and H. Horie: *Progr. Theor. Phys.*, 12, 623 (1954).

5-4. A Method of Measuring Alpha-Decays in the Nanosecond Range

T. Nomura, K. Hiruta, T. Inamura, and M. Odera

Many neutron-deficient elements beyond lead are known to be high-energy α - emitters with short half-lives. In particular the nuclides with 128 neutrons are expected to have the largest α -decay energies due to the extra stability of the N=126 neutron shell, and lifetimes of these nuclei will fall in the submicrosecond region. It is almost impossible to measure such short lifetimes by the usual "off-beam" preparation of α -activities. Even the rapid helium -jet collection system needs much longer transportation time (usually longer than 1 ms) and thus, measurements of lifetimes shorter than microseconds have been limited to cases where activities of interest are provided from the decay of parent nuclei having sufficiently long half-lives. We have therefore developed a simple pulsed-beam method of observing α -decays with lifetimes ranging from microseconds to a few nanoseconds.

The principle of the present method is to produce α -emitters by nuclear reactions, to stop them within a target used and to observe α -decays between natural beam bunches of the cyclotron with the help of the fast electronics. This method is essentially the same as the one employed by Yamazaki and Ewan¹⁾ in the study of gamma decays from nanosecond isomers. The beam spread of the cyclotron is around 2ns and its repetition period ranges from 80 to 150 ns depending on accelerated particles and their energies. Alpha -particles were detected with a Si-detector of surface barrier type placed at 135 degrees to avoid strong Coulomb scattering of incident particles. The depletion layer of the detector was about 200 μ m and the measurable maximum energies were around 0.2 MeV, 5 MeV and 20 MeV for electrons, protons and α -particles, respectively. This property of the thin Si-detector is very convenient since we are interested in short-lived α -decays having high decay-energies,

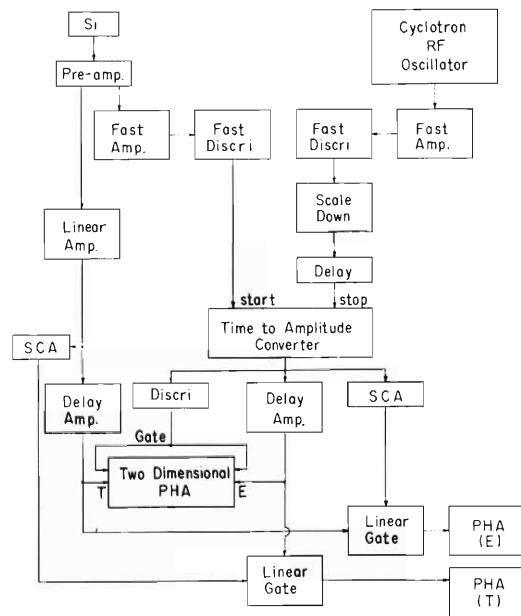


Fig. 1. The schematic diagram of the present electronics.

say, from 5 MeV to 15 MeV. Although no special particle-identification technique was used, the above property of the detector and the electrical system of taking delayed particles turned out to be enough to discriminate delayed α -particles from prompt emission of other charged particles following reactions and also from possible delayed emission of protons and fission fragments.

The electronics used is shown in Fig. 1. In order to check the timing property of this system, the prompt emission of charged particles such as protons and alphas having energies between 5 MeV and 15 MeV in the $^{32}\text{S} + ^{12}\text{C}$ (81 MeV) reaction was detected by the same system. The time resolution obtained was around 2 ns, being almost the same as the spread of the beam burst.

Figure 2 shows a typical time distribution of charged-particle emission following bombardment of a ^{208}Pb target of about 1 mg/cm^2 thickness with 91 MeV ^{14}N -beam. In this case a time resolution of the prompt curve was 5.6 ns, being considerably broader than the one mentioned above. This can be explained by the fact that there are three gross groups in velocity distributions of charged particles which cause the prompt part of the time spectrum; light particles such as protons and alphas, scattered incident heavy ions, and fission fragments.

Typical energy spectra in various sections of the delay time taken by using a two-dimensional PHA are presented in Fig. 3. They were observed when a 1.5 mg/cm^2 ^{207}Pb target was bombarded with 81 MeV ^{14}N -ions. The spectrum shown at the top of the left side of this figure includes the prompt component and therefore has appreciable backgrounds with continuous energy distributions, while almost no backgrounds exist in the delayed spectra in the energy range from 5 MeV to 15 MeV. Two prominent peaks at 9.65 MeV and 6.77 MeV were due to decays of a previously unknown element ^{217}Ac

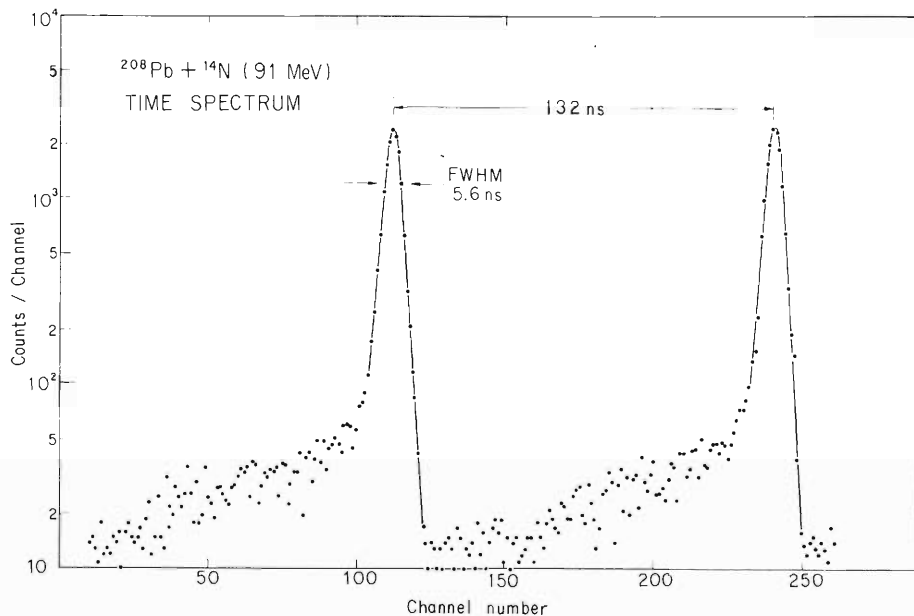


Fig. 2. A typical time distribution of charged particles taken by the electronics system shown in Fig. 1. Every second pulse from the cyclotron oscillator generates the stop signal of the time-to-amplitude converter, and therefore two prompt peaks appear in the time spectrum.

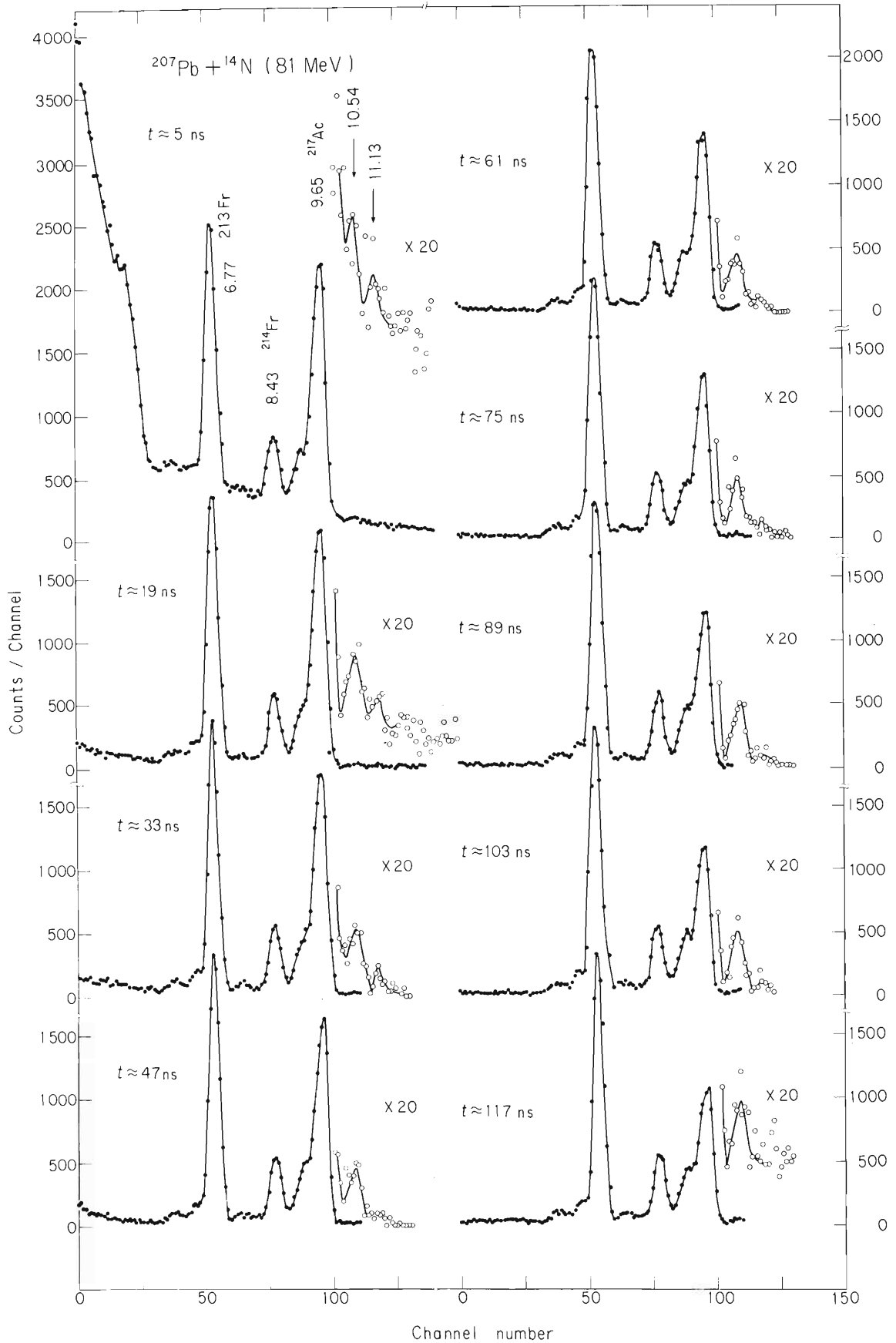


Fig. 3. A part of two-dimensional spectra – 256 channels (energy) times 16 channels (time) – resulting from bombardment of a ^{207}Pb target with 81 MeV ^{14}N -ions.

produced in the $^{207}\text{Pb}(^{14}\text{N},4\text{n})$ reaction and its daughter nucleus ^{213}Fr , respectively.²⁾ The 9.65 MeV peak was found to decay with a half-life of $0.10 \pm 0.01 \mu\text{s}$, while the other peaks having energies lower than 9 MeV turned out to be constant in this time range. Two small peaks at 10.54 MeV and 11.13 MeV were found to have similar excitation functions to that of the 9.65 MeV peak and therefore assigned to the decay from isomeric states of ^{217}Ac . Their half-lives are $400 \pm 100 \text{ ns}$ (10.54 MeV) and $8 \pm 2 \text{ ns}$ (11.13 MeV).

References

- 1) T. Yamazaki and G.T. Ewan: *Phys. Letters*, 24B, 278 (1967).
- 2) T. Nomura, K. Hiruta, T. Inamura, and M. Odera: *ibid.*, 40B, 543 (1972).

5-5. Alpha- and Gamma-Spectroscopy of N=128 Isotones

 ^{216}Ra , ^{217}Ac , and ^{218}Th T. Nomura, K. Hiruta, T. Inamura,
M. Odera, and O. Hashimoto

Alpha-decays from N=128 isotones, ^{216}Ra , ^{217}Ac , and ^{218}Th , have been studied with the help of the fast detection technique developed in our laboratory.¹⁾ Two previously unknown nuclei ^{217}Ac and ^{218}Th were produced in the $^{207}\text{Pb}(^{14}\text{N},4n)$ and $^{209}\text{Bi}(^{14}\text{N},5n)$ reactions, respectively. Alpha-particles were detected with a Si surface-barrier detector and their time distributions were taken between natural beam bunches of the cyclotron, being analyzed with a two-dimensional pulse-height-analyzer in the form of 256 (energy) times 16 (time) channels. Typical delayed α -spectra obtained are shown in Figs. 1 and 2. The assignment of peaks was made from their excitation functions, energies, half-lives and decay-chain relations. The half-life of ^{216}Ra has been measured in the same way by using the $^{208}\text{Pb}(^{12}\text{C},4n)$ reaction. The decay-curves of ^{216}Ra , ^{217}Ac , and ^{218}Th are shown in Fig. 3. Several long-range alphas have been also observed and assigned to transitions from short-lived isomeric states of ^{216}Ra and ^{217}Ac . The results are summarized in Table 1.

Gamma-transitions of these nuclei were also measured in the same system except that the Si-detector was replaced with a Ge(Li) counter. Construction of decay schemes from the knowledge of delayed gamma- and alpha-transitions is now in progress.

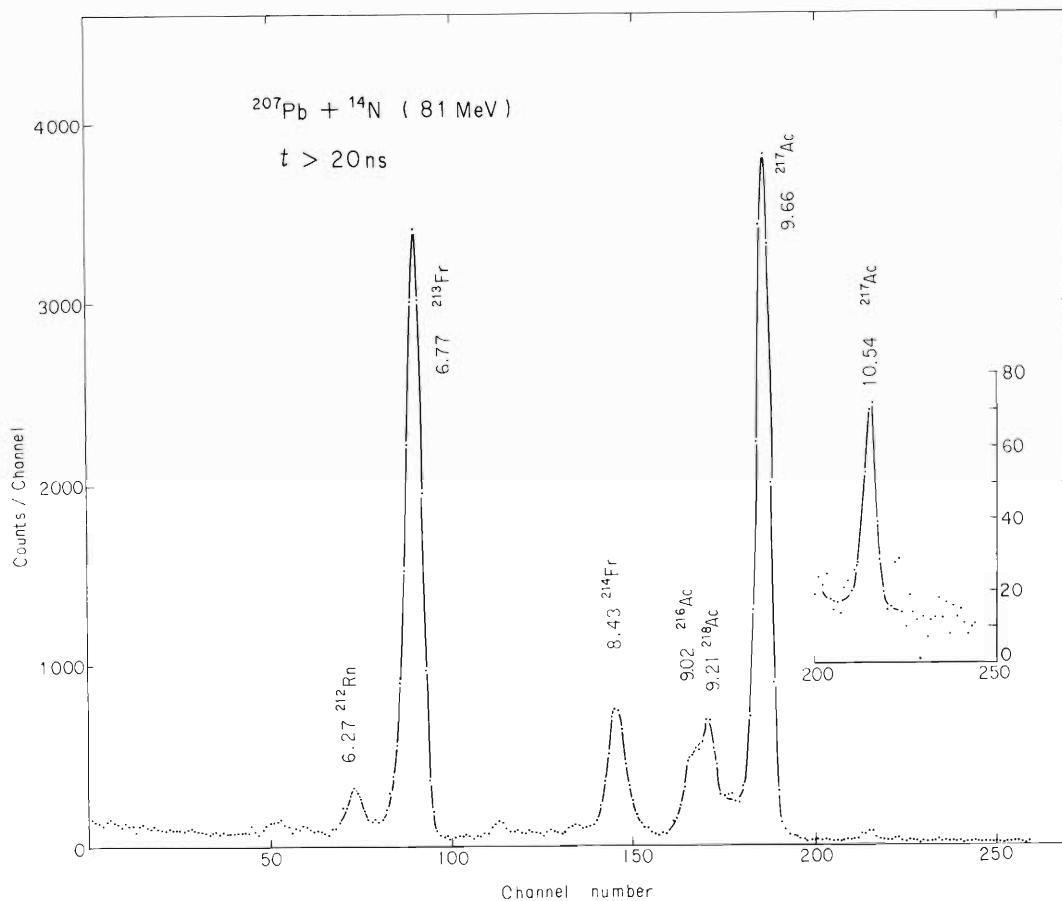


Fig. 1. A delayed alpha-spectrum following the $^{207}\text{Pb} + ^{14}\text{N}$ reaction. Energies are given in MeV.

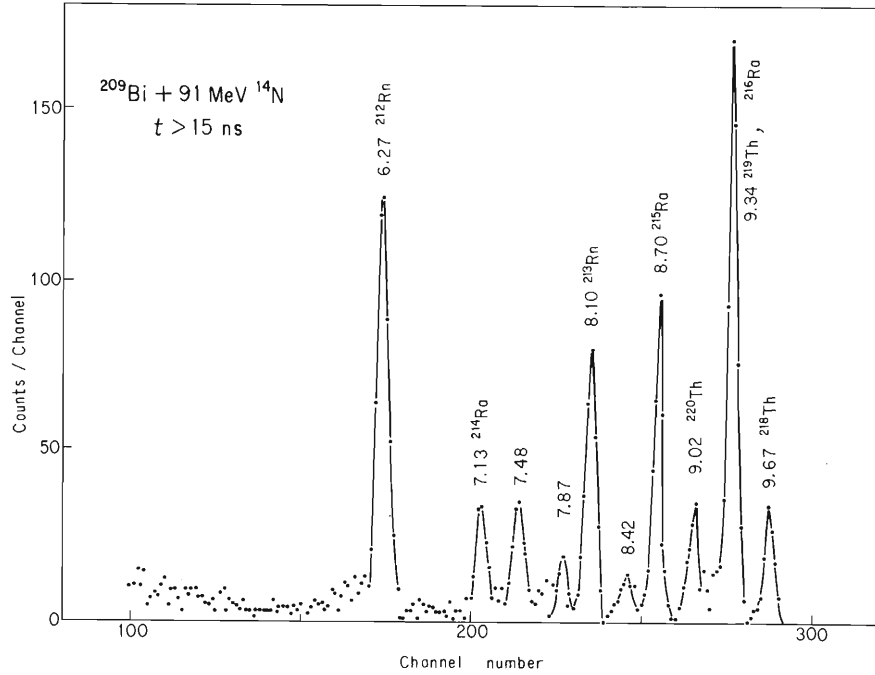


Fig. 2. A delayed alpha-spectrum following the $^{209}\text{Bi} + ^{14}\text{N}$ reaction. Energies are given in MeV.

Table 1. Experimentally observed alpha-decays from ^{216}Ra , ^{217}Ac , and ^{218}Th .

	E_α (MeV)	Q_α (MeV)	$t_{1/2}$ (ns)	Q_{sys} (MeV)	Comments
^{216}Ra	9.304 ± 0.02	9.480	216 ± 20	9.480	gnd
	9.502 ± 0.02	9.681	8 ± 1		
	(9.666)	(9.848)			
	10.111 ± 0.02	10.302	8 ± 1		
	10.424 ± 0.02	10.621	8 ± 1		
	10.751 ± 0.02	10.954	8 ± 1		
	10.952 ± 0.02	11.159	8 ± 1		
^{217}Ac	11.262 ± 0.02	11.475	8 ± 1		
	9.66 ± 0.02	9.84	100 ± 10	9.800	gnd
	10.54 ± 0.02	10.74	400 ± 100		
^{218}Th	11.13 ± 0.02	11.34	8 ± 4		
	9.67 ± 0.02	9.85	87 ± 7	9.900	gnd

Given errors for the α -decay energies are absolute. For long-range alphas errors relative to the ground-state decay are usually 0.005 MeV.

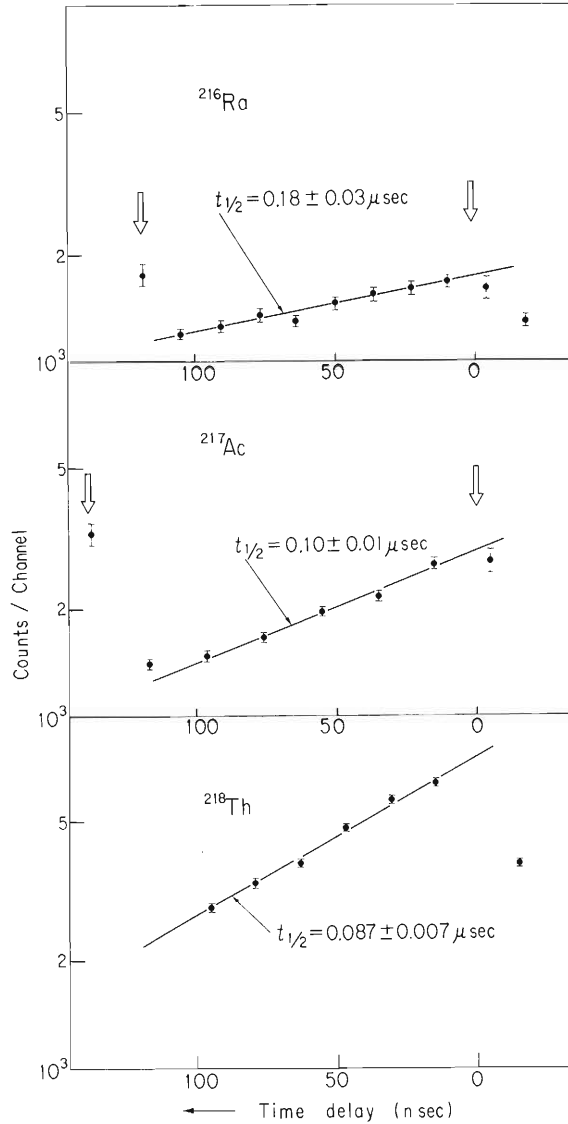


Fig. 3. Decay curves of the ground-state alpha transitions of ^{216}Ra , ^{217}Ac , and ^{218}Th .

Table 2 compares the experimental reduced α -widths of $N=128$ isotones with those calculated on the basis of the shell model. The experimental reduced width is deduced from

$$r_{\alpha}^2 = \frac{\hbar \lambda}{2} \cdot \frac{1}{P},$$

where λ is the α -decay constant and P the barrier penetrability calculated for S -wave α -particles using a pure Coulomb potential at a radius of $R = 1.57 A^{1/3}$ fm. Because absolute values of r_{α}^2 are very sensitive to the choice of R and moreover the nuclear potential was neglected in defining the barrier, only relative values of r_{α}^2 should be considered to be significant. The shell model predicts, as the simplest configuration, $[(\pi h_{9/2}^n)_{9/2} (\nu g_{9/2}^2)_0]_{9/2}^-$ for the odd parents and $[(\pi h_{9/2}^n)_0 (\nu g_{9/2}^2)_0]_0^+$ for the even-even parents. Assuming the above configuration for parent- and $\pi h_{9/2}^{n-2}$ (closed shell for neutrons) for daughter-nuclei we have calculated theoretical values of r_{α}^2 after Mang,⁶⁾ which are given in the fifth column of Table 2. Agreement with experiment is generally quite good except in the case of ^{218}Th .

Table 2. Experimental and theoretical α -reduced widths of the ground-state α -decay of N=128 isotones.

Parent nucleus	E_α (MeV)	$t_{1/2}$ (μ s)	$r_\alpha^2(\text{exp})$ (keV)	$r_\alpha^2(\text{cal})$ (keV)	Ref. for experiments
^{212}Po	8.785	0.304	1.49	1.49a)	2
^{213}At	9.080	0.11 ± 0.02	1.74	1.19	3
^{214}Rn	9.035	0.27 ± 0.02	1.79	2.38	4
^{215}Fr	9.365	< 0.5		1.79	5
^{216}Ra	9.304	0.18 ± 0.03	2.32	2.68	Present
^{217}Ac	9.66 ± 0.02	0.10 ± 0.01	1.60	1.79	Present
^{218}Th	9.67 ± 0.02	0.087 ± 0.01	3.43	2.38	Present

The reduced width of ^{212}Po is taken as a standard and set equal to the experimental reduced width.

References

- 1) T. Nomura, K. Hiruta, T. Inamura, and M. Odera: IPCR Cyclotron Progr. Rep., 6, 76 (1972); Nucl. Instr. Methods, in press.
- 2) Table of Isotopes, 6th edition (ed. by C.M. Lederer, J.M. Hollander, and I. Perlman), John Wiley & Sons, N.Y. (1966).
- 3) J. Borggreen, K. Valli, and E.K. Hyde: Lawrence Radiation Laboratory Report, UCRL-19539 (1970).
- 4) K. Valli, E.K. Hyde, and J. Borggreen: Phys. Rev., C1, 2115 (1970).
- 5) R.D. Griffioen and R.D. Macfarlane: Lawrence Radiation Laboratory Report, UCRL-10023 (1961).
- 6) H.J. Mang: Phys. Rev., 119, 1069 (1960).

5-6. g Factor Measurement of the 8^+ State in ^{86}Sr Produced in Kr Gas

O. Hashimoto, E. Matthias, K. Nakai, S. Nagamiya,
E. Recknagel, T. Yamazaki, and Y. Yamazaki

Ishihara et al.¹⁾ reported on the 8^+ isomeric state in ^{86}Sr and determined the half life of this state to be $0.46 \pm 0.03 \mu\text{sec}$ (see Fig. 1). This state was explained as a neutron-two-hole state ($\nu g_{9/2}^{-2}$) assuming ^{88}Sr to be the core. Previously, the g factor of this state was measured by Hashimoto et al.²⁾ to be $g = -0.241 \pm 0.015$ by the spin rotation method.

Our interest in the present experiment was the following two points;

1) To determine the g factor of this state more accurately to examine the additivity relation of the magnetic moment between the $9/2^+$ state in ^{87}Sr and the 8^+ state in ^{86}Sr .

2) To ascertain whether the nuclear alignment produced by the $^{84}\text{Kr}(\alpha, 2n)^{86}\text{Sr}$ reaction is preserved in Kr gas and to investigate the relaxation mechanism in the μsec region.

Natural Kr gas (^{84}Kr ; 56.9 %) was irradiated by 22-MeV α particles from the cyclotron to populate the 8^+ state. The pressure of Kr gas was 3 atm. The diameter of the target gas chamber was 8 mm and the length was 10 mm, so that recoiling ions were stopped in Kr gas. A Harvar foil of $3 \mu\text{m}$ thickness was used as the window.

To measure the g factor of the 8^+ state the stroboscopic resonance method was used. The γ -rays were observed with two NaI(Tl) counters placed at 45 and 135 degrees to the beam axis. The composite peak of 1154 keV and 1078 keV γ -rays was used for analysis. The stroboscopic resonance at $n=1$ was observed as shown in Fig. 2, from which we obtained

$$g(8^+; ^{86}\text{Sr}) = -0.242 \pm 0.004$$

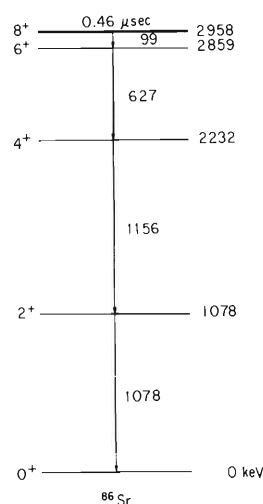


Fig. 1. Relevant energy levels of ^{86}Sr as proposed by Ishihara et al.

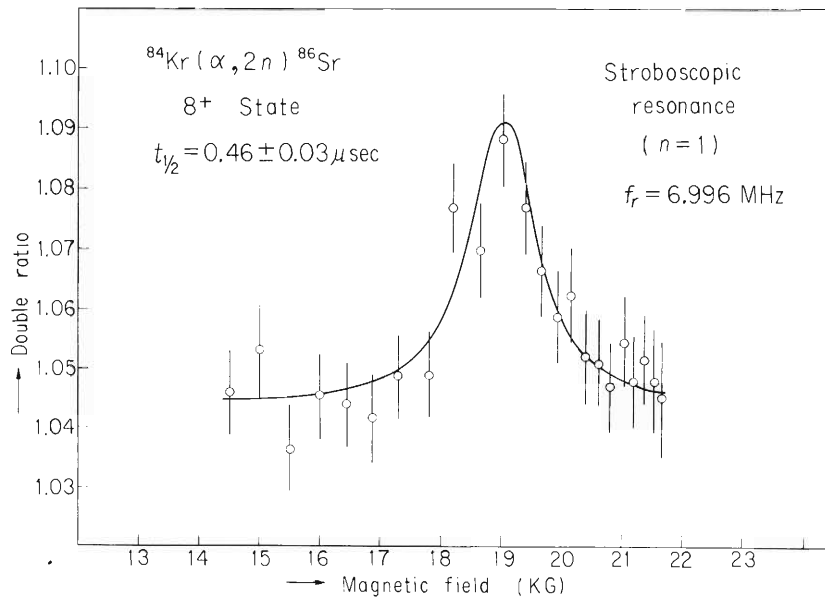


Fig. 2. The $n=1$ stroboscopic resonance. Solid curve gives the best fit assuming a Lorentzian line shape.

Table 1. Experimental and calculated g factors for ^{87}Sr and ^{86}Sr .

	Main configuration	g_{Schmidt}	$\delta g_{\text{A.H.}}^{\text{a)}}$	$g_{\text{cal}}^{\text{b)}}$	g_{exp}
^{87}Sr	$\nu g_{9/2}^{-1}$	-0.426	+0.237	-0.189	-0.2429 ^{c)}
^{86}Sr	$\nu g_{9/2}^{-2}$	-0.426	+0.210	-0.216	-0.242 \pm 0.004 ^{d)}

a) $\delta g_{\text{A.H.}}$ is calculated by the theory of Arima and Horie.

b) $g_{\text{cal}} = g_{\text{Schmidt}} + \delta g_{\text{A.H.}}$.

c) From Ref. 3).

d) Value obtained in this experiment.

The configuration of the ground state in ^{87}Sr is considered to be the one-hole state of the $g_{9/2}$ neutron. The g factor of this state is known to be $g = -0.2429$ by the NMR experiment³⁾ which is very close to the present result. This shows that the additivity of the magnetic moment between the $9/2^+$ state in ^{87}Sr and the 8^+ state in ^{86}Sr holds well, though these g factors deviate from the Schmidt estimate of -0.425 . This deviation $\delta g = g_{\text{exp}} - g_{\text{Schmidt}} = 0.18$ is nearly accounted for by the theory of Arima and Horie ($\delta g_{\text{1st}} = 0.23$) (see Table 1).

The width of the stroboscopic resonance observed was $\sim 7\%$ which is not considerably broader than the natural width of the resonance (6.2%). The relaxation time was estimated to be of the same order as or longer than the mean lifetime of the 8^+ state in ^{86}Sr , namely $T_{\text{relax}} \gtrsim 0.5 \mu\text{sec}$.

The spin relaxation process in Kr gas could be divided into two stages. In the first stage, recoiling Sr ions travel through the Kr gas and were slowed down very quickly to thermal energy by atomic collisions with Kr atoms. The second stage concerns with a state when Sr ions have been thermalized in Kr gas. Because of the high pressure of the Kr gas and the high velocity of the recoiling atom, the correlation time is so short in the first stage that the nuclear alignment is expected to be preserved well by frequent atomic collisions. In the second stage the correlation time is too long to randomize hyperfine fields caused by unpaired s electrons if they exist. However, the present result showed that the nuclear alignment was preserved longer than 0.5 μ sec. This indicates that the hyperfine interactions must be very weak or do not exist. This situation can be realized if the Sr atoms were in the neutral atomic state, 1S_0 , and the mean time for the neutral Sr atoms picking up an electron in Kr gas was longer than the nuclear lifetime of $\sim 0.5 \mu$ sec. It is also noticed that the doubly charged Sr ion has an atomic closed-shell configuration, namely Kr, which produces no hyperfine field. As for the quantitative argument the study is still in progress.

References

- 1) M. Ishihara, H. Kawakami, N. Yoshikawa, M. Sakai, and K. Ishii: Phys. Letters, 35B, 398 (1971).
- 2) O. Hashimoto, T. Nomura, T. Yamazaki, K. Miyano, and M. Ishihara: Contr. Intern. Conf. Nucl. Moments Nucl. Struct., 3-16 (1972).
- 3) Table of Isotopes, 6th edition (ed. by C.M. Lederer, J.M. Hollander, and I. Perlman), John Wiley & Sons, N.Y. (1966)
- 4) A. Arima and H. Horie: Progr. Theor. Phys., 12, 623 (1954).

6. NUCLEAR INSTRUMENTATION

6-1. A Dual Ge(Li) Gamma-Ray Spectrometer for Nuclear Study

M. Okano, Y. Tendow, T. Katou, K. Izumo,
H. Kumagai, and T. Hamada

A standard gamma-ray spectrometer using a semiconductor detector has been employed for measurements of gamma-rays accompanying nuclear reactions as well as those from radioactive nuclides produced by the cyclotron.^{1), 2)}

Recently, a new Ge(Li) detector was added to the detector assembly of the standard spectrometer, and a gamma-ray spectrometer consisting of a pair of Ge(Li) detectors mounted inside a split annulus of NaI(Tl) scintillator was constructed. The dual Ge(Li) gamma-ray spectrometer system is expected not only to use for studying characteristics of coincidence of gamma-rays but also to find applications in the analysis of radionuclides that emit coincident gamma-rays or multiple coincident gamma-rays.

The new Ge(Li) detector is a closed-end coaxial type with an active volume of 29 cm³ (ORTEC, System Model No. 8301-0325). The detector cryostat has an aluminum end cap of 8 inch in length and 2 ~ 1/4 inch in diameter, which is able to insert into the annulus type NaI(Tl) scintillator of the standard gamma-ray spectrometer. Its peak efficiency is 1.5 % for a ¹³⁷Cs 662 keV gamma-ray source placed on the front surface of end cap, and the resolution is 2.3 keV FWHM for ⁶⁰Co 1332 keV gamma-ray.

The detector is mainly used for a coincidence gate and its signal is sent to an ADC connected with a digital gate unit. The function of this unit is to convert a selected address to a fixed channel. This pulse height selection system, combined with a two-parameter multichannel system, will digitize the pulse height to 4095 channel full scale with provisions of four selective lower- and upper-level pair digital gates.

In Fig. 1 is shown a block diagram of the arrangement used for a coincidence dual Ge(Li) two-parameter spectrometer.

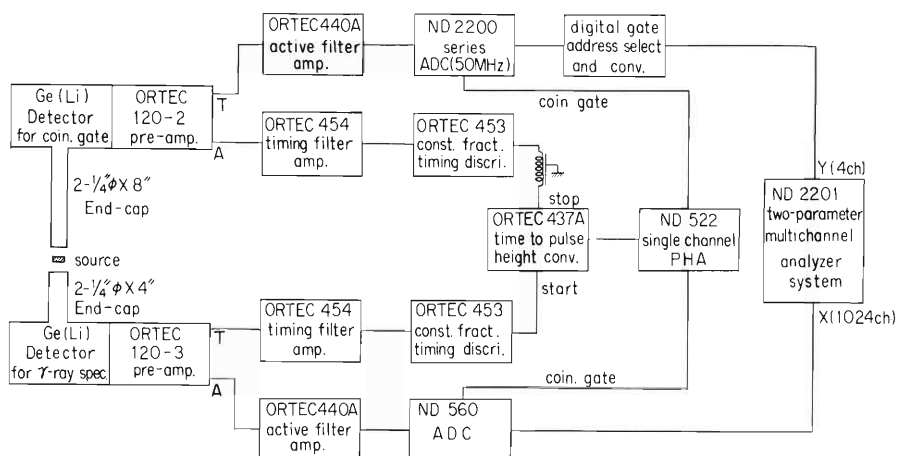


Fig. 1. Block diagram of dual Ge(Li) coincidence γ -ray spectrometer.

References

- 1) M. Okano, A. Hashizume, Y. Awaya, Y. Tendow, K. Kato, and T. Hamada: IPCR Cyclotron Progr. Rep., 2, 110 (1968).
- 2) M. Okano, Y. Tendow, T. Katou, K. Izumo, and T. Hamada: *ibid.*, 5, 75 (1971).

6-2 Particle Identification Study for $Z=3$ to $Z=7$ Particles Using a Power-Law Type Particle Identifier

S. Nakajima, I. Kohno, I. Yamane, M. Yoshie,
M. Odera, and H. Kamitsubo

A combination of a counter telescope consisting of ΔE and E detectors and a power-law type particle identifier was used to identify heavy particles produced in nuclear reactions induced by heavy ions. Satisfactory results were obtained by adjustment of the circuit parameters.

This type of particle identifier employs an empirical range-energy relation¹⁾

$$R = aE^n, \quad (1)$$

where R =particle range in the absorber,

a =constant depending on the type of particle,
 n =constant (about 1.73 for $Z=1$ and 2 particles),
 E =incident particle energy.

Figure 1 shows the range-energy relations²⁾ for several particles. Equation 1 is satisfied well by the light particles such as p , d , α etc., but apparently heavier particles do not follow such a simple law. However, if the exponent of the power law is treated as an adjustable parameter, Eqn. 1 can be applicable to heavier particles at high energies or at a limited range of energy.

Identification study of heavy particles with this method was undertaken by bombarding a ^{12}C target and a ^{46}Ti target with a 90 MeV ^{14}N beam. The block

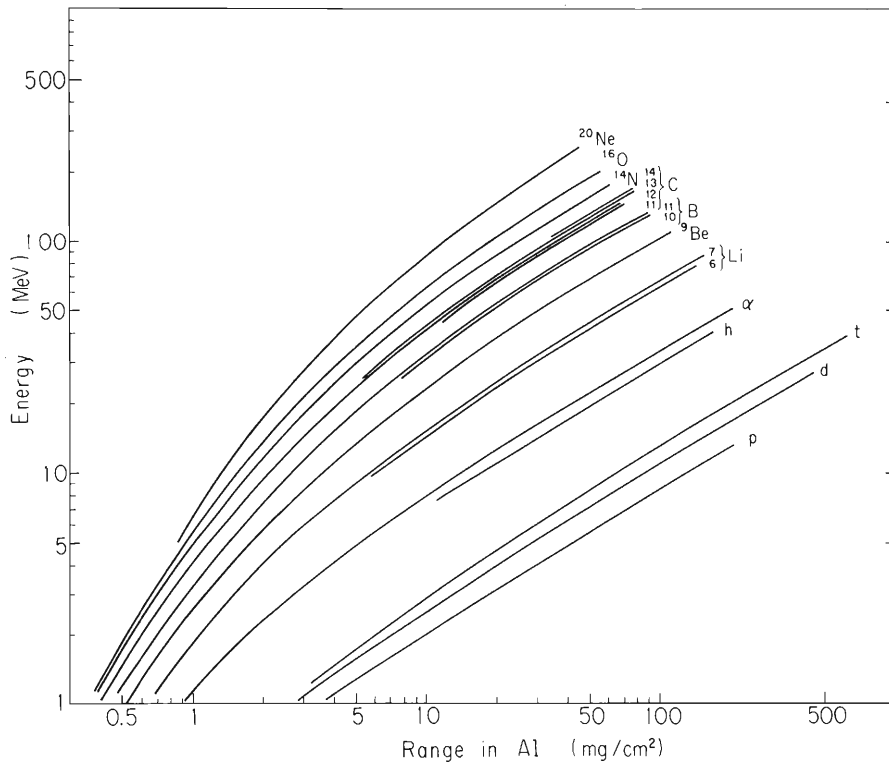


Fig. 1. Range-energy relationship.

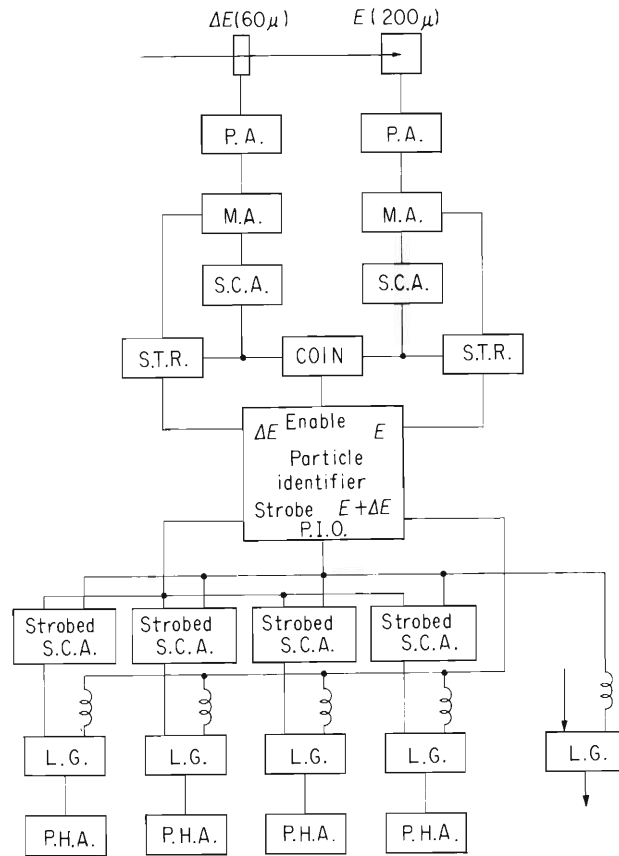


Fig. 2. Block diagram of electronics.

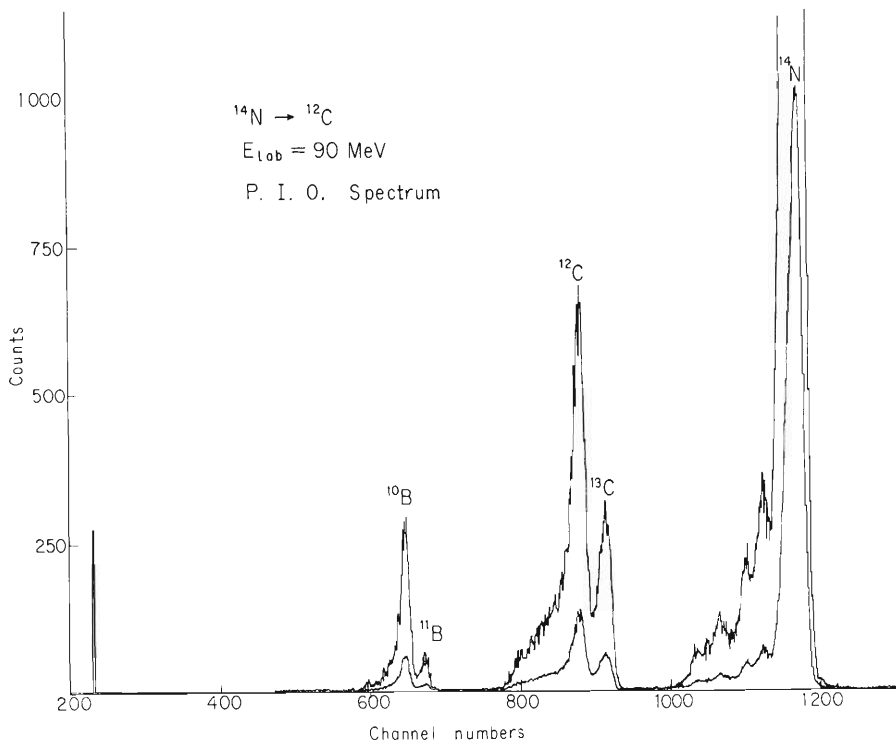


Fig. 3. A particle identifier spectrum resulting from the bombardment of ^{12}C with 90 MeV ^{14}N beam.

diagram of the electronic circuit used is shown in Fig. 2. A totally depleted silicon detector was used as a ΔE detector, and a silicon detector of $200\ \mu$ thick was used as an E detector. The thickness of the ΔE counter ($60\ \mu$) was chosen in such a way that heavy particles of interest lost about a half of their initial energies in it. By use of this ΔE counter, the energies of the heavy particles could be detected in the region above 50 MeV, where the range-energy relations of heavy particles could be approximated by Eqn. 1 with a constant value for n . The exponent of the power law was varied between 1.75 and 1.45. When the value was set at about 1.73 or 1.45, the identifier spectrum did not represent a clear separation because of a tail caused by a deviation of Eqn. 1 from the real range-energy curve. Setting the value at about 1.6, we obtained satisfactory results as shown in Fig. 3 and Fig. 4.

A greater energy range can be covered by choosing properly the thickness of the ΔE counter and the value of exponent according to the energies of particles desired.

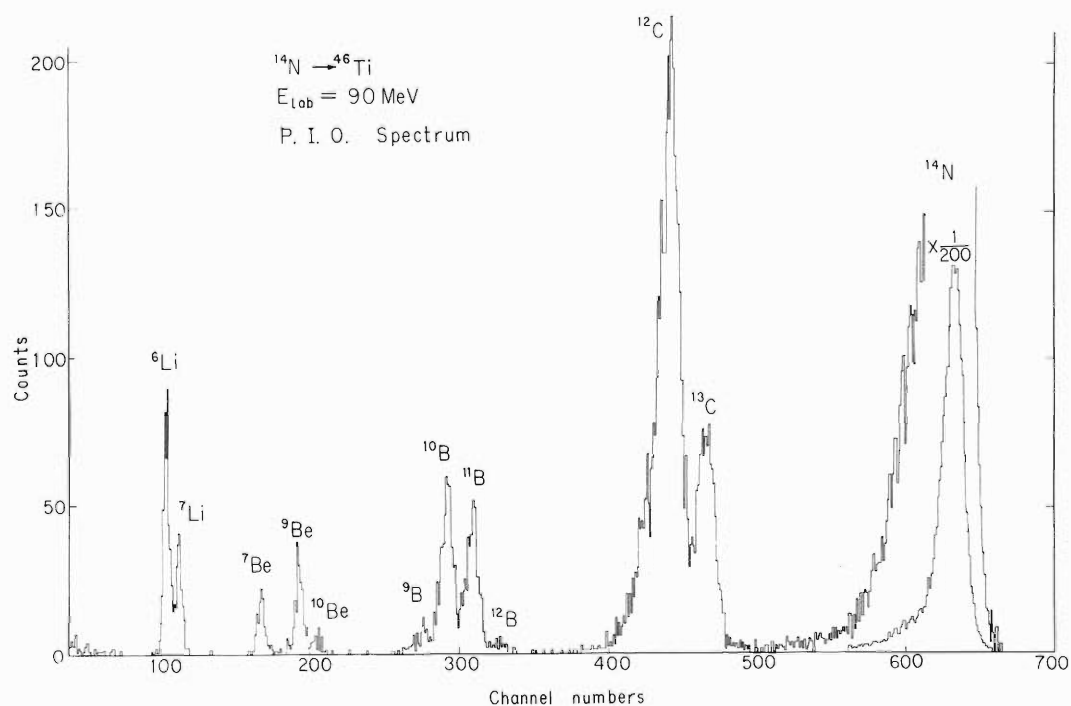


Fig. 4. A particle spectrum resulting from the bombardment of ^{46}Ti with 90 MeV ^{14}N .

References

- 1) F.S. Goulding, D.A. Landis, J. Cerny, and R.H. Pehl: Nucl. Instr. Methods, 31, 1 (1964).
- 2) L.C. Northcliffe and R.F. Schilling: Nucl. Data Tables, A7, 233 (1970).

6-3. On a Model of Wire Spark Chamber with Ferrite Memory Cores for Broad Range Magnetic Spectrometer

J. Fujita and S. Takeda

The outline of a model of the wire spark chamber with ferrite memory cores was described in a previous report.¹⁾ We give here methods to solve several problems and results of test using β -rays.

An abbreviated block diagram is shown in Fig. 1. A new gate was introduced into the reading-out circuit in order to prevent position information in the cores from being destroyed by occurrence of spark. The fast signal from a photomultiplier which triggers the high voltage pulser closes the gate for two microseconds until the storm of

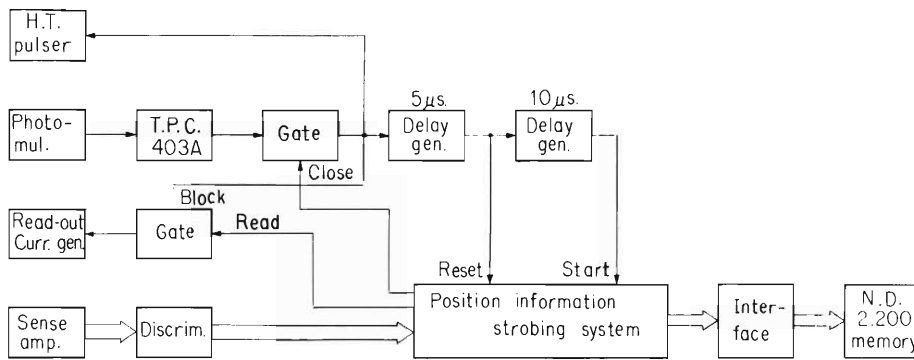


Fig. 1. An abbreviated block diagram of electric system in wire spark chamber.

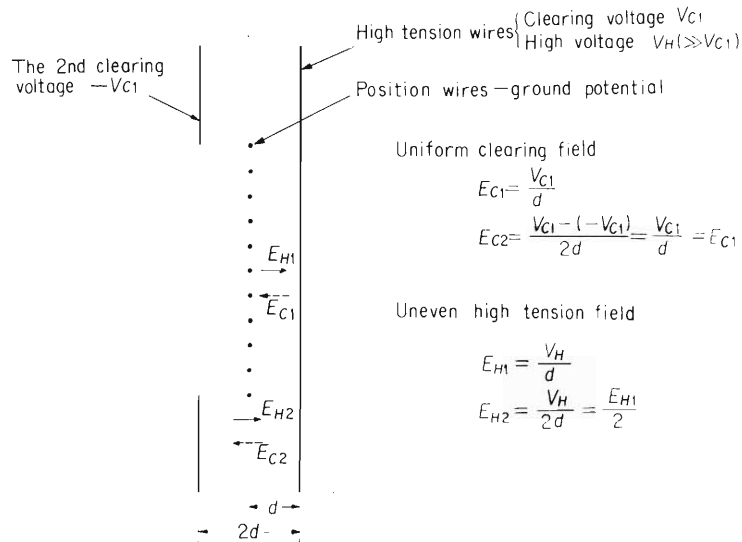


Fig. 2. The effect of the 2nd clearing plate on the clearing and high tension fields.

spark current becomes quiet. After this signal has been held for $5 \mu\text{sec}$ by a delay generator, the logic circuit is caused to reset and start reading-out. Also a noise picked up by sense leads was minimized by twisting each sense wire in order that they are not exposed to the magnetic flux from the read-out and spark currents.

Residual ions existing outside of the gap between wire planes are not swept away by a clearing field and bring about fault sparks, especially in the neighborhood of both edges of wire planes. The other clearing plate was set parallel to wire planes at a distance twice the wire gap from the high tension wire plane and given a potential of equal magnitude but of opposite polarity to the clearing voltage on the high tension wires. As seen in Fig. 2, the clearing field is distributed uniformly in the horizontal direction, but the high tension field outside of the gap becomes half of its inside. Thus, error sparks in the neighborhood of both edges are prevented.

Any trouble does not occur in the upper and bottom ends of the gap because of steep decrease of high tension field.

Electrical principle of the wire spark chamber is shown in Fig. 3 (a). The equivalent circuits of the chamber are shown in Fig. 3 (b) and Fig. 3 (c). The transmission line from the high tension pulser has characteristic impedance of 50Ω . R_1 , R_2 , and R_3 are varied appropriately to match the characteristic impedance and limit spark current.

Tests were performed in the following three cases:

- i) $R_1 = 0 \Omega$ $R_2 = \gamma \Omega$ and $R_3 = 100 \Omega$
- ii) $R_1 = 50 \Omega$, $R_2 = \gamma \Omega$ and $R_3 = 100 \Omega$
- iii) $R_1 = 50 \Omega$, $R_2 = \gamma \Omega$ and $R_3 = 2 \text{ k}\Omega$.

Here, γ is the total amount of resistance due to a stainless steel wire, a conductive glue and contact resistance between them. The value of γ has discrete distribution between 50 to 200Ω . The values of the high tension, the first and second clearing fields and the He-gas pressure are fixed at 5.5 kV, +31 and -31 V and one atmosphere, respectively. In the second case there appear no spark and no count because of decrease of effective high voltage by one-third. In the third case there occur sparks and counts but noise is larger than in the first case. Increment of R_2 by addition of resistance of 100Ω in the first case induces further disturbance of high tension pulse so that the information of position stored in the cores is destroyed. The first case without modification is chosen as a better combination.

A test of space-resolution is performed in a manner of Fig. 4 (a) and its result is shown in Fig. 4 (b). Operating conditions are the same as mentioned above except

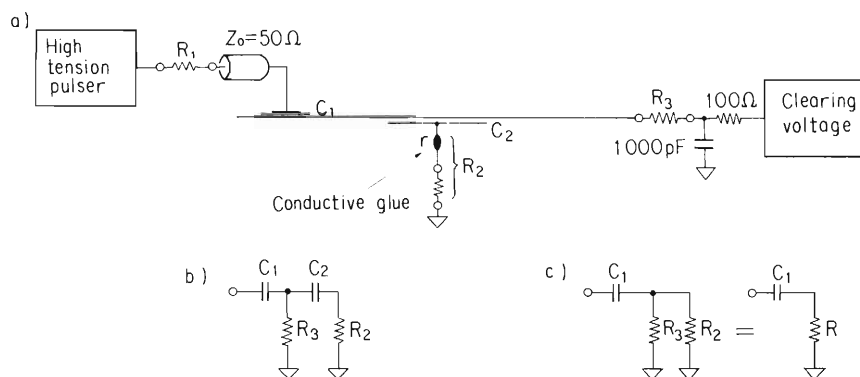


Fig. 3. Principle and equivalent circuits of the wire spark chamber. a) shows principle. b) and c) are equivalent circuits in the absence and presence of spark respectively.

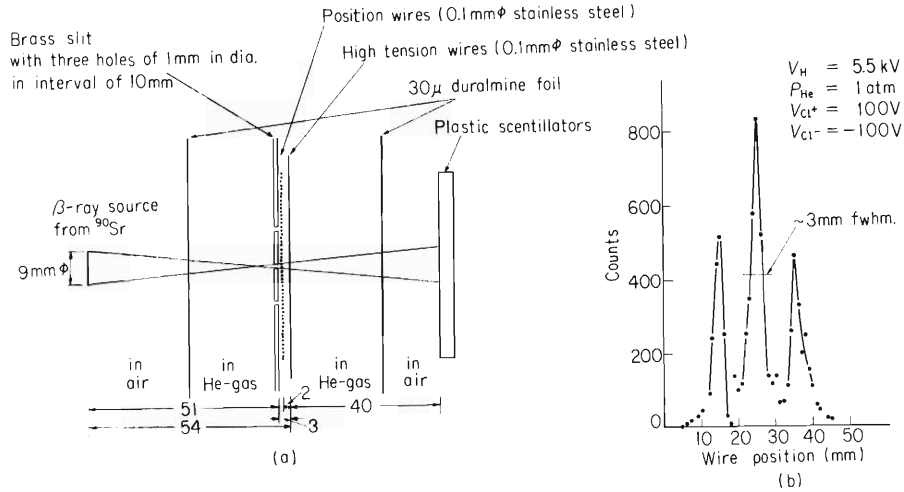


Fig. 4. A test result of spatial resolution with Model-I. a) Source and slit system used. b) A result of spatial resolution in this case.

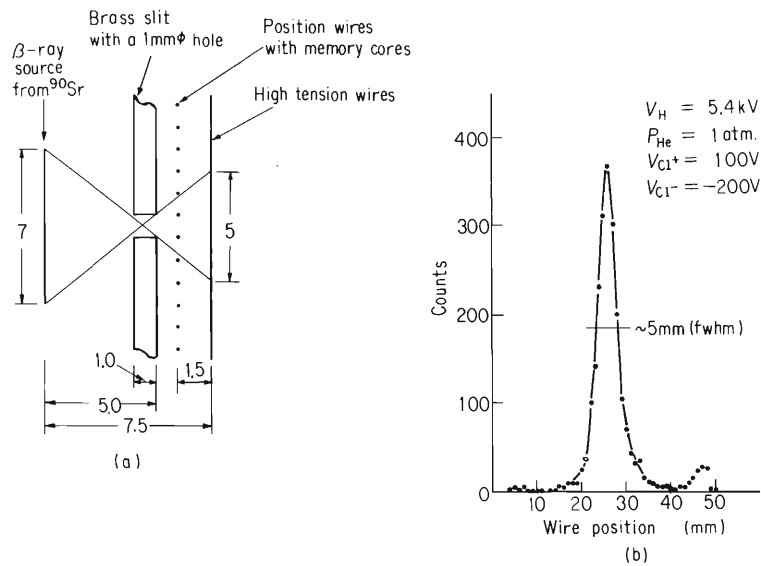


Fig. 5. A test result with Model-II. a) Source and slit system used. b) A result of spatial resolution in this case.

that clearing voltages are changed into +100 and -100 V. Space-resolution of about 3 mm full width at half maximum was obtained.

In order to prevent extra spark, geometrical modification of the chamber was performed. A model-II is the same as the model-I in principle. In the model-II, phosphor bronze wires of 0.1 mm diameter are soldered on both surfaces in a printed circuit board with a thickness of 1.5 mm. A series resistance of 20 Ω is inserted to the input terminal of a high tension wire plate to limit the spark current. A test result of spatial resolution is shown in Fig. 5 (b). High tension voltage and He-gas pressure are 5.4 kV and one atmosphere. Clearing voltages are +100 and -200 V. The model-II shows remarkable characteristics for most part of sparks to localize at one wire.

Worse space-resolution of 5 mm in Fig. 5 originates from the property of the slit system.

Counting rate of the system is governed by the dead time of the high tension pulser which is about 75 m sec.

Reference

- 1) J. Fujita and S. Takeda: IPCR Cyclotron Progr. Rep., 5, 68 (1971).

6-4. Measurements of Ion Optical Properties of A Particle analyzer by Particle Beams

N. Nakanishi, S. Motonaga, S. Takeda, M. Hemmi,
T. Inoue, J. Fujita, and H. Nakajima

Measurements of optical properties of the magnetic analyzer were carried out by two methods, the floating-wire method and the method using particle beams. The former was employed in order to estimate roughly the position of horizontal focal line, dispersion factor and incident angle to the focal line, and the latter was adopted in order to obtain the relation of horizontal focal point to beam radius, solid angle and dispersion factor. A part of the results was already reported.^{1),2)}

Proton beams from the cyclotron were analyzed in the accuracy of less than 0.1 % at 13.80 MeV, and scattered elastically in the direction of 14.75° by Au of $32.8 \mu\text{g}/\text{cm}^2$ thickness. Nuclear emulsion was used as particle detector. Dispersion factors projected on the focal line and momentum resolutions were estimated from the

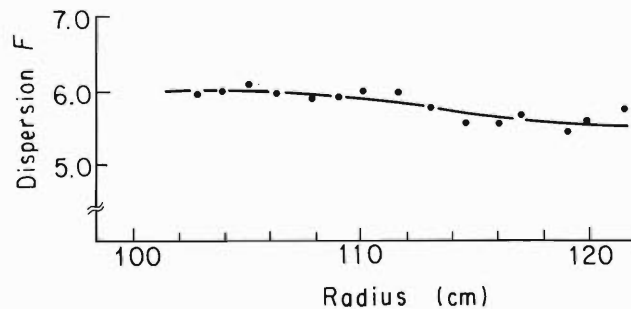


Fig. 1. Dispersion factor vs. radius of curvature of beam.

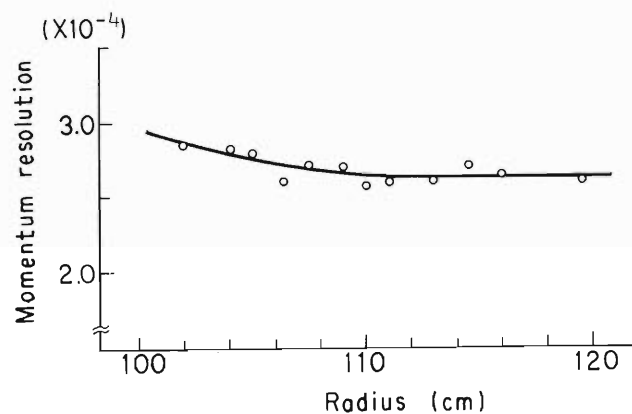


Fig. 2. An example of momentum resolution vs. radius of curvature of beam. Proton beam of 13.8 MeV energy was scattered elastically at an angle of 14.75° by Au-foil of $32.8 \mu\text{g}/\text{cm}^2$ thickness and was detected by nuclear emulsion on the focal line.

measurements of focusing positions corresponding to the fields B and $B + \Delta B$. Figures 1 and 2 show the dispersion factor and momentum resolution, respectively. Solid angle was also estimated to be within the range from 3.1×10^{-4} sr to 6.1×10^{-4} sr when the defining slits were set at an solid angle of 8.2×10^{-4} sr.

The relation between beam radius and focusing position was obtained to examine the influence of the change of field distribution in magnetic fields ranging from 2700 to 3230 gauss for alpha beam from ^{210}Po , from 4500 to 5250 gauss for 14 MeV proton beam, from 4570 to 5550 gauss for 16 MeV alpha beam, and from 7440 to 8850 gauss for 40 MeV alpha beam. An example for the 14 MeV proton beam is shown in Fig. 3. Systematic dependence on the field strength was observed. However it is so small that we can not see it in the figure and can be neglected in the normal use.

The measurement was also done on the effect of hysteresis, that is, the change of focusing position due to different processes of field-setting to the same field strength. Magnetic field was set in two ways. One was to set the exciting current directly from zero to the necessary value and the other was to set the current at the necessary value after being kept at twice of it for 15 minutes. Maximum difference of 5×10^{-4} of momentum was observed.

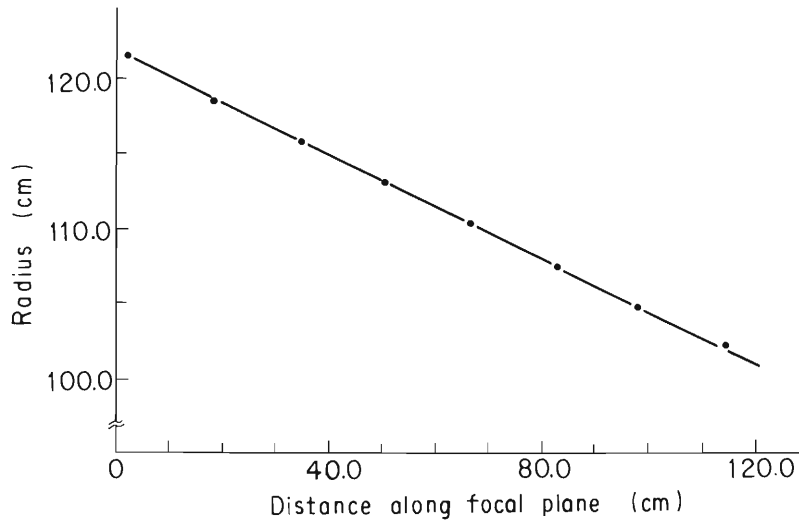


Fig. 3. Relation of the horizontal focusing point with the corresponding beam radius in the field.

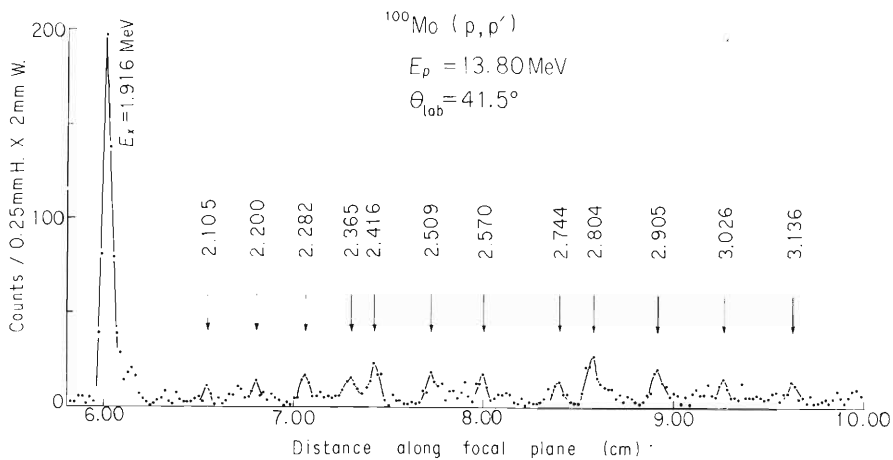


Fig. 4. Proton spectrum of reaction $^{100}\text{Mo}(p, p')^{100}\text{Mo}$. Energies of some excited levels are also shown.

The proton energy spectrum for the reaction $^{100}\text{Mo}(p, p')^{100}\text{Mo}$ is shown in Fig. 4 in the excitation-energy range from 1.9 MeV to 3.2 MeV. The proton beam of 13 MeV was scattered inelastically at an angle of 41.5° by a ^{100}Mo -foil of 1.08 mg/cm^2 thickness and was detected by nuclear emulsion on the focal line.

References

- 1) S. Motonaga, N. Nakanishi, K. Matsuda, M. Hemmi, H. Ono, and Y. Awaya: IPCR Cyclotron Progr. Rep., 3, 77 (1969).
- 2) N. Nakanishi, S. Motonaga, K. Matsuda, S. Takeda, M. Hemmi, H. Nakajima, and Y. Awaya: *ibid.*, 4, 96 (1970).

7. RADIOCHEMISTRY

7-1. The Behavior of Trace Amounts of ^{18}F Atoms Trapped on Metal Surfaces

M. Aratani

In the course of studies on the charge spectrum of ions derived from the decay of ^{18}F trapped on metal surface,¹⁾ it has become clear that the trapping of ^{18}F on the surface depends upon the chemical nature of the metal surface.

The metals employed for the trapping of ^{18}F were aluminum, copper, zinc, and stainless steel. The radiofluorine, ^{18}F , was produced by the $^{16}\text{O}(^3\text{He},p)^{18}\text{F}$ reaction.²⁾ A stream of oxygen gas was bombarded with ^3He beams from the cyclotron in an irradiation tube especially designed for this purpose. After the metal surfaces had been treated with a series of cleaning processes, the metal plates (10 mm \times 20 mm \times 0.5 mm) were exposed to the flow of bombarded gas at the outlet of the irradiation tube. A part of the ^{18}F in the gas stream was trapped on the surfaces of the metal plates. After each plate had been exposed to the gas stream, the annihilation gamma activities of ^{18}F on each plate were measured by means of a scintillation counter. The decrease in the activities of the trapped ^{18}F with the time was measured with or without vacuum pumping. In the measurements with the vacuum pumping, the samples were transferred to a chamber. The chamber could be evacuated down to 10^{-4} Torr in a much shorter time than the half-life of ^{18}F . The counting rates of the samples were followed for at least two half-lives of ^{18}F . In the measurements without vacuum pumping, the samples were kept in a desiccator and the counting rates of the samples were measured in the same way as has been described above.

In every run of the measurements without vacuum pumping, the decrease in the activity of the ^{18}F on the metal surface as a function of the time was found to be linear in the semilogarithmic plots, and the decay of the activity agreed with that of ^{18}F . The measurements with vacuum pumping, however, showed different results. The difference was that the decrease in the activity of the trapped ^{18}F , on the surface samples with the time was not linear in the semilogarithmic plots in every run. The

Table 1. Exhausted fractions (f_E) and residual fractions (f_R) of ^{18}F atoms on trapping metals.

Trapping metal	f_E	f_R
Aluminum	0.16	0.84
Copper	0.86	0.14
Zinc	0.62	0.38
Stainless steel	0.14	0.86

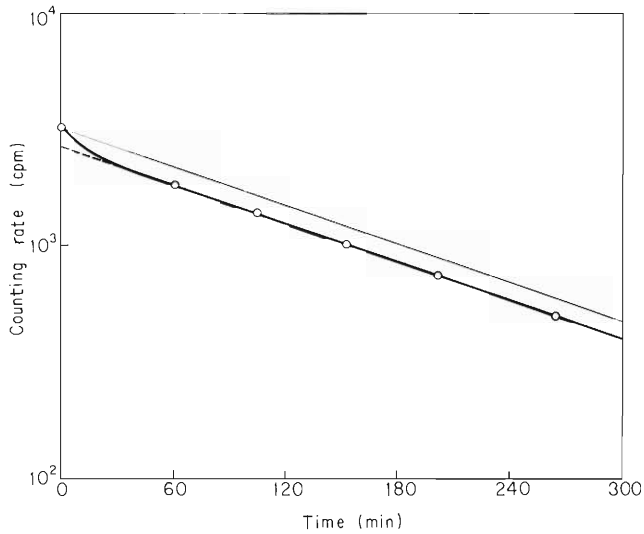


Fig. 1. Changes with time in counting rates of ^{18}F on aluminum plates under vacuum pumping (thick line) and without it (thin line).

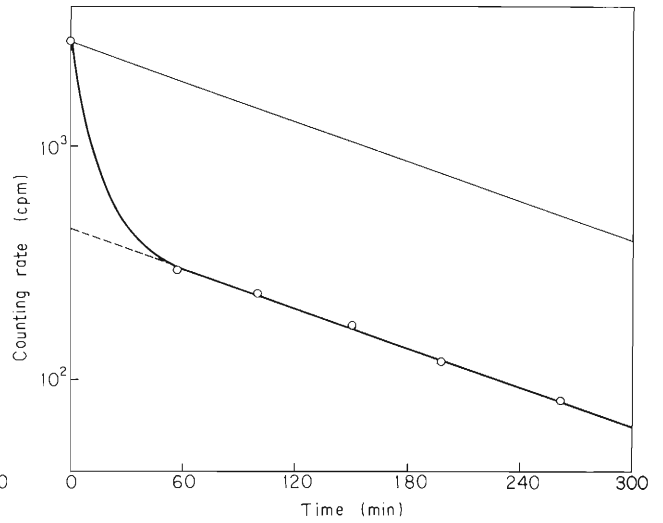


Fig. 2. Changes with time in counting rates of ^{18}F on copper plates under vacuum pumping (thick line) and without it (thin line).

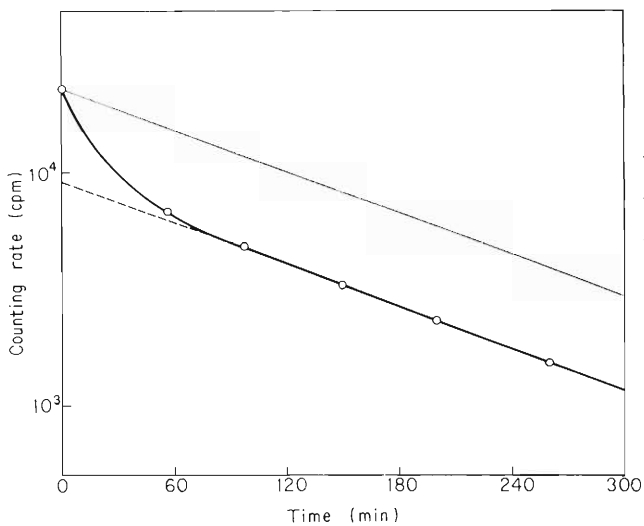


Fig. 3. Changes with time in counting rates of ^{18}F on zinc plates under vacuum pumping (thick line) and without it (thin line).

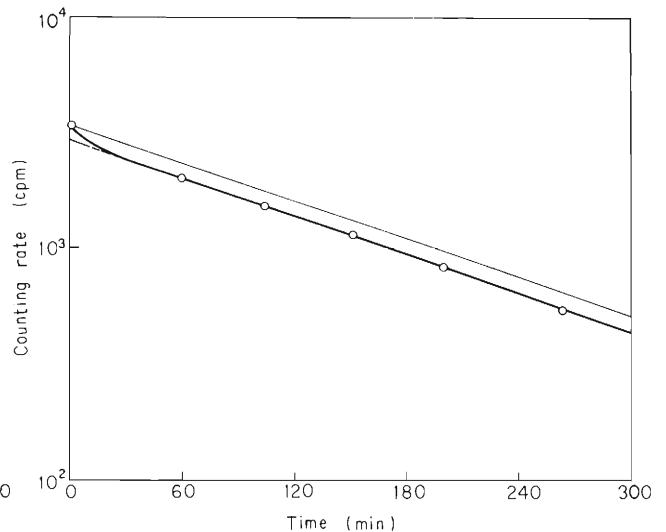


Fig. 4. Changes with time in counting rates of ^{18}F on stainless steel plates under vacuum pumping (thick line) and without it (thin line).

results are shown in Fig. 1 (aluminum), Fig. 2 (copper), Fig. 3 (zinc) and Fig. 4 (stainless steel).

The linear part of each curve corresponds to the decay of ^{18}F . The non-linear part can be interpreted in terms of the stripping of a fraction of ^{18}F from the metal plates during the vacuum pumping. The strippable fraction can be estimated by the calculation of $(C_0 - N_0)/C_0$, where C_0 is the total counting rate of the sample at $t = 0$, and where N_0 is the counting rate obtained by extrapolating the linear part of the activity curve of the sample to $t = 0$. The fraction of ^{18}F sticking on the surface after the vacuum pumping is then N_0/C_0 .

The results demonstrate that the trapping of trace amounts of ^{18}F on the metal surface depends upon the chemical nature of the metal, and that aluminum and stainless steel are suitable metals for providing a stable deposition of trace ^{18}F atoms on the surface under a vacuum.

References

- 1) S. Yokoi, M. Aratani, and T. Nozaki: IPCR Cyclotron Progr. Rep., 5, 88 (1971).
- 2) T. Nozaki, Y. Tanaka, A. Shimamura, and T. Karasawa: Intern. J. Appl. Radiat. Isotopes, 19, 27 (1968).

7-2. A Mössbauer Spectroscopic Study of Chemical States of ^{119}Sn after the EC Decay of ^{119}Sb in Sb_2O_3 and TeO_2

F. Ambe, S. Ambe, and N. Saito

As a part of a series of investigations¹⁾ of the chemical states of dilute impurity atoms produced in solids by nuclear decay, the valence state of ^{119}Sn after the EC decay of ^{119}Sb was determined in Sb_2O_3 and TeO_2 by Mössbauer emission spectroscopy.

The ^{119}Sb (38.0 h) and $^{119\text{m}}\text{Te}$ (4.7 days) were produced by the p- and α -irradiation of tin plates respectively. The nuclides were separated from tin and were purified radiochemically. $^{119}\text{Sb}_2\text{O}_3$ was obtained by the hydrolysis of a 3M HCl solution of ^{119}Sb (III) with NH_4OH . The precipitate was dehydrated at 120°C and sublimed in a vacuum at 500°C . $^{119\text{m}}\text{TeO}_2$ was prepared by neutralizing an alkaline solution of $^{119\text{m}}\text{Te}$ (IV) with 2 M acetic acid. The precipitate was dried at 120°C in air. The samples were identified by their Debye-Scherrer patterns. The $^{119\text{m}}\text{TeO}_2$ samples were let stand in liquid nitrogen until the ^{119}Sb attained a state of radioactive equilibrium with $^{119\text{m}}\text{Te}$. The Mössbauer emission spectra of ^{119}Sn in the $^{119}\text{Sb}_2\text{O}_3$ and $^{119\text{m}}\text{TeO}_2$ samples were measured at liquid nitrogen temperature against BaSnO_3 . Typical spectra thus obtained are shown in Fig. 1.

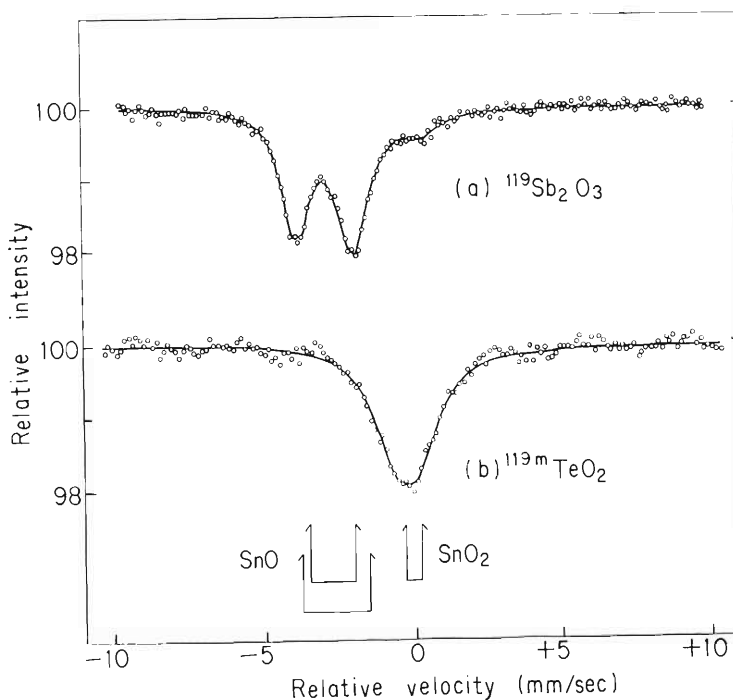


Fig. 1. ^{119}Sn -Mössbauer emission spectra of (a) $^{119}\text{Sb}_2\text{O}_3$ and (b) $^{119\text{m}}\text{TeO}_2$ at $78 \pm 1^\circ\text{K}$ against BaSnO_3 at $296 \pm 2^\circ\text{K}$. In the abscissa a velocity of approach is taken positive.

The emission spectra of $^{119}\text{Sb}_2\text{O}_3$ in the cubic modification are dominated by two lines, which can be identified as a quadrupolar doublet due to Sn(II), with oxygen ions as ligands (see Fig. 1 (a)). The identification is based on the fact that the isomer shift, 2.91 mm/sec, and the quadrupole splitting, 1.90 mm/sec, do not differ much from those of the tetragonal and rhombic SnO.²⁾ The subsidiary peak close to the zero relative velocity can similarly be assigned to a Sn(IV) state. These assignments allow us to conclude that the ^{119}Sn atoms produced by the EC decay of $^{119}\text{Sb}_2\text{O}_3$ are preferentially stabilized in the Sn(II) state, if the recoilless fraction is assumed to be of the same order of magnitude for the Sn(II) and Sn(IV) states. In case of the Sb_2O_3 samples, which had not been sublimed, the fraction of the Sn(IV) line was much larger than in the sublimed samples, although the Sn(II) doublet was still dominant.

The ^{119}Sn produced by the successive EC decays of $^{119\text{m}}\text{Te}$ via ^{119}Sb in the TeO_2 matrix gave a broad emission line attributable to a Sn(IV) state (see Fig. 1 (b)). The isomer shift, 0.19 mm/sec, is slightly higher than the corresponding value for SnO_2 . The quadrupole splitting, computed on the assumption that the peak is an unresolved symmetric doublet of quadrupolar origin, amounts to 0.9 mm/sec. No line was detected in the region of Sn(II) within the limits of the sensitivity of measurement. Although the valence state of ^{119}Sb in the $^{119\text{m}}\text{TeO}_2$ can not be determined by Mössbauer or other conventional physical techniques, a radiochemical determination has shown that about sixty percent of the ^{119}Sb is in the Sb(III) state, and the rest, in the Sb(V) state, after the EC decay of $^{119\text{m}}\text{Te}$ in TeO_2 .³⁾ Summing up these observations, it can be concluded that a large part of the ^{119}Sb atoms were in the Sb(III) state, presumably with oxide ions as ligands, after the EC decay of $^{119\text{m}}\text{Te}$ in the TeO_2 , and they turned into ^{119}Sn in the tetravalent state with the second EC decay. This contrasts with the results on $^{119}\text{Sb}_2\text{O}_3$, in which the majority of ^{119}Sn was in the Sn(II) state after the decay of ^{119}Sb (III) with oxide-ion ligands. These observations suggest the importance of the matrix in determining the final valence state of ^{119}Sn . The appearance of ^{119}Sn only as Sn(IV) in TeO_2 is in accord with the similarity of the crystal structures of TeO_2 and SnO_2 (rutile type) and the fact that the stabilization of ^{119}Sn in the Sn(IV) state requires no charge compensation, as in the case of the IT in $^{119\text{m}}\text{SnO}_2$.

References

- 1) F. Ambe, H. Shoji, S. Ambe, M. Takeda, and N. Saito: IPCR Cyclotron Progr. Rep., 4, 115 (1970); *ibid.*, 5, 85 (1971); Chem. Phys. Lett., 14, 522 (1972).
- 2) J.D. Donaldson and B.J. Senior: J. Inorg. Nucl. Chem., 31, 881 (1969).
- 3) S. Ambe, F. Ambe, and N. Saito: IPCR Cyclotron Progr. Rep., 6, 104 (1972).

7-3. A Radiochemical Study of Oxidation States of ^{119}Sb after the EC Decay of $^{119\text{m}}\text{Te}$ in TeO_2 and H_6TeO_6

S. Ambe, F. Ambe, and N. Saito

Although considerable information has already been accumulated concerning the chemical effects of the IT and the β -decay in tellurium compounds, no investigation has ever been reported on the chemical consequences of the EC decay of tellurium. We have now studied the oxidation states of ^{119}Sb (38.0 h) arising from the EC decay of $^{119\text{m}}\text{Te}$ (4.7 days) in tellurium dioxide and telluric acid.

The procedures for producing $^{119\text{m}}\text{Te}$ and for preparing $^{119\text{m}}\text{TeO}_2$ have been described elsewhere.¹⁾ $\text{H}_6^{119\text{m}}\text{TeO}_6$ was prepared by the oxidation of the solid $^{119\text{m}}\text{TeO}_2$ with KMnO_4 in dil. HNO_3 and was recrystallized from dil. HNO_3 , and then from water with the aid of ethanol. The product was dried under a vacuum over P_2O_5 and CaO . The samples were kept at room temperature, 0°C or liquid nitrogen temperature for twelve days or more to allow to decay the ^{119}Sb produced from $^{119\text{m}}\text{Te}$ during the procedure of preparation of the samples.

$^{119\text{m}}\text{TeO}_2$ (3 ~ 10 mg) was dissolved in 6 M HCl containing 3 mg each of Sb(III) and Sb(V) carriers. The solution was immediately diluted to 1.5 M in HCl . $\text{H}_6^{119\text{m}}\text{TeO}_6$ (50 ~ 100 mg) was dissolved in 1.5 M HCl containing the carriers. The ^{119}Sb in the Sb(III) and Sb(V) states was separated by an anion exchange procedure.²⁾ The ^{119}Sb in each fraction was precipitated as Sb_2S_3 from the solutions with H_2S and was collected on a sheet of glass filter paper. The ^{119}Sb -radioactivity (23.8 keV γ -rays and Sn KX -rays) of each fraction was measured by means of a 2-mm NaI scintillation counter connected to a multi-channel pulse-height analyzer.

The results on solid $^{119\text{m}}\text{TeO}_2$ are shown in Table 1. In this compound, ^{119}Sb was found in both the Sb(III) and Sb(V) states, the distribution in the Sb(III) state being slightly higher than that in the Sb(V) state. As can be seen in Table 1, the ^{119}Sb -

Table 1. Oxidation state of ^{119}Sb after the EC decay of $^{119\text{m}}\text{Te}$ in solid TeO_2 and H_6TeO_6 .

Materials	Temperature of storage ($^\circ\text{C}$)	Sb(III) (%)	Sb(V) (%)
TeO_2	-196	59 ± 1	41 ± 1
	23	66 ± 3	34 ± 3
H_6TeO_6	-196	5.0 ± 0.8	95.0 ± 0.8
	0	2.2 ± 0.1	97.8 ± 0.1
	23	1.6 ± 0.2	98.4 ± 0.2

radioactivity in the Sb(III) fraction increased with an increase in the temperature of storage. This observation suggests that the trivalent state is more stable for ^{119}Sb in the solid $^{119\text{m}}\text{TeO}_2$ than is the pentavalent state.

The results on solid $\text{H}_6^{119\text{m}}\text{TeO}_6$ samples are also given in Table 1. In this material, most of the ^{119}Sb was found in the Sb(V) fraction, reflecting the higher oxidation state of $^{119\text{m}}\text{Te}$ in telluric acid. In contrast with the case of TeO_2 , the ^{119}Sb in the Sb(III) fraction showed a significant decrease with an increase in the temperature of storage. It can be concluded, therefore, that the pentavalent state is more stable than the trivalent state for ^{119}Sb in $\text{H}_6^{119\text{m}}\text{TeO}_6$.

In the $\text{H}_6^{119\text{m}}\text{TeO}_6$ samples stored in the form of solutions in water and 1 M KCl without carriers, 30 % and 9 % of ^{119}Sb were found, respectively, in the Sb(III) fraction. The observed values for distribution in Sb(III) are considerably higher than the corresponding values for the $\text{H}_6^{119\text{m}}\text{TeO}_6$ samples stored as a solid. These results can be interpreted on the basis of the absence of the effect of lattice in solutions. The fact that, in a solid, the ^{119}Sb in the Sb(III) state decreases with an increase in the temperature of storage shows that the lattice of telluric acid favors the stabilization of ^{119}Sb in the Sb(V) state, which has an oxidation state closer to the tellurium of the parent compound than does the Sb(III) state. Since there exists no such an effect of lattice in solutions, a greater part of the ^{119}Sb is considered to have been allowed to stabilize in the Sb(III) state.

References

- 1) F. Ambe, S. Ambe, and N. Saito: IPCR Cyclotron Progr. Rep., 6, 102 (1972).
- 2) T. Kambara, K. Hasegawa, and T. Nakamura: Rep. Fac. Sci. Shizuoka Univ., 15, 51 (1970).

7-4. Radiochemical Studies on Carbon, Nitrogen, and Oxygen in Semiconductor Silicon

T. Nozaki, Y. Yatsurugi, and N. Akiyama

By the following three methods, the concentration and behavior of carbon, nitrogen, and oxygen in semiconductor silicon have been studied: (1) charged particle activation analysis, (2) infrared spectrophotometry calibrated by charged particle activation, and (3) a special tracer technique. We have already published some of our results,^{1)~4)} and in this report the works done in 1971 and 1972 are described.

In this period, (1) the precision and accuracy for the activation analysis of the carbon was examined closely in order to obtain more reliable calibration curve for the infrared spectrophotometry of carbon in silicon, and (2) the solubilities of nitrogen and oxygen in solid and liquid silicon at its melting point were determined with more accuracy. The infrared calibration curve for carbon in silicon is given in a separate paper,⁵⁾ together with its validity range, precision, accuracy and some remarks necessary in the practical infrared determination. Table 1 shows the solubilities for carbon, nitrogen, and oxygen as well as their equilibrium distribution coefficients between solid and liquid silicon and their atomic dimensions. Figures 1 and 2 show the phase diagrams for N-Si and O-Si systems in extremely low nitrogen or oxygen concentration ranges. Detailed description about these data together with thermodynamical discussions on them will be published in near future.⁶⁾

Table 1. Solubilities and equilibrium distribution coefficients of carbon, nitrogen, and oxygen in silicon at its melting point and their atomic radii and tetrahedral radii.

	Carbon	Nitrogen	Oxygen
Solubility in solid			
(at./cm ³)	$(3.2 \pm 0.3) \times 10^{17}$	$(4.5 \pm 1.0) \times 10^{15}$	$(2.75 \pm 0.15) \times 10^{18}$
(atomic fraction)	$(6.5 \pm 0.5) \times 10^{-6}$	$(9 \pm 2) \times 10^{-8}$	$(5.6 \pm 0.3) \times 10^{-5}$
Solubility in liquid			
(at./cm ³)	$(4.5 \pm 0.5) \times 10^{18}$	7×10^{18}	$(2.20 \pm 0.15) \times 10^{18}$
(atomic fraction)	$(9 \pm 1) \times 10^{-5}$	1.2×10^{-4}	$(4.5 \pm 0.3) \times 10^{-5}$
Equilibrium distribution coefficient	0.07 ± 0.01	7×10^{-4}	1.25 ± 0.15
Atomic radius (A)	0.77	0.53	0.60
Tetrahedral radius (A)	0.77	0.70	0.66

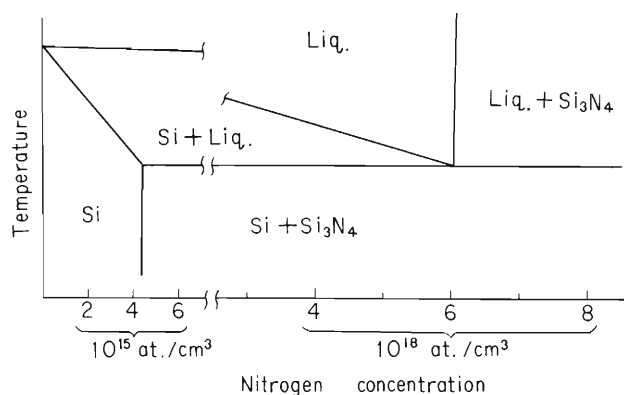


Fig. 1. Phase diagram of N-Si system in extremely low nitrogen concentrations.

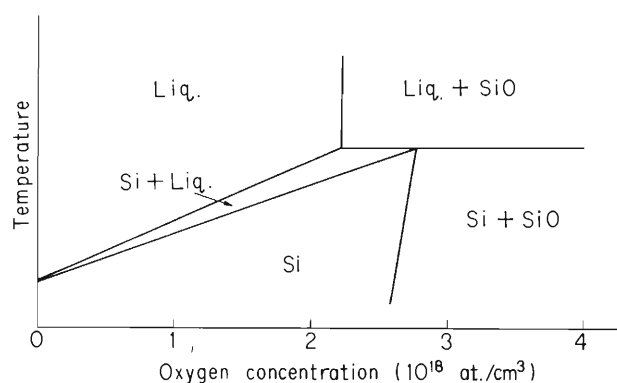


Fig. 2. Phase diagram of O-Si system in extremely low oxygen concentrations.

Studies on the following subjects are either under way or under planning: (1) infrared spectrophotometry for oxygen in silicon as calibrated by charged particle activation, (2) relationship between the carbon monoxide content of the ambient and the concentrations of carbon and oxygen in molten silicon, and (3) effects of carbon in semiconductor silicon on its electrical properties.

References

- 1) T. Nozaki, Y. Yatsurugi, and N. Akiyama: *J. Radioanal. Chem.*, **4**, 87 (1970).
- 2) T. Nozaki, Y. Yatsurugi, and N. Akiyama: *J. Electrochem. Soc.*, **117**, 1566 (1970).
- 3) T. Nozaki, Y. Makide, Y. Yatsurugi, N. Akiyama, and Y. Endo: *Intern. J. Appl. Radiat. Isotopes*, **22**, 602 (1971).
- 4) T. Nozaki, Y. Makide, Y. Yatsurugi, Y. Endo, and N. Akiyama: *Bull. Chem. Soc. Japan*, **45**, 2776 (1972).
- 5) Y. Endo, Y. Yatsurugi, N. Akiyama, and T. Nozaki: *Anal. Chem.*, **44**, 2258 (1972).
- 6) Y. Yatsurugi, N. Akiyama, Y. Endo, and T. Nozaki: Submitted for publication in *J. Electrochem. Soc.*

8. RADIATION CHEMISTRY AND RADIATION BIOLOGY

8-1. Radiolysis of Binary Mixtures of Tetrahydrofuran and Benzene in High LET Region

M. Matsui, T. Karasawa, and M. Imamura

Binary mixtures of tetrahydrofuran (THF) and benzene were subjected to radiolyses with 20 MeV ^4He - and 80 MeV ^{14}N -ions. Variations of the yield of hydrogen, a major radiolysis product, in the ^4He -ion and ^{14}N -ion radiolyses are shown in Figs. 1 and 2, respectively, as a function of the electron fraction of benzene. The general patterns are similar to that observed in γ -radiolysis shown in Fig. 3,¹⁾ i.e., an energy transfer from the precursor of hydrogen to benzene seems to take place, resulting in the reduction of the yields from those expected in the absence of any interaction between the two components. (These expected values are to be on the lines connecting G-values of pure THF and benzene as shown in Figs. 1, 2, and 3)

A previous study²⁾ on γ -radiolysis of a binary system of THF and furan also exhibited the similar behavior, and it was concluded that the charge transfer from THF^+ , the precursor of hydrogen, to furan does take place.

In the present THF-benzene system, it can also be assumed that the precursor of hydrogen is THF^+ and the charge transfer to benzene would take place to reduce the yields of hydrogen. The experimental results supporting this assumption are described below.

First, the yields of hydrogen in γ -radiolysis of pure THF are not affected in the presence of radical scavengers, indicating that the precursor should be ionic or excited species. Second, carbon monoxide, the yields of which are not affected by radical scavengers, was concluded to be formed predominantly from excited species,²⁾ and its yields in the THF-benzene and THF-furan²⁾ systems do not show any deviation from linearity unlike those of hydrogen. Finally, the behavior of $G(\text{H}_2)$ is quite similar to that observed for the THF-furan system as mentioned above.

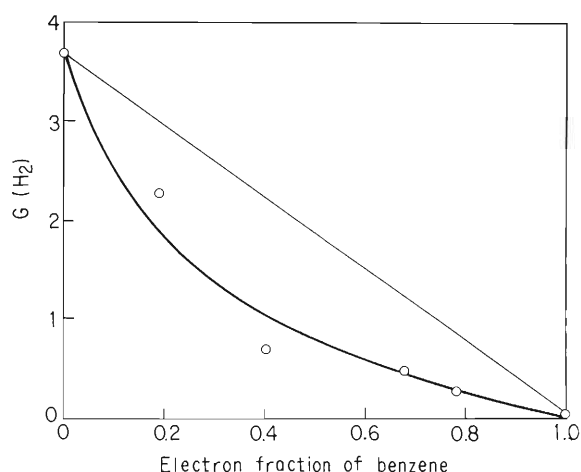


Fig. 1. Variation of $G(\text{H}_2)$ with electron fraction of benzene in ^4He -ion radiolysis.

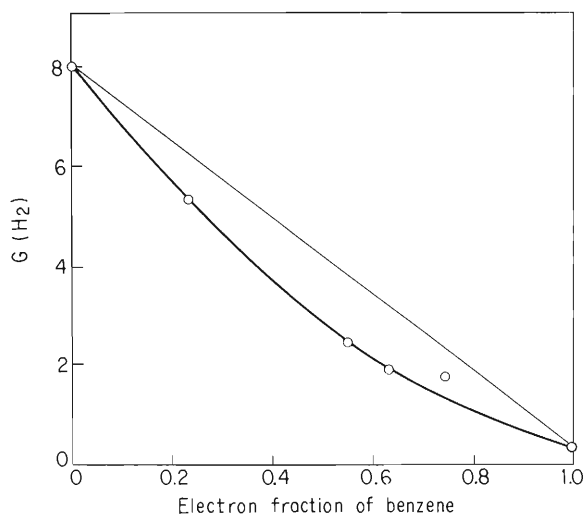


Fig. 2. Variation of $G(\text{H}_2)$ with electron fraction of benzene in ^{14}N -ion radiolysis.

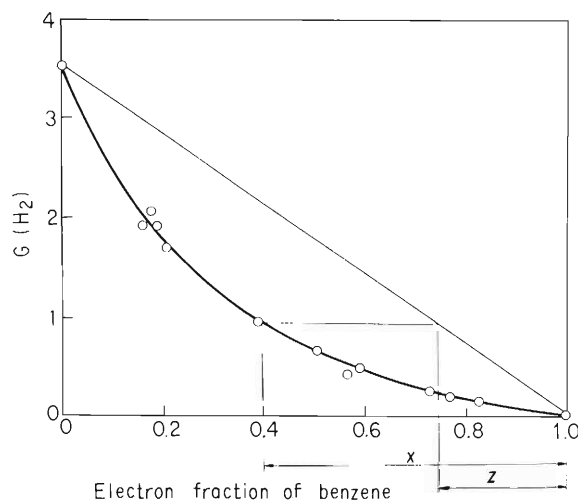


Fig. 3. Variation of $G(H_2)$ with electron fraction of benzene in γ -radiolysis.

According to Hardwick,³⁾ let x be the electron fraction of THF, and let z be the apparent electron fraction of THF as indicated by the measured value of $G(H_2)$ (Cf. Fig. 3), then the amount of THF which transfers energy is $(1-z) - (1-x) = x - z$. The fraction of THF molecules absorbing energy, and which subsequently transfer this energy, is $(x - z)/x$. The limiting values of $(x - z)/x$ and the decreasing hydrogen yield, $\Delta G(H_2)$, at the higher concentration region of benzene for γ , ^4He , and ^{14}N radiolyses are listed in Table 1.

Table 1. Yields of total ionization of THF obtained for the radiolyses of THF-benzene mixtures with γ , ^4He , and ^{14}N .

Radiation	Mean LET (eV/Å)	$\Delta G(H_2)$	Limiting ($x-z$)/ x	$G(\text{total ionization})$
γ	0.02	2.2	0.70	3.1
^4He	6.5~7.0	2.4	0.75	3.2
^{14}N	43	2.0	0.65	3.1

Using these values and assuming that all the hydrogen is produced from THF^+ , one can estimate the yields of total ionization of THF as listed also in Table 1. These results imply that $G(\text{total ionization})$ is invariant irrespective of the nature of radiations or LET. Large increases of $G(H_2)$ which are generally observed for radiolyses of liquid organic compounds in a high LET region may therefore be not ascribed to the increasing ionization resulting from charge exchange, energetic secondary electron production or other events by heavy ions.

References

- 1) M. Matsui: Bull. Chem. Soc. Japan, 39, 1640 (1966).
- 2) M. Matsui and M. Imamura: Abst. 12th Conf. Radiat. Chem., Nagoya, p. 57 (1969).
- 3) T. J. Hardwick: J. Phys. Chem., 66, 2132 (1962).

8-2. LET Dependence of Spatial Distribution of Free Radicals in Irradiated Crystalline Eicosane

K. Kimura, M. Kikuchi,* M. Matsui, T. Karasawa,
M. Imamura, Y. Tabata,* and K. Oshima*

Electron spin resonance studies have been made on the spatial distribution and its dependence on linear energy transfer of free radicals produced and trapped in a crystalline n-eicosane ($C_{20}H_{42}$).

Only a few studies have been reported so far on the similar subject with amino acids¹⁾ and other solids,²⁾ and no substantial differences in the spatial distribution of free radicals due to LET have been found.

Sliced single crystals ($45 \times 45 \times 1$ mm) were subjected to irradiations with 23.3 MeV ^4He , 85 MeV ^{12}C , and 81.5 MeV ^{14}N ions at low temperatures in the vicinity of 80 °K. Irradiations were also carried out using ^{60}Co γ -rays for comparison. ESR measurements were done employing 100 kHz frequency modulation at several temperatures between 77 and 250°K. Upon γ -irradiation, the single crystal of n-eicosane gave ESR spectra having well-separated and sharp hyperfine structures which can be attributed to alkyl radicals in the weak spin-spin interactions.

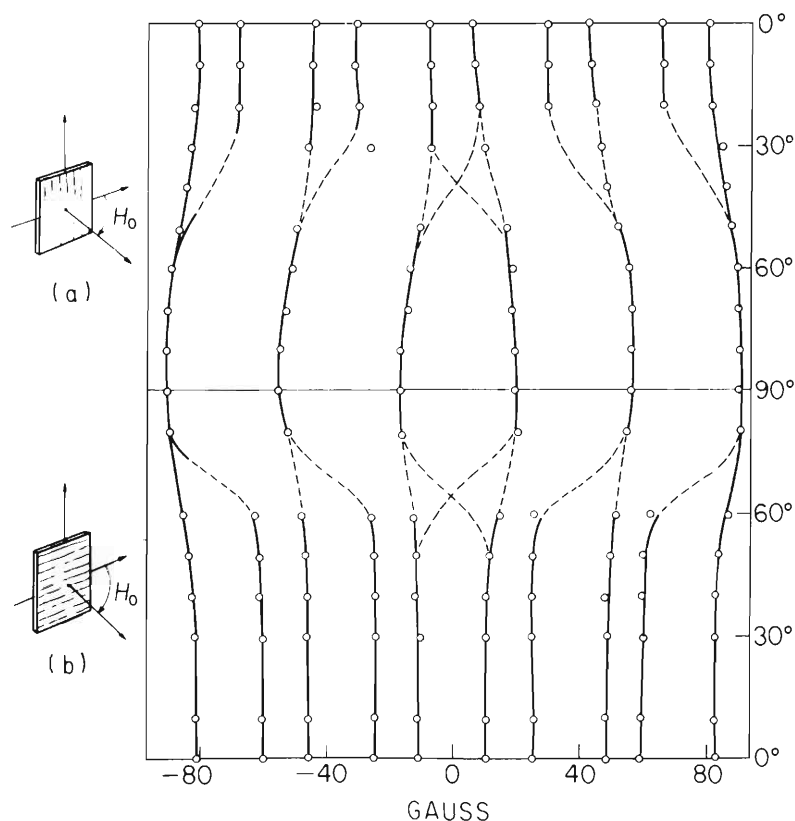


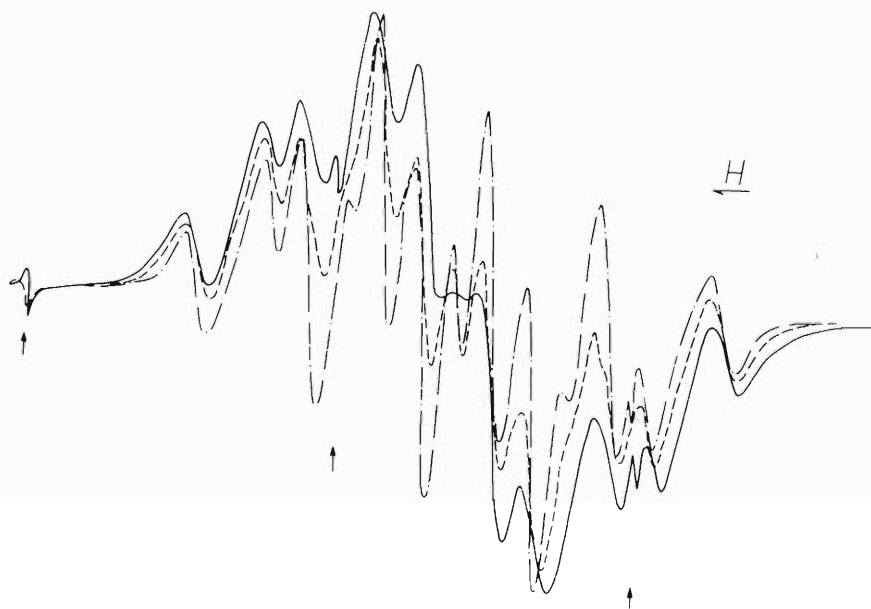
Fig. 1. Variations of hf coupling constants with angles of static field E_0 to the surface of n-eicosane.

* Department of Nuclear Engineering, University of Tokyo.

Figure 1 shows variations of hf coupling constants of alkyl radicals with angles (θ) of static field H_0 to the crystal surface for two cases (a) and (b): (a), H_0 is fixed perpendicular to a crystal axis of growth and (b), H_0 is at variable angles to this axis. When H_0 intersects with the surface at a right angle, six lines are assignable to five equivalent α and β protons of a coupling constant of 34.8 gauss; when H_0 makes an angle of 0° with the surface and 90° with the axis (case a), ten lines to one α proton of $A_\alpha^{\text{iso}} = -22.4$ and $A_\alpha^{\text{dipol}} = 8.9$ gauss and four equivalent β protons of $A_\beta^{\text{iso}} = 34.8$ gauss; when H_0 makes an angles of 0° with both the surface and axis (case b), ten lines to one α proton of $A_\alpha^{\text{iso}} = -22.4$ and $A_\alpha^{\text{dipol}} = 1.2$ gauss and four equivalent β protons of $A_\beta^{\text{iso}} = 34.8$ gauss.

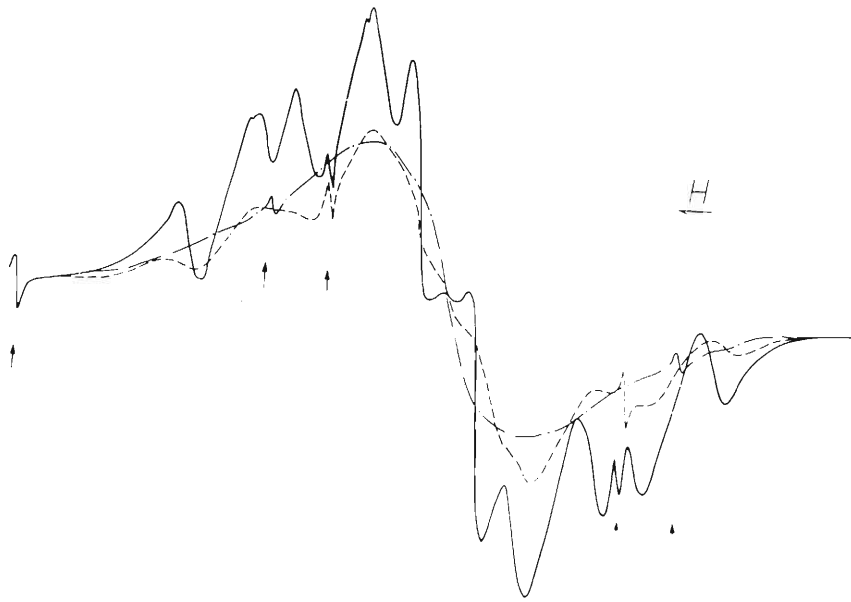
In Fig. 2 are shown the spectra recorded at 77°K for samples irradiated with ^4He and ^{12}C ions as well as with γ -rays (case b, $\theta = 0^\circ$). Apparently, linewidths of the spectra decrease on going from γ to ^{12}C -ion irradiation. There exists an relatively strong dose effect on the lineshape and linewidth as shown in Fig. 3. Therefore, absorbed doses in the present study were chosen to be so low as not to give rise to the overlapping of ionization tracks.

A variation of the ESR spectra with temperature is shown in Fig. 4, in which spectra were recorded at 77, 116, and 198°K for a sample irradiated with ^{12}C ions at 80°K (case b, $\theta = 0^\circ$). It is apparent from Fig. 4 that as a temperature of the sample is increased the intensity of the spectrum decreases, while its sharpness increases; the spectrum recorded at 198°K seems similar to that obtained by γ -irradiation and recorded at 77°K.

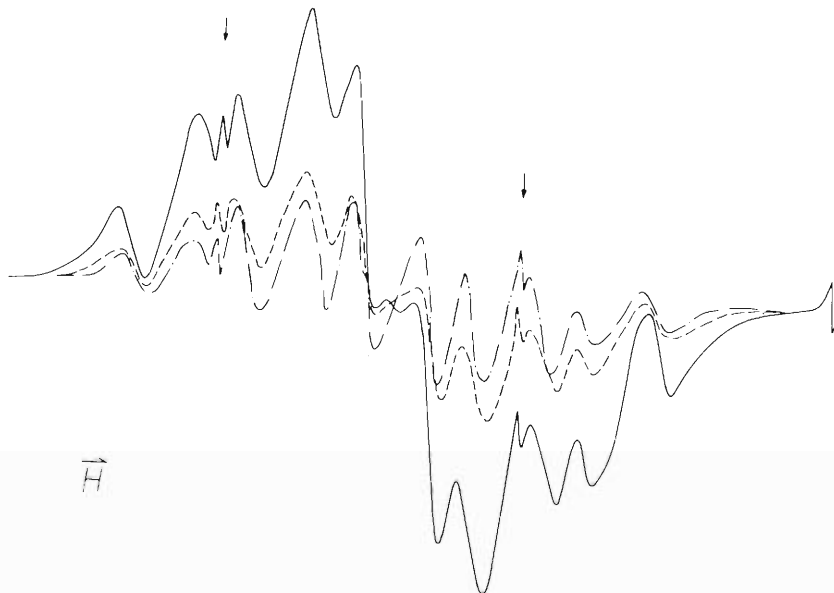


Irradiated with γ (- · - ·), ^4He (- · - -), and ^{12}C (—).
Dose: 1.68×10^{21} eV for γ ; 2.3×10^{19} eV for ^4He ; 2.7×10^{19} eV for ^{12}C . Spectra recorded at 77 °K. Case b, $\theta = 0^\circ$. Absorption lines due to Mn^{2+} are indicated by arrows.

Fig. 2. ESR spectra of irradiated n-eicosane.



Spectra recorded at 77 °K. Case b, $\theta = 0^\circ$. Dose: —, 2.7×10^{19} eV; ----, 1×10^{20} eV; - · - ·, 4.3×10^{21} eV.
 Fig. 3. Variations of ESR spectra with radiation dose.
 Irradiated with ^{12}C .



Irradiated with ^{12}C to a dose of 2.7×10^{19} eV.
 Temperature: —, 77 °K; ----, 116 °K; - · - ·, 198 °K.
 Fig. 4. Variations of ESR spectra with increasing temperature.

Such a variation of spectra is not due to a motional narrowing because no reversible variation of spectra was observed even if the sample was cooled back to lower temperatures. Therefore, the spectrum disappearing by increasing temperature is only a component having broad linewidths. In fact, by subtracting the spectrum observed at 116 or 198°K from that at 77°K, one can obtain a broad spectrum similar to that obtained with the sample irradiated to a high dose.

From these experimental results, it may be concluded that the ESR spectra of ^{12}C or ^{14}N ion-irradiated samples recorded at 77°K are superimpositions of components having broad and sharp linewidth. The broad one is regarded as being due to a strong spin-spin interaction between closely distributed radicals. These radicals readily combine with each other as the temperature is increased, resulting in the disappearance of the broad component of the spectrum. The sharp component may therefore be considered to be due to sparsely distributed radicals, which is a principal mode in the γ -irradiation.

Preliminary estimate has been made of the relative number of radicals distributed densely and sparsely. More quantitative studies are in progress.

References

- 1) T. Henriksen, P. K. Horan, and W. Snipes: *Radiat. Res.*, 43, 1 (1970).
- 2) Yu. D. Tsvetkov and A. M. Raitsimring: *Radiat. Effects*, 3, 61 (1970).

8-3. LET Effects on Bacterial Cells

A. Matsuyama, T. Takahashi, T. Karasawa, K. Igarashi,
F. Yatagai, and Y. Kitajima

(1) Determinations of LET effects on cellular radiosensitivities of bacteria

Log-phase cells of *E. coli* B_{S-1} and spores of a thymine requiring mutant of *B. subtilis* 168 were irradiated with charged particles such as α -particles, carbon-, nitrogen-, and oxygen-ions to determine the LET dependence on radiosensitivity of these bacterial cells. As previously described,¹⁾ bacterial cells spread on a membrane filter (Millipore filter type HA) which was placed on a wet pad were exposed to ion beams in air. Using a biological irradiation unit, the sample was swung vertically and horizontally in a plane perpendicular to the beam over a square area of 24 × 24 mm during irradiation for the dose uniformity. Since the faster rate of the swinging cycle was employed, a variance of survival data which might be due to the fluctuation of beam intensity was reduced.

The results obtained are shown in Figs. 1~4. All survival curves were of an exponential type. With respect to LET dependence on cellular radiosensitivity, it should be noted that values of radiosensitivity, $1/D_{37}$, simply decreased with increasing total LET in the case of *E. coli* B_{S-1} (Fig. 2), while those of *B. subtilis* spores revealed a maximum at about 12 eV/Å of total LET, followed by the decrease in higher regions (Fig. 4). In the latter case (*B. subtilis* spores), where the shape of survival curves indicates the one-hit type, the increase in cellular radiosensitivity with increasing LET in the region of the LET less than 12 eV/Å suggests that one effective lethal hit requires multiple events as charged particles traverse the target in a spore. It must be pointed out as a pregnant fact that, in Fig. 3 illustrating a relationship between the energy of charged particles and inactivation cross section for spores, there can be seen a significant shift of the effective cross section (S_{eff}) for nitrogen ions ($0.17 \mu^2$) from the maximum plateau of S_{eff} for α -particles ($0.13 \mu^2$) in the low-energy region (less than about 1 MeV/amu). Because biological effects in these low energy region do not or hardly involve those due to δ -rays, this shift may suggest an additional possibility of spore inactivation due to the smaller targets other than DNA molecule or spore-specific conformation of DNA. Further investigations are now undertaken in this laboratory to elucidate this problem.

(2) Analysis on the inactivation model for *E. coli* B_{S-1}

Since survival curves of *E. coli* B_{S-1} were of the exponential type, from the viewpoint of one-hit model in the target theory, the relationship between S_{eff} and LET can be simplified as follows:

$$S_{\text{eff}} = S_0 \left\{ 1 - \exp(-k \cdot L) \right\} \quad (1)$$

where S_0 is the geometrical cross section, L the total LET, k a constant. As seen in Fig. 5, theoretical curve (1) indicates a good agreement with experimental one, and using the least-squares method (Grid search method), parameters S_0 and k are determined as follows:

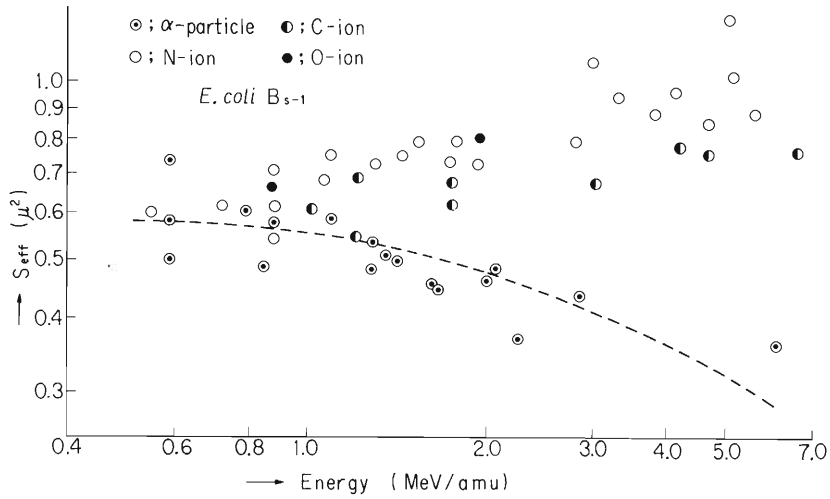


Fig. 1. Effective inactivation cross section (S_{eff}) of E. coli B_{S-1} as a function of energy per nucleon (MeV/amu).

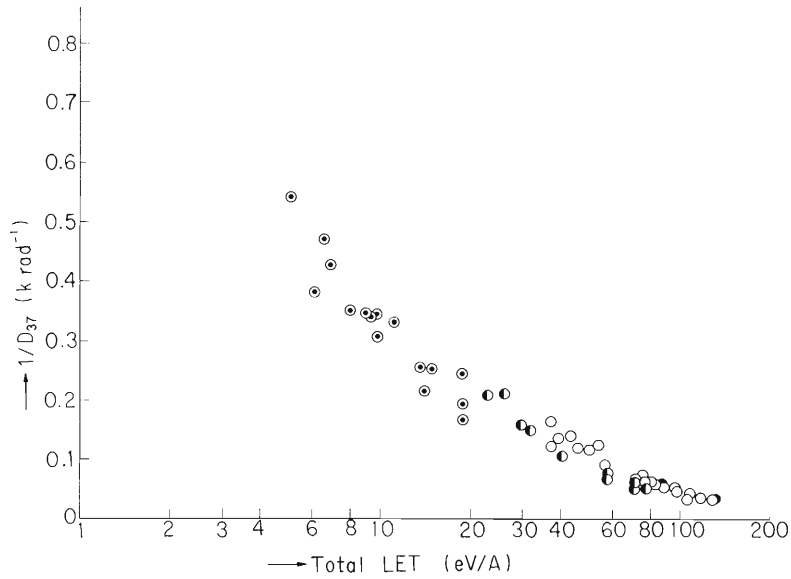


Fig. 2. Radiosensitivity ($1/D_{37}$) of E. coli B_{S-1} as a function of total LET.

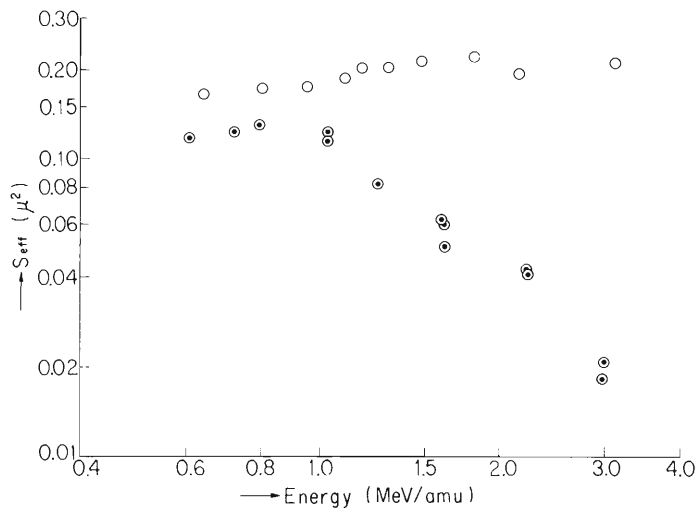


Fig. 3. Effective inactivation cross section (S_{eff}) of B. subtilis 168 thy⁻ind⁻leu⁻ (MY2Y1U2) spores as a function of energy per nucleon (MeV/amu).

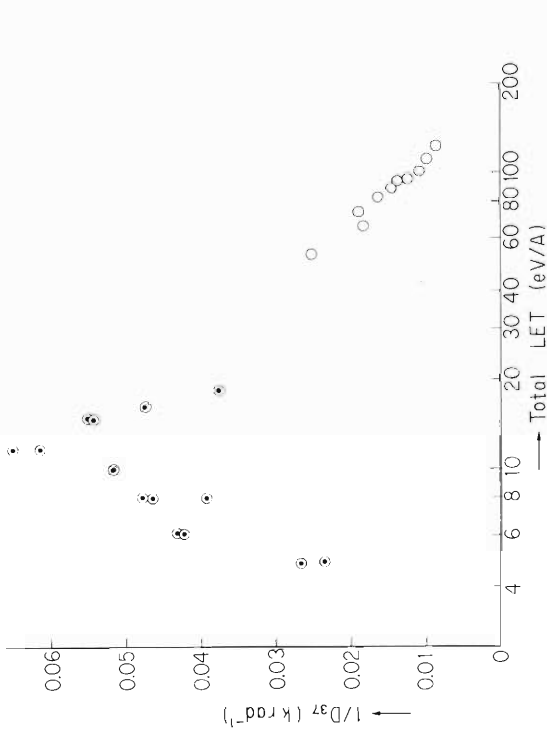


Fig. 4. Radiosensitivity ($1/D_{37}$) of *B. subtilis* 168 thy^- and leu^- (MY2Y IU2) spores as a function of total LET.

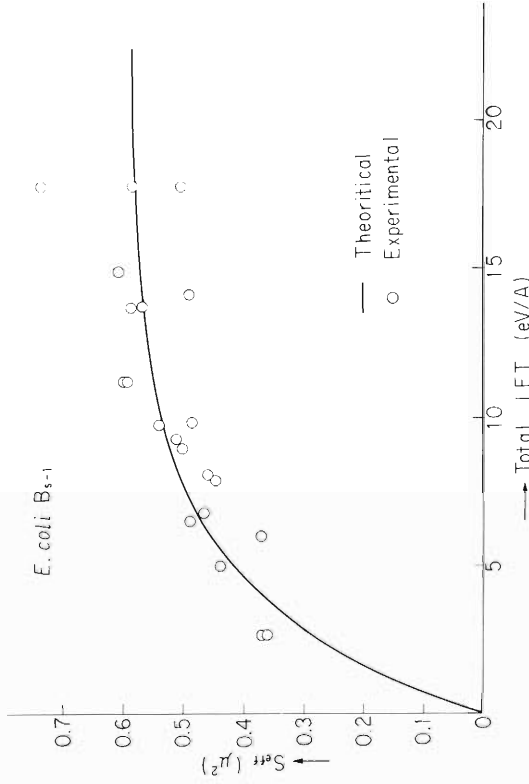


Fig. 5. Relationship between effective inactivation cross section of *E. coli* B₅₋₁ and total LET.

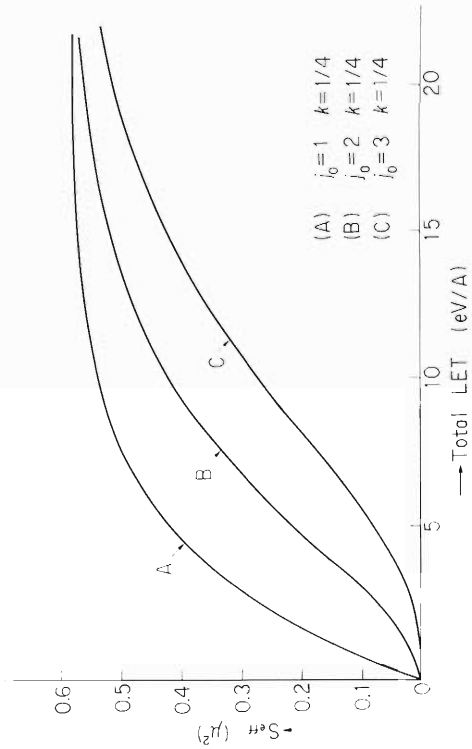


Fig. 6. S_{eff} - total LET curve calculated by equation (3).

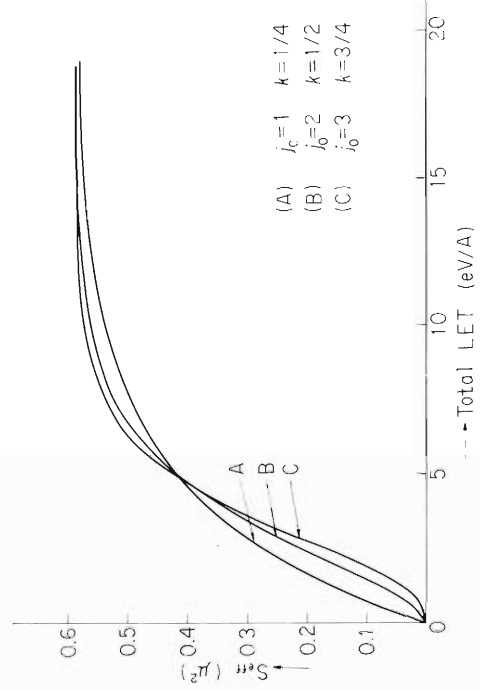


Fig. 7. S_{eff} - total LET curve calculated by equation (4).

$$S_0 = 0.585 \pm 0.0697 \quad (\mu^2)$$

$$k = 0.249 \pm 0.0488$$

The value of S_0 , $0.59 \mu^2$, is appreciably smaller than the geometrical cross section S_0 , $1.1 \mu^2$, estimated from the electron micrograph, and this fact may suggest that S_{eff} is implicated with the repair ability for radiation damages in the target. If the DNA in a cell is the target molecule, more explicit description (2) on the inactivation mechanism is obtained by introducing the "microdose concept" to the target theory.

$$S_{\text{eff}} = S_0 \left(1 - \sum_{j=0}^{j_0-1} f_j \right)$$

$$f_j = (\ell/W \cdot L)^j / j! \exp(-\ell/W \cdot L) \quad (2)$$

where f_j is the probability that a track gives j primary events, j_0 the minimum number of primary events required for one decisive event in a target,* W the mean energy per primary event. ℓ is the mean thickness of the target and consequently $(\ell/W \cdot L)$ is the mean number of primary events occurred along a track. In the case of $j_0 = 1$ and $k = \ell/W$, formula (2) is consistent with formula (1). Therefore, by applying formula (2) to the experimental results, two different inactivation models can be suggested, which define the repair ability factor $(1 - P)$ with different ways. P is the probability of the unrepaired radiation damage, where the whole damage is normalized to 1.

In the first inactivation model, on the assumption that the whole DNA (the geometrical cross section of which = S'_0) in a cell is the target, P could be defined as follows:

$$P = (S_0/S'_0)^{3/2} \quad (3)$$

Three different calculated curves are shown in Fig. 6. The curve A indicates the best fit for the experimental data. If curve A is adopted, the experimental results give $P = 0.39$ and $W = 170$ eV.

In the second model, hypothesizing that more small unit of DNA (the geometrical cross section of which = S_0) in the cell is the target, P could be defined as follows:

$$P = (W_s/W_g) \quad (4)$$

where W_s is the energy required for producing a single-strand break in DNA and W_g the gamma energy absorbed in DNA of a cell irradiated with a dose specified by D_{37} . Three different cases are shown in Fig. 7. If curve A is adopted, the experimental results give $\ell = 6.4 \text{ \AA}$. In the first model, it is not clear what is a decisive event in a target and in the second model, the value of ℓ (6.4 \AA) appears too small to compare it with the size of DNA strands. However, the possible contribution of any other targets besides DNA should be taken into consideration for establishing the most plausible inactivation model.

* In general, primary ionization and excitation may be considered as primary events, and if single- or double-strand breaks in DNA remain irreparable, they are referred to as decisive events.

(3) Sedimentation analysis on DNA of E. coli B_S-1

In order to determine the LET dependence on a ratio of single breaks to double break in bacterial DNA and a rate of the DNA repair, log-phase cells of E. coli B_S-1 and M. radiodurans labeled with ³H-thymidine in advance have been irradiated with different types and energies of charged particles, and subjected to the sedimentation analysis before and after the postirradiation incubation. Although determinations have not yet been completed, it has been observed that the rate of the DNA repair at high LET (44 MeV nitrogen ions) was appreciably reduced even in a radioresistant bacterium M. radiodurans.

Reference

- 1) A. Matsuyama, T. Karasawa, S. Kitayama, and R. Takeshita: IPCR Cyclotron Progr. Rep., 3, 101 (1969).

9. SOLID STATE PHYSICS

9-1. Positron Annihilation in Ferromagnetic Nickel

N. Shiotani, T. Okada, H. Sekizawa,
T. Mizoguchi, and T. Karasawa

Positron annihilation in ferromagnetic nickel single crystals has been studied. About 500 mCi ^{90}Nb positron sources were obtained by irradiation of Zr targets in the cyclotron. The detailed experimental procedure was described by the authors.^{1), 2)}

Figure 1 shows the observed angular correlation curves for the $[100]$ orientation and for the $[110]$ orientation, respectively. The curves marked Field-2 were obtained under the condition that the direction of the magnetization of the specimen was parallel to the direction of the polarization of the positron spins. The curves marked Field-1 were obtained by reversing the direction of the magnetization of the specimen. The curves are normalized to give an equal area.

The smoothed curves drawn through the experimental points were obtained by evaluating at θ_i the least-squares polynomial of degree 3 relevant to the five successive points $[N(\theta_{i+k}), \theta_{i+k}, k = -2; -1, \dots, 2]$.

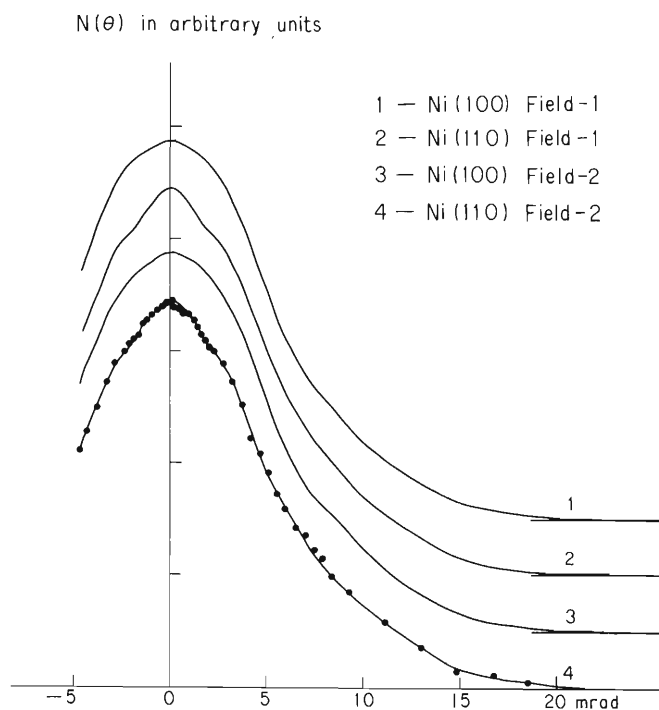


Fig. 1. The angular correlation curves for (100) and (110) nickel crystals.

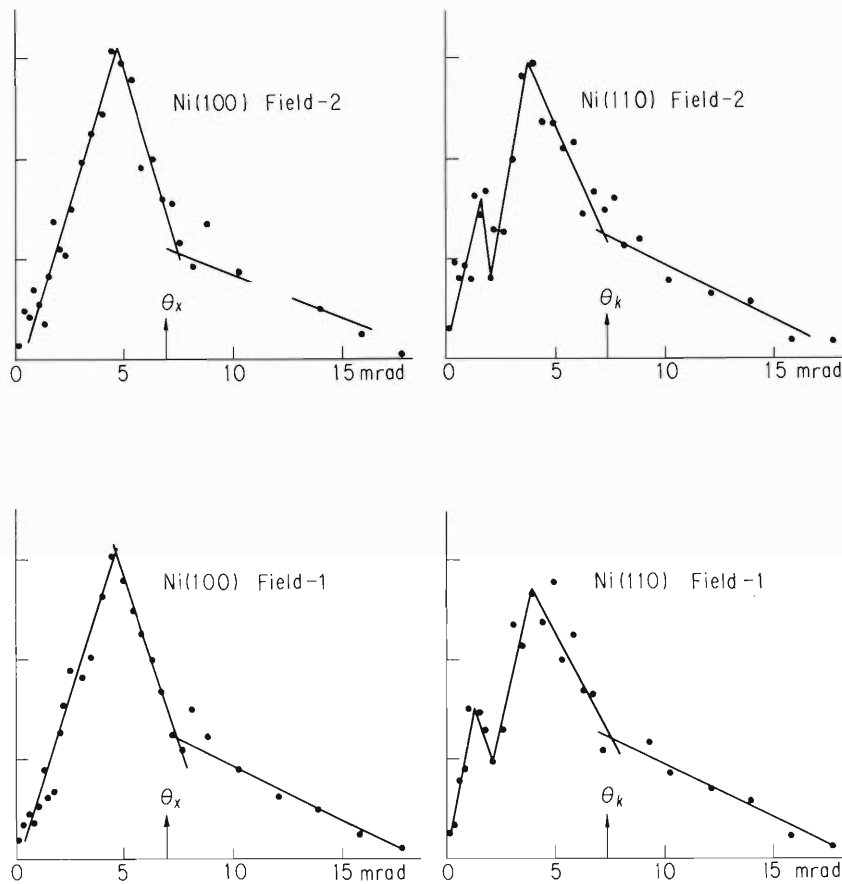


Fig. 2. "Differentiated curves" obtained by differentiating the angular correlation curves shown in Fig. 1.

In order to find some characteristics of the angular correlation curves, the smoothed curves are numerically differentiated. The differentiated curves are shown in Fig. 2.

The statistical error of each point on the smoothed curves is about 0.7 % and is not small enough to be used to see the effect of reversing the direction of magnetization of the specimen. Therefore, the sectional area under the smoothed curve is calculated at an interval of about one milliradian and from this area an averaged value of $N(\theta)$, θ being taken as the middle point of the interval, is determined. The differences at each θ by reversing the direction of magnetization are plotted in Fig. 3.

The observed features of the correlation curves can be interpreted qualitatively on the basis of the energy band structures in the ferromagnetic nickel calculated by Connolly.²⁾ The detailed report will be published elsewhere shortly.

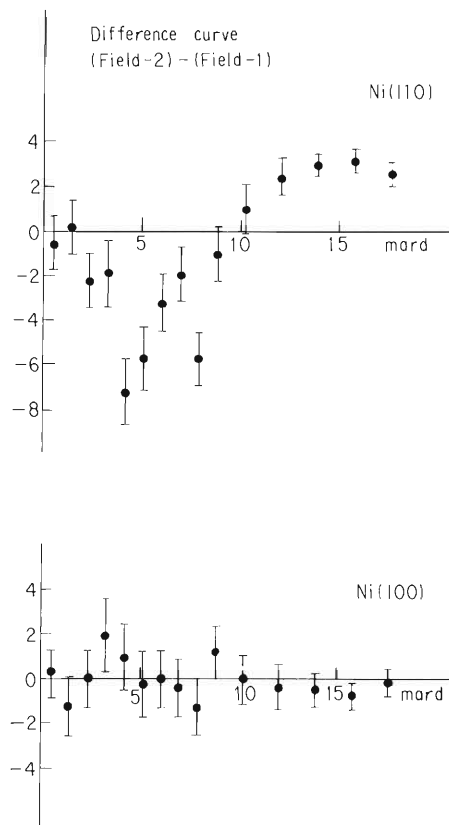


Fig. 3. "Difference curves" showing the change of the correlation curves on reversal of the applied magnetic field.

References

- 1) N. Shiotani, S. Ambe, T. Okada, and T. Karasawa: *Japan. J. Appl. Phys.*, 11, 412 (1972).
- 2) N. Shiotani, T. Okada, H. Sekizawa, S. Ambe, T. Mizoguchi, and T. Karasawa; *IPCR Cyclotron Prog. Rep.* 5, 105 (1971).
- 3) J. W. Connolly: *Phys. Rev.*, 159, 415 (1967).

9-2. Point Defects in Irradiated Copper and Cu₃Au

H. Sakairi, E. Yagi, A. Koyama,
T. Karasawa, and R.R. Hasiguti

The increased resistivity of irradiated f.c.c. metals shows distinctive recovery below 50K (stage I), then decreases gradually over a wide range of temperature (stage II) and shows again a fast decay near room temperature (stage III). The assignment of point defects behavior to each stage is a difficult problem and has given rise to a variety of interpretations for about 20 years.

The irradiation study of an ordered Cu₃Au alloy and a pure copper is being performed in this laboratory.¹⁾ The use of ordered alloys is expected to give additional information which cannot be obtained by the studies of pure metals, because the physical properties of ordered alloys are changed drastically by the change of the degree of order induced by atomic exchange replacements, while those of pure metals are not affected by atomic replacements.

(1) Stage III annealing

A decay of the resistivity of Cu is caused by a decrease of the number of defects, while that of Cu₃Au by a decrease of the number of wrongly sited atoms. As the ordering replacements of atoms are caused by the defect migration, the decreasing rate of wrongly sited atoms is determined by a number of visits of defects to them, which is in proportion to the concentration of migrating defects (n), the number of jumps of them (j), and the concentration of wrongly sited atoms (D). Thus the rate equation of the stage III annealing of Cu₃Au is written as

$$\frac{dD}{dt} = -njD.$$

As for n , its decay is caused by the recombination annihilation of interstitial atoms and vacancies, in which the number of migrating defects always equals to that of the waiting counterparts (though it is not certain which are migrating in this stage), so that the decay rate of the concentration of them obeys the 2nd order reaction kinetics as

$$\frac{dn}{dt} = -n^2jg,$$

where g is the number of effective sink sites around waiting defects. From these equations it can be derived that

$$n/n_0 = (D/D_0)^g.$$

In the irradiation experiments of aluminum a radius of sinks acting in the stage III annealing was estimated to be around 2 atomic diameters,²⁾ from which the value of g is deduced to be about 30.

The curves of n presented in Fig. 1 were calculated with this equation and the experimentally obtained curve of D .¹⁾ It can be fitted to the experimentally obtained one for pure copper by taking g to be about 20, which is close to the above referred value.

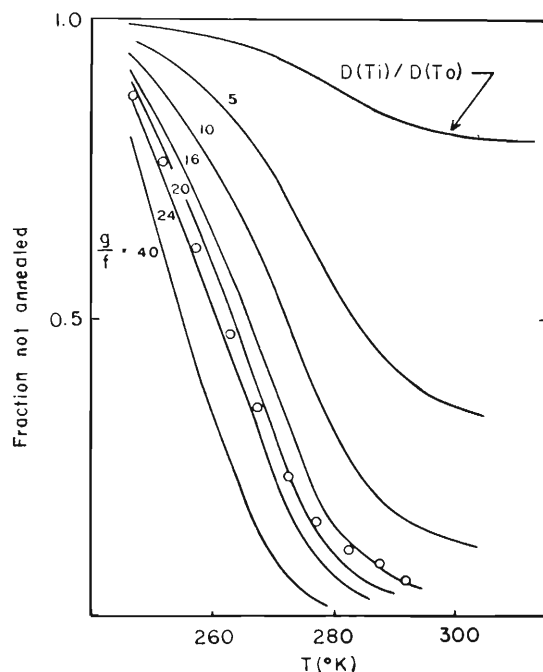


Fig. 1. Isochronal annealing curves of defect concentration in Cu_3Au calculated from the isochronal annealing curve of the concentration of wrongly sited atoms. (Open circles indicate the values obtained experimentally for Stage III defects in copper.¹⁾)

The analysis mentioned here shows that the ability of thermal migration of the defects responsible to the stage III of the alloy is nearly the same as that of the stage III defects in pure copper, in spite of an apparent discrepancy between the stage temperatures of the alloy and the pure copper.

(2) Stage I annealing

The annealing characteristics of the alloy between liquid helium and liquid nitrogen temperatures were found to be different greatly from those of pure copper. Isochronal annealing curves of them are shown in Fig. 2.

A notable difference between the alloy and copper appears as the reverse annealing below 50K in the heavily irradiated alloy. An extent of reverse annealing is, however, almost cancelled by the following normal annealing up to liquid nitrogen temperature, so that the total amount of recovery between these temperatures is almost independent of the irradiation dose. It is obviously the result of this cancelling effect that the damage introduction rate at liquid helium temperature is larger by only about 30 % than that at liquid nitrogen temperature, as was reported previously.³⁾

At present it is difficult to determine which of the reverse and normal annealing stages of the alloy corresponds to the defect migration occurring in the stage I of pure copper. Moreover, the fine structures of the annealing curve of the alloy bring about further difficulty in the interpretation of the stage.

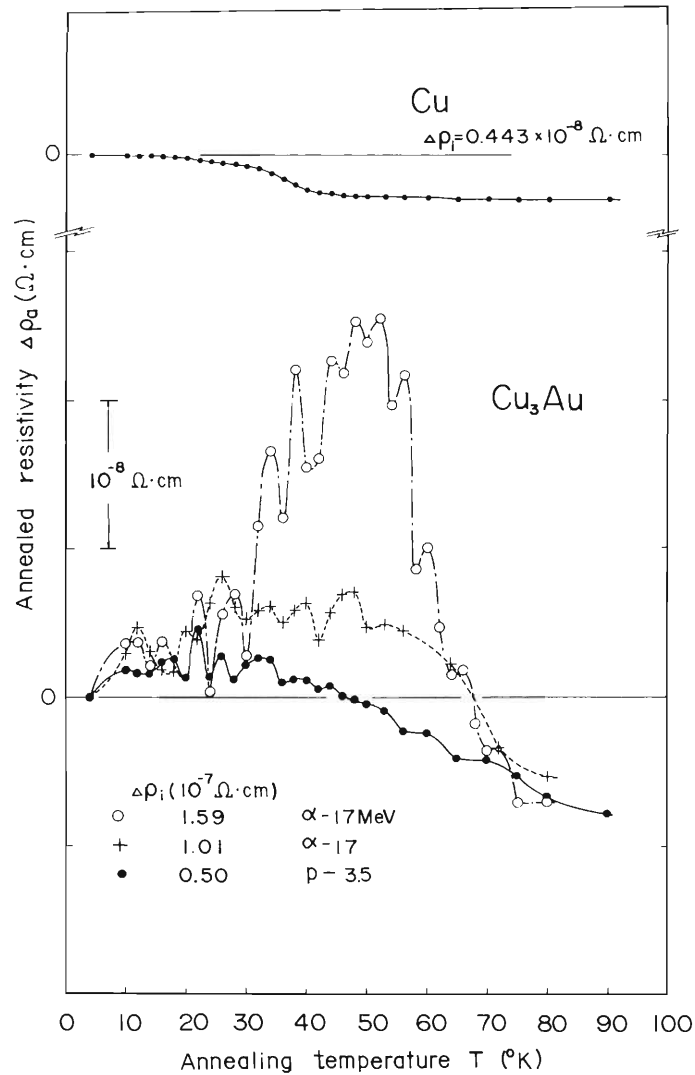


Fig. 2. Stage I annealing of Cu₃Au and Cu irradiated with alpha-particles or protons at liquid helium temperature. Annealing time at each temperature is 5 min. ($\Delta\rho_i$ is a total increase of resistivity by the irradiation.)

References

- 1) H. Sakairi, E. Yagi, T. Karasawa, and R.R. Hasiguti: IPCR Cyclotron Progr. Rep., 4, 140 (1970).
- 2) W. Schilling, G. Burger, K. Isebeck, and H. Wenzl: Vacancies and Interstitials in Metals, (ed. A. Seeger et al.) North-Holland, Amsterdam, p. 255 (1970).
- 3) H. Sakairi, E. Yagi, A. Koyama, T. Karasawa, and R.R. Hasiguti: IPCR Cyclotron Progr. Rep., 5, 101 (1971).

9-3. Electron Microscopic Observation on Helium Bubbles in Aluminum Irradiated by Alpha-Particles

H. Sakairi, E. Yagi, H. Shiraishi,
T. Karasawa, and R.R. Hasiguti

Helium bubbles generated in pure aluminum irradiated by alpha particles have been observed by transmission electron microscopy. The aim is to investigate the relation between the bubbles and various lattice imperfections.

Examples of bubbles generated on dislocations or at grain boundaries were observed and already reported.^{1), 2)} It is certain that helium atoms precipitate preferentially on such imperfections. It was, however, suggested that the interaction between bubbles and dislocations is rather weak so that the dislocations can be released easily from the trapping by bubbles during thermal annealing.

Subsequently an example of the bubble-boundary interaction was observed in a specimen which was deformed after injection of He. As shown in Fig. 1, a grain boundary migrating for recrystallization is bent by pinning action of bubbles. The calculation by Speight and Greenwood³⁾ predicted that small bubbles are swept up by the migrating boundary while large bubbles are left behind it. Condition of the bubble sweeping was determined in terms of radius of bubbles and distance between them as illustrated in Fig. 2. However, a free energy difference ΔF between atoms in adjacent grains was left as an undetermined parameter, which can vary greatly in magnitude by the circumstances. It is therefore uncertain whether the bubbles of such size as in Fig. 1 can still be swept up by the boundary or not. From the location of the experimental points in Fig. 2, which is regarded as of the bubbles left behind the migrating grain, ΔF is estimated to be larger than 10^{-16} erg/atom in our specimens.

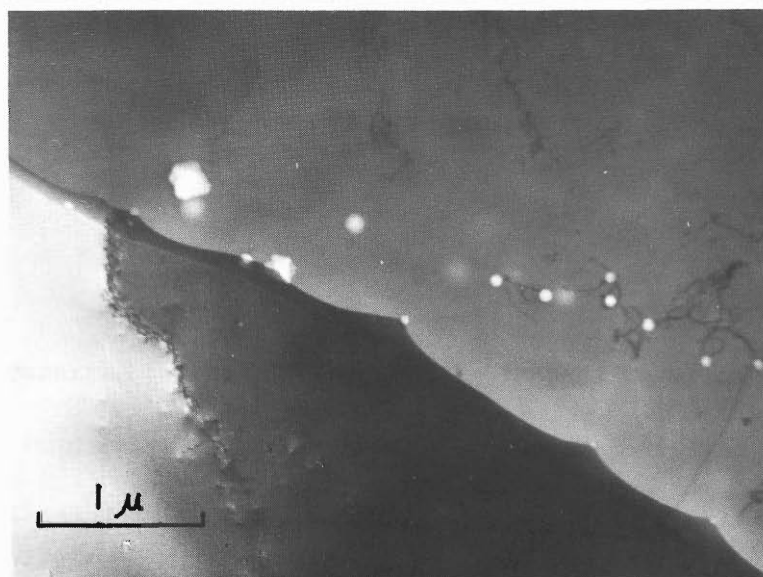


Fig. 1. Grain boundary bent by bubbles. (Observed in an annealed specimen for 1.5 h at 645°C, after deformation of 8 % tensile strain following 87 ppm He injection.)

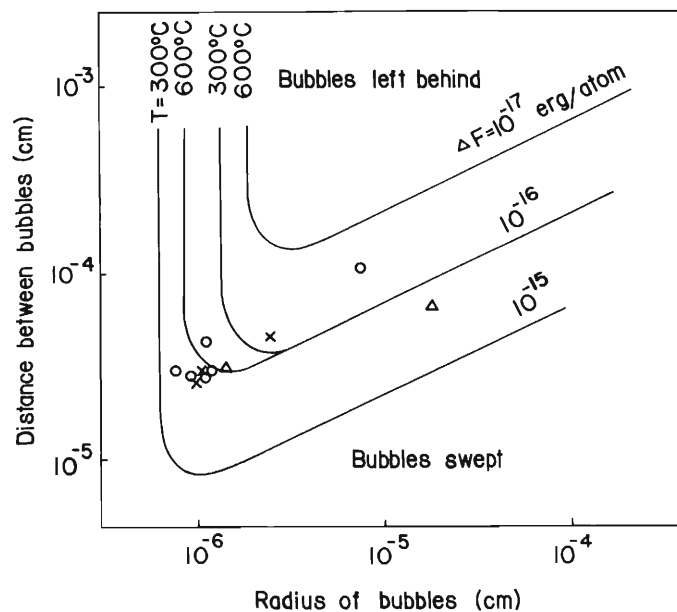


Fig. 2. Illustration of sweeping condition for bubbles calculated following Speight et al.³⁾ The bubbles on the upper side of the curve cannot follow the migration of the grain boundaries. (Experimental points were obtained by the authors²⁾ for specimens annealed at 600 °C; Δ , injected with 43 ppm He, \times , injected with 43 ppm He and deformed to 8 % tensile strain, o , injected with 87 ppm He.)

The radius of bubbles in question is 2×10^{-6} cm and the distance between them is 10^{-4} cm, so that they seem to locate in the region where they cannot follow the migrating boundary.

References

- 1) R.R. Hasiguti, E. Yagi, H. Sakairi, M. Kobayashi, and T. Karasawa: IPCR Cyclotron Progr. Rep., 4, 144 (1970).
- 2) H. Sakairi, E. Yagi, H. Shiraishi, T. Karasawa, and R.R. Hasiguti: *ibid.*, 5, 98 (1971).
- 3) M.V. Speight and G.W. Greenwood: *Phil. Mag.*, 9, 683 (1964).

10. RADIOISOTOPE PRODUCTION AND ITS APPLICATIONS

10-1. Production of Radioisotopes for Medical Use

T. Nozaki, T. Karasawa, M. Okano, A. Shimamura,
M. Iwamoto, T. Ido, and Y. Makide

Efforts have been made to increase the production yield for ^{18}F and ^{43}K , to prepare some ^{18}F -labelled organic compounds for injection into experimental animals, and to find a convenient process for the production of $^{197\text{m}}\text{Hg}$. Also, the facility for the inner bombardment has been improved.

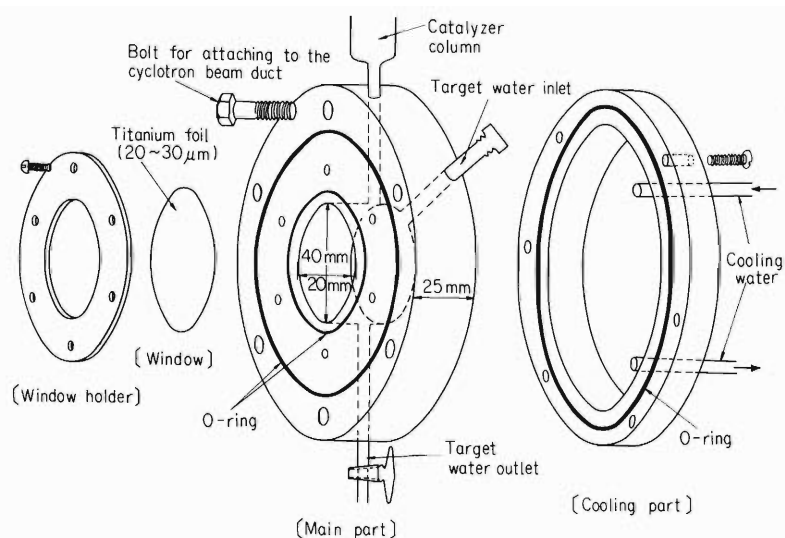


Fig. 1. Target assembly for the ^3He bombardment of water.

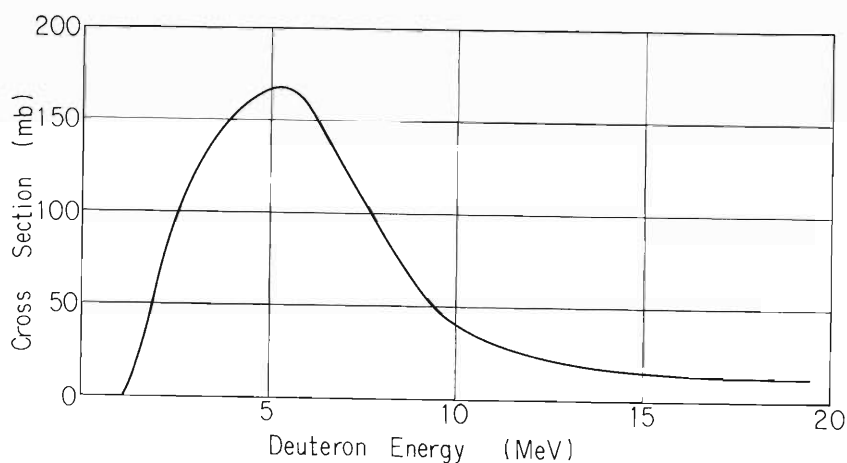


Fig. 2. Excitation curve for the $\text{Ne} + \text{d} \rightarrow ^{18}\text{F}$ reaction.

Figure 1 shows the target assembly for the production of carrier-free ^{18}F by the ^3He bombardment of water. The vessel is made entirely of titanium. Practically, about 60 mCi of ^{18}F ready for intravenous injection can be obtained routinely by this bombardment. The excitation curve for the $\text{Ne} + \text{d} \rightarrow ^{18}\text{F}$ reaction has been measured; it is shown in Fig. 2. We are, however, not as yet entirely sure in the shape of the curve in Fig. 2, and are continuing the measurement. The experimental results so far obtained suggest the presence of some fine structures in the deuteron energies of 8 to 10 MeV. It is now clear, regardless of the fine structures, that the thick target yield of ^{18}F is larger for the $\text{Ne} + \text{d}$ reaction than for the $\text{O} + ^3\text{He}$ reaction by a factor of about 1.5 for an equal beam current.

^{18}F -labelled p-fluorobenzoic acid and cholesteryl fluoride were prepared¹⁾ and injected into mice or rats, and the resultant distribution of the ^{18}F was measured. The results are shown in Figs. 3 and 4.

By the α -particle bombardment of an argon stream, ^{43}K has been produced. It has been found that more than 90 % of the ^{43}K formed in the stream is adsorbed within a glass bombardment vessel (about 1 m length, 6 cm diameter), when the streaming rate

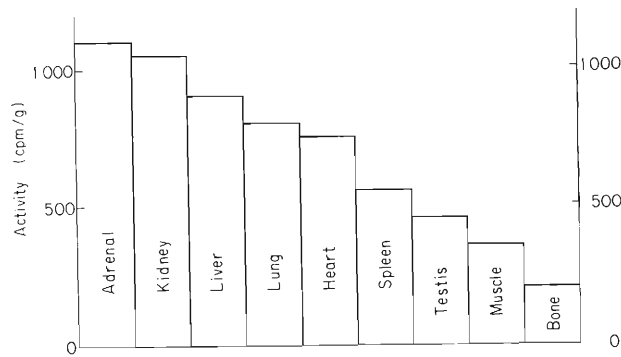


Fig. 3. Distribution of p-fluorobenzoic acid.

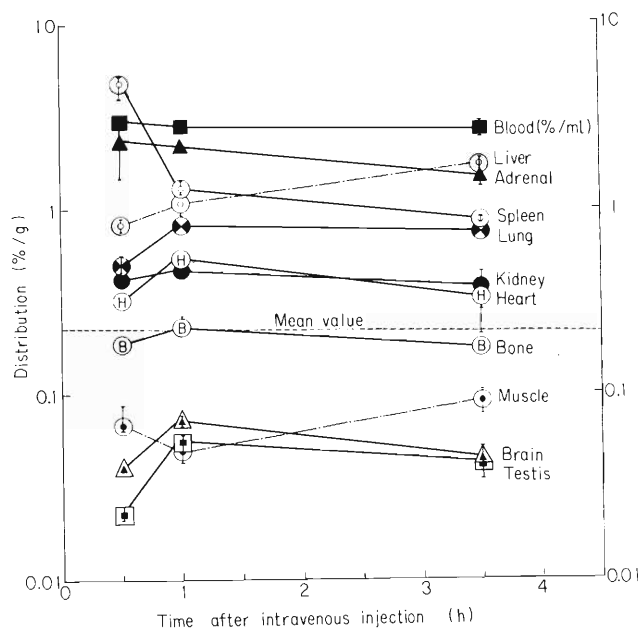


Fig. 4. Distribution of cholesteryl fluoride and its change with time.

is about 2 ℓ /min. The adsorbed ^{43}K has been shown to be eluted efficiently by the condensation of steam on the inside wall of the bombardment vessel. Thus, ^{43}K ready for intravenous injection is prepared with a yield of about 2 mCi/hr.

The excitation curve for the $^{197}\text{Au}(d,2n)^{197\text{m}}\text{Hg}$ reaction was roughly measured, and the separation of the $^{197\text{m}}\text{Hg}$ from the gold target was studied. For a 20 MeV deuteron beam, about 0.6 mCi of $^{197\text{m}}\text{Hg}$ has been shown to be formed per $\mu\text{A}\text{-hr}$, accompanied with a much smaller activity of ^{197}Hg . No noticeable loss of the product mercury from the gold target in the course of the bombardment has been found, and the separation yield of the radiomercury has proved to be over 90 % in our method.

Reference

- 1) T. Nozaki, A. Shimamura, and T. Karasawa: IPCR Cyclotron Progr. Rep., 2, 156 (1968).

11. RADIATION MONITORING

11-1. Routine Monitoring

K. Koda, I. Sakamoto, and I. Usuba

The results of routine monitoring on the IPCR cyclotron obtained from April 1971 to March 1972 are described.

1) Residual activities of the machine

Dose rates at the acceleration chamber were 100 mR/h on its outer surface and 5 R/h at the septum, 20 h after machine shutdown. An order of several mR/h was observed at the Q magnets of each beam course.

2) Leakage radiations

Measurements of leakage radiation were made using gamma-ray film badges and neutron pocket dosimeters at various points around the cyclotron room under the condition that a $^{147}\text{Sm}_2\text{O}_3$ target was bombarded by $9 \sim 10 \mu\text{A}$ ^3He beam of 38 MeV. Among the results obtained, it is worth mentioning that the dose rate in the vicinity of loop holes in the large experimental area was 3 mrem/day (gamma + neutron) and that at the entrance to the cyclotron room from the underground passage was 50 mrem/day where the contribution of gamma rays and neutron was 30 and 20 mrem/day, respectively.

3) Floor and air contamination

The surface contamination on the floor of the cyclotron room was kept about $10^{-5} \mu\text{Ci}/\text{cm}^2$ since the preceding period. Those of the experimental areas, hot laboratory, and chemical laboratories were of the order of $10^{-7} \mu\text{Ci}/\text{cm}^2$. On the inner surface of the acceleration chamber the contamination of $2 \times 10^{-2} \mu\text{Ci}/\text{cm}^2$ of tritium and $10^{-5} \mu\text{Ci}/\text{cm}^2$ of other beta- and gamma-emitters was found.

The tritium still remained in the acceleration chamber since the last tritium acceleration in December 1970. About $10^{-2} \mu\text{Ci}/\text{cm}^3$ of tritium concentration was found in the air within the chamber, and 8.4 mCi of tritium was recovered from the air by purging the chamber with fresh air and trapping the moisture in a water bubbler.

The tritium contamination of air in the cyclotron room ranged from 10^{-5} to $10^{-6} \mu\text{Ci}/\text{cm}^3$.

4) Personnel monitoring

The values of accumulated dose of external exposure during the present period of all cyclotron workers issued with the gamma-neutron film badge are shown in Table 1. The average annual dose per person was 261 mrem and is decreasing year by year. The main reason is the reduction of work time for high-level operations such as septum replacement.

About 60 mrem of thermal neutron exposure was observed for the first time since the start of cyclotron operation. The internal exposure of the workers to tritium was

reduced to almost zero by purging the air in the acceleration chamber completely before overhauling.

Table 1. Accumulated dose distribution of the cyclotron workers from April 1971 to March 1972.

Dose (mrem)	Undetectable	10~100	101~300	301~1000	>1000
Operators			3	4	
Nuclear physicists		6	8	4	
Accelerator physicists		1	3	2	
Physicists of other fields	1	5		1	1
Radiochemists	1	2	1	1	
Radiation chemists	2				
Biological chemists	2				
Health physicists	1	1			

Average annual dose per person : 261 mrem.

Maximum annual dose: 1360 mrem.

12. LIST OF PUBLICATIONS

- 1) T. Nomura and T. Yamazaki: "Effective Magnetic Moment and E2 Polarization Charge in $f_{7/2}$ Nuclei", 'The Structure of the $1f_{7/2}$ Nuclei' ed. R.A. Ricci (Editrice Compositori, Bologna, 1971) p. 437.
- 2) T. Nomura, T. Yamazaki, S. Nagamiya, and T. Katou: "Magnetic Moment of the Lowest 6^+ State in ^{42}Ca ", J. Phys. Soc. Japan, 33, 286 (1972).
- 3) T. Nomura, K. Hiruta, T. Inamura, and M. Odera: "In-Beam Alpha Spectroscopy of N=128 Isotones, Lifetimes of ^{216}Ra and a New Isotope ^{217}Ac ", Phys. Lett., 40B, 543 (1972).
- 4) J.I. Fujita, S. Yamaji, and M. Hirata: "Effects of Exchange Currents on Orbital g-Factor and E1 Sum Rule", J. Phys. Soc. Japan., 33, 541 (1972).
- 5) T. Kammuri, S. Kusuno, and S. Yamaji: "The Use of the Angular Momentum Projection Technique in Two-Nucleon Transfer Reactions on Deformed Nuclei", Phys. Lett., 39B, 327 (1972).
- 6) Y. Awaya, K. Matsuda, T. Wada, N. Nakanishi, S. Takeda, and S. Yamaji: "Inelastic Scattering of Protons from ^{100}Mo and ^{98}Mo ", J. Phys. Soc. Japan, 33, 881 (1972).
- 7) Y. Abe and N. Takigawa: "Stability and Persistency of α Cluster Structures" Prog. Theor. Phys. Suppl., 52 (1972).
- 8) Y. Miyazawa, I. Kohno, T. Tonuma, T. Inoue, A. Shimamura, and S. Nakajima: "A Source for Multiply-charged Ions and Acceleration of C, N and O Ions by IPCR Cyclotron", IEEE Trans. Nucl. Sci. NS-19, 105 (1972).
- 9) I. Kohno, Y. Miyazawa, T. Tonuma, T. Inoue, A. Shimamura, and S. Nakajima: "Production of Multiply-charged Ions of Ne, Ar, Kr and Xe by the Electron-bombarded Hot Cathode Ion Source of IPCR", IEEE Trans. Nucl. Sci., NS-19, 109 (1972).
- 10) K. Matsuda: "On the Acceleration of Heavy Ions in a Cyclotron", Sci. Papers I.P.C.R., 66, 33 (1972).
- 11) M. Odera and T. Tonuma: "A Variable Frequency Linac for Acceleration of the Low Energy Heavy Ions and its Use as a Prestripper Accelerator for a Separate Sector Cyclotron", Proc. 6th Intern. Cyclotron Conf., Vancouver (1972).
- 12) F. Ambe, H. Shoji, S. Ambe, M. Takeda, and N. Saito: "A Mössbauer Study of the Valence State of ^{119}Sn after EC Decay of ^{119}Sb in Antimony, Sb_2Te_3 and Sb_2S_3 ", Chem. Phys. Lett., 14, 522 (1972).

- 13) T. Nozaki, Y. Makide, Y. Yatsurugi, Y. Endo, and N. Akiyama: "Chemical Behavior of Carbon in High-purity Silicon in the Dissolution and Fusion of the Matrix", *Bull. Chem. Soc. Japan*, 45, 2776 (1972).
- 14) Y. Endo, Y. Yatsurugi, N. Akiyama, and T. Nozaki: "Infrared Spectrophotometry for Carbon in Silicon as Calibrated by Charged Particle Activation", *Anal. Chem.*, 44, 2258 (1972).

13. LIST OF PERSONNEL

Members of the Board

MIYAZAKI Yukio 宮崎友喜雄 (Chairman)	KAMITSUBO Hiromichi 上坪宏道
HAMADA Tatsuji 浜田達二	NAKANE Ryohei 中根良平
IMAMURA Masashi 今村 昌	ODERA Masatoshi 小寺正俊

Cyclotron Users Committee

HAMADA Tatsuji 浜田達二 (Chairman)	NOZAKI Tadashi 野崎 正
IMAMURA Masashi 今村 昌	SAITO Nobufusa 齋藤信房
KAMITSUBO Hiromichi 上坪宏道	SAKAIRI Hideo 坂入英雄
KARASAWA Takashi 唐沢 孝	SEKIZAWA Hisashi 関沢 尚
MATSUYAMA Akira 松山 晃	

Managers of Users Group

HAMADA Tatsuji 浜田達二	ODERA Masatoshi 小寺正俊
NOZAKI Tadashi 野崎 正	

IPCR Cyclotron Operating Personnel

Machine Group

HEMMI Masatake 逸見政武	SHIMAMURA Akira 島村 旻
INOUE Toshihiko 井上敏彦	TONUMA Tadao 戸沼正雄
MIYAZAWA Yoshitoshi 宮沢佳敏	

Operation

FUJITA Shin 藤田 新	NAKAJIMA Hisao 中嶋尚雄
IKEGAMI Kumio 池上九三男	TERAJIMA Osamu 寺島 為
KAGEYAMA Tadashi 影山 正	OGIWARA Kiyoshi 荻原 清
KOHARA Shigeo 小原重夫	

Scientific and Engineering Personnel

Cyclotron Lab.

CHIBA Yoshiaki 千葉好明	NAKANISHI Noriyoshi 中西紀喜
FUJISAWA Takashi 藤沢高志	NOJIRI (INANAGA) Tamaki 野尻多真喜
FUJITA Jiro 藤田二郎	NOMURA Toru 野村 亨
HASHIMOTO Osamu 橋本 治	ODERA Masatoshi 小寺正俊
HEMMI Masatake 逸見政武	SHIMAMURA Akira 島村 旻
HIRUTA Kotaro 蛙田幸太郎	TAKEDA Shigeru 竹田 繁
INAMURA Takashi 稲村 卓	TAKIGAWA Noboru 滝川 昇
INOUE Toshihiko 井上敏彦	TONUMA Tadao 戸沼正雄
KAMITSUBO Hiromichi 上坪宏道	TOYAMA Manabu 外山 学
KARASAWA Takashi 唐沢 孝	YAMAJI Shuhei 山路修平
KOHNO Isao 河野 功	YAMAZAKI Yoshishige 山崎良成
MIYAZAWA Yoshitoshi 宮沢佳敏	YOSHIDA Fusako 吉田房子
MOTONAGA Shoshichi 元永昭七	YOSHIE Morio 吉江森男
NAKAJIMA Shunji 中島諄二	WADA Takeshi 和田 雄

(Visitors)

EJIRI Hiroyasu 江尻宏泰 (Univ. of Osaka)
 FUJINO Takeo 藤野武夫 (Inst. Nucl. Study, Univ. of Tokyo)
 FUJITA Junichi 藤田純一 (Tokyo Univ. of Educ.)
 HANAZONO Sakae 花園栄 (INS, Univ. of Tokyo)
 IMANISHI Bunryu 今西文竜 (Nihon Univ.)
 KOIKE Masahiro 小池正宏 (INS, Univ. of Tokyo)
 LIN Ching Liang 林清涼 (Univ. of Formosa)
 MIKUMO Takashi 三雲昂 (Tokyo Univ. of Educ.)
 MATTHIAS, E. (Freie Univ. Berlin, West Germany)
 NAGAMIYA Shoji 永宮正治 (Dept. Phys., Univ. of Tokyo)
 NAKAI Koji 中井浩二 (Dept. Phys., Univ. of Tokyo)
 OHNUMA Hajime 大沼甫 (INS, Univ. of Tokyo)
 PINGEL, K. (Max-Planck-Inst. Für Kernphysik Heidelberg, West Germany)
 RECKNAGEL, E. (HAHN-MEITNER Inst. f. Kern Forschung GmbH u. Freie Univ
 Berlin, West Germany)
 SEKIGUCHI Masayuki 関口雅行 (INS, Univ. of Tokyo)
 YAMANE Isao 山根功 (Res. Center Nucl. Sci. and Tech. Univ. of Tokyo)
 YAMAZAKI Toshimitsu 山崎敏光 (Dept. Phys., Univ. of Tokyo)
 YAZAKI Koichi 矢崎紘一 (Dept. Phys. Univ. of Tokyo)

Radiation Lab.

AWAYA Yohko 粟屋容子	KUMAGAI Hidekazu 熊谷秀和
HAMADA Tatsuji 浜田達二	OKANO Masaharu 岡野真治
HASHIZUME Akira 橋爪朗	TAKAHASHI Tan 高橋旦
KATOU Takeo 加藤武雄	TENDOW Yoshihiko 天道芳彦
KONNO Satoshi 金野智	

(Visitors)

NAGAHARA Teruaki 永原照明 (Rikkyo Univ.)
 ANDO Jun 安東醇 (Kanazawa Univ.)
 DOKE Tadayoshi 道家忠義 (Waseda Univ.)
 SUZUKI Kazuaki 鈴木一明 (Japan Anal. Chem. Res. Inst.)

Nuclear Analytical Chemistry Lab.

AMBE Fumitoshi 安部文敏	MAKIDE Yoshihiro 卷出義紘
AMBE Shizuko 安部静子	NOZAKI Tadashi 野崎正
ARATANI Michi 荒谷美智	SAITO Nobufusa 斎藤信房

(Visitors)

AKIYAMA Nobuyuki 秋山信之 (Komatsu Electronic Metals Co., Ltd.)
 IDO Tatsuo 井戸達雄 (Nat. Inst. of Radiological Sciences)
 FUKUSHI Kiyoshi 福士清 (Nat. Inst. of Radiological Sciences)
 YATSURUGI Yoshifumi 八剣吉文 (Komatsu Electronic Metals Co., Ltd.)

Radiobiology Lab.

IGARASHI Kazui 五十嵐一茂	MATSUYAMA Akira 松山晃
KITAJIMA Yoshio 北嶋淑男	YATAGAI Fumio 谷田貝文夫

Radiation Chemistry Lab.

IMAMURA Masashi 今村 昌
KIMURA Kazuie 木村 一宇

MATSUI Masao 松井正夫

Metal Physics Lab.

HASIGUTI R. Ryukiti 橋口隆吉
KOYAMA Akio 小山昭雄
SAKAIRI Hideo 坂入英雄

SHIOTANI Nobuhiro 塩谷巨弘
YAGI Eiichi 八木栄一

(Visitors)

ISHINO Shiori 石野 梨 (Univ. of Tokyo)
MISHIMA Yoshitsugu 三島良績 (Univ. of Tokyo)
SHIRAIISHI Haruki 白石春樹 (Nat. Res. Inst. for Metals)

Magnetic Materials Lab.

OKADA Takuya 岡田卓也
OKAMOTO Shoichi 岡本祥一

SEKIZAWA Hisashi 関沢 尚

Radiation Monitors

KODA Kugao 甲田陸男
SAKAMOTO Ichiro 坂本一郎

USUBA Isao 薄葉 勲

(Editors of the Progress Report)

AMBE Fumitoshi 安部文敏
IMAMURA Masashi 今村 昌

ODERA Masatoshi 小寺正俊
SAKAIRI Hideo 坂入英雄

14. LIST OF OUTSIDE USERS AND THEIR THEMES

Description is in the order of theme, particle and energy used, users' name(s) institution, and number of times of use.

- 1) "Production of ^{43}K for Heart Diagnosis".
 α -29 MeV.
 M. Nakamura et al.,
 Med. Dept., Kyushu Univ. (5)
- 2) "Production of ^{52}Fe used for Diagnosis".
 ^3He -40 MeV.
 Y. Murakami et al.,
 Tokyo Metropolitan Univ. (3)
- 3) "Production of ^{76}Br for Study of Internal Conversion Electrons".
 α -41 MeV.
 T. Nagahara,
 Rikkyo Univ. (1)
- 4) "Production of ^{18}F for Tumor Search".
 ^3He , 18 ~ 21 MeV.
 H. Kakehi,
 Chiba Univ. Hospital,
 A. Tsuya,
 National Cancer Center Res. Inst.,
 H. Murayama,
 Tokyo Medical Univ. (8)
- 5) "Production of ^{197}Hg for Diagnosis of Lung Tumor".
 d -22 MeV.
 M. Iio and T. Hara,
 Nakano National Hospital. (2)
- 6) "Measurement of Excitation Function of the Reaction $^{54}\text{Fe}(\alpha, n)^{57}\text{Ni}$ ".
 α -25 MeV.
 S. Tanaka,
 Inst. Nucl. Study, Univ. of Tokyo. (1)
- 7) "Production of ^{123}I ".
 ^3He -40 MeV, α -40 MeV.
 O. Ezawa,
 Chem. Dept., Tokyo Metropolitan Univ. (8)
- 8) "Study of Effect of Helium Bubbles on the Mechanical Behavior of Stainless Steel, SUS 32".
 α -32, 35, 36 MeV.
 T. Katou, S. Kawasaki, and T. Furuta,
 Japan Atomic Energy Res. Inst. (7)

- 9) "Simulation Study by Charged particles of Neutron Damage of Reactor Materials".
p-6, 10 MeV (2); α -23, 34, 35 MeV (5).
H. Kamei and M. Terasawa,
Electrical and Nuclear Engineering Lab.,
Toshiba Research and Development Center.
- 10) "Production of ^{54}Mn as a temperature Indicator at the Nuclear Alignment Experiment".
p-15 MeV.
K. Nagamine and H. Koyama,
Phys. Dept., Univ. of Tokyo. (1)
- 11) "Production of ^{210}At for Study of Hyperfine Interaction of the Isomeric States of ^{210}Po ".
 α -42 MeV.
S. Nagamiya et al.,
Phys. Dept., Univ. of Tokyo. (1)
- 12) "Production of ^{111}In for Tumor Search".
 α -43 MeV.
H. Kakehi,
Chiba Univ. Hospital. (3)
- 13) "Study of Potassium Metabolism by ^{43}K ".
 α -29 MeV.
Y. Araki and M. Kashima,
Med. Dept., Univ. of Tokyo. (3)
- 14) "Study of Excited States of ^{76}Se and ^{124}Te ".
 α -43 MeV.
T. Nagahara,
Rikkyo Univ. (1)
- 15) "Production Study of ^{53}Mn ".
d-9.0, 10.0 MeV.
S. Umemoto and S. Shibata,
Chem. Dept., Kyushu Univ. (2)
- 16) "Production of ^7Be for Experimental Practice at the Highest Class of Radio-isotope School".
p-14 MeV.
K. Noguchi et al.,
Radio-isotope School,
Japan Atomic Energy Res. Inst. (2)
- 17) "Activation Analysis of Impurities in Silicon".
 ^3He -20 MeV.
K. Noguchi et al.,
Radio-isotope School,
Japan Atomic Energy Res. Inst. (1)

- 18) "Production of ^{55}Co for Study of Nuclear Magnetic Resonance Phenomena of Nuclei aligned at Liquid Helium Temperature"
p-17 MeV.
K. Nagamine,
Phys. Dept., Univ. of Tokyo. (1)
- 19) "Production of ^{52}Fe ".
 ^3He -40 MeV.
O. Ezawa et al.,
Radio-isotope School,
Japan Atomic Energy Res. Inst. (1)
- 20) "Production of $^{179\text{m}}\text{Hf}$ for study of E2-to-M1 Ratio in its Cascade Decay".
 α -33 MeV.
H. Kawakami,
Inst. Nucl. Study., Univ. of Tokyo. (1)
- 21) "Production of Tl Radio-isotopes for Medical Use".
 α -43 MeV.
J. Ando,
Med. Dept., Kanazawa Univ. (1)
- 22) "Measurements of Reaction Cross Sections of $^{66}\text{Sn}(\alpha, n)$, $(\alpha, 2n)$, and $(\alpha, \alpha n)$ ".
 α -25 MeV.
M. Furukawa,
Chem. Dept., Nagoya Univ. (1)
- 23) "Study of ^{148}Sm ".
p-17 MeV.
Y. Gohno and Y. Iriya,
Phys. Dept., Tokyo Inst. Tech. (1)

AUTHOR INDEX

- AKIYAMA Nobuyuki 秋山信之 106
- AMBE Fumitoshi 安部文敏 102,104
- AMBE Shizuko 安部静子 102,104
- ARATANI Michi 荒谷美智 99
- AWAYA Yohko 栗屋容子 70
- FUJISAWA Takashi 藤沢高志 12,30,33,37,45
- FUJITA Jiro 藤田二郎 47,92,96
- FUJITA Shin 藤田新 7
- HAMADA Tatsuji 浜田達二 70,87
- HARADA Kichinosuke 原田吉之助 49
- HASHIMOTO Osamu 橋本治 73,80,84
- HASHIZUME Akira 橋爪朗 66,70
- HASIGUTI R. Ryukiti 橋口隆吉 122,125
- HEMMI Masatake 逸見政武 7,12,21,96
- HIRATA Michihiro 平田道紘 47
- HIRUTA Kotaro 蛙田幸太郎 76,80
- IDO Tatsuo 井戸達雄 127
- IGARASHI Kazui 五十嵐一茂 114
- IKEGAMI Kumio 池上九三男 7,12
- IMAMURA Masashi 今村昌 108,110
- INAMURA Takashi 稲村卓 76,80
- INANAGA Tamaki 稲永多真喜 30,33,45
- INOUE Toshihiko 井上敏彦 5,7,96
- IWAMOTO Masako 岩本正子 127
- IZUMO Koichi 出雲光一 87
- KAGEYAMA Tadashi 影山正 7
- KAMITSUBO Hiromichi 上坪宏道 15,23,27,30,33,45,89
- KARASAWA Takashi 唐沢孝 108,110,114,119,122,125,127
- KATOU Takeo 加藤武雄 66,70,87
- KIKUCHI Mariko 菊地真理子 110
- KIMURA Kazuie 木村一字 110
- KITAJIMA Yoshio 北嶋淑男 114
- KODA Kugao 甲田陸男 130
- KOHARA Shigeo 小原重夫 7
- KOHNO Isao 河野功 20,23,27,89
- KOIKE Masahiro 小池正宏 30,33,45
- KOYAMA Akio 小山昭雄 122
- KUMAGAI Hidekazu 熊谷秀和 66,87
- Machine Group 2
- MAKIDE Yoshihiro 巻出義紘 127
- MASUI Kuniaki 増井邦明 37
- MATSUDA Kazuhisa 松田一久 37
- MATSUI Masao 松井正夫 108,110
- MATSUYAMA Akira 松山晃 114
- MATTHIAS E. 84
- MIKUMO Takashi 三雲昂 27,45
- MIYAZAWA Yoshitoshi 宮沢佳敏 7
- MIZOGUCHI Tadashi 溝口正 119

- MOTONAGA Shoshichi 元永昭七 12,37,96
- NAGAMIYA Shoji 永宮正治 73,84
- NAKAI Kozi 中井浩二 73,84
- NAKAJIMA Hisao 中嶋尚雄 7,96
- NAKAJIMA Shunji 中島諄二 23,27,43,89
- NAKANISHI Noriyoshi 中西紀喜 35,96
- NOMURA Toru 野村亨 73,76,80
- NOZAKI Tadashi 野崎正 106,127
- ODERA Masatoshi 小寺正俊 15,18,21,23,27,43,76,80,89
- OGIWARA Kiyoshi 荻原清 7
- OHNUMA Hajime 大沼甫 35
- OKADA Takuya 岡田卓也 119
- OKANO Masaharu 岡野真治 87,127
- OSHIMA Keichi 大島恵一 110
- PINGEL, K. 30
- RECKNAGEL, E. 84
- SAITO Nobufusa 斎藤信房 102,104
- SAKAGUCHI Harutaka 坂口治隆 37
- SAKAIRI Hideo 坂入英雄 122,125
- SAKAMOTO Ichiro 坂本一郎 130
- SEKIZAWA Hisashi 関沢尚 119
- SHIMAMURA Akira 島村旻 5,7,127
- SHIOTANI Nobuhiro 塩谷亘弘 119
- SHIRAISHI Haruki 白石春樹 125
- SUEKANE Shota 末包昌太 49
- TABATA Yoneho 田畑米穂 110
- TAKAHASHI Tan 高橋旦 114
- TAKEBE Hideki 武部英樹 12
- TAKEDA Shigeru 竹田繁 35,43,92,96
- TAKIGAWA Noboru 滝川昇 58
- TENDOW Yoshihiko 天道芳彦 66,70,87
- TERAJIMA Osamu 寺島為 7
- TONUMA Tadao 戸沼正雄 7,18
- TOYAMA Hinako 外山比南子 35
- TOYAMA Manabu 外山学 53
- USUBA Isao 薄葉勲 130
- WADA Takeshi 和田雄 30,33,45
- YAGI Eiichi 八木栄一 122,125
- YAMADA Satoshi 山田総 35
- YAMAJI Shuhei 山路修平 37,47,49
- YAMANE Isao 山根功 23,27,89
- YAMAZAKI Toshimitsu 山崎敏光 73,84
- YAMAZAKI Yoshishige 山崎良成 73,84
- YATAGAI Fumio 谷田貝文夫 114
- YATSURUGI Yoshifumi 八剣吉文 106
- YOSHIDA Fusako 吉田房子 18,37
- YOSHIE Morio 吉江森男 23,27,89

IPCR Cyclotron Progress Report

理化学研究所サイクロトロン年次報告 第6巻 (1972)

印刷 昭和48年(1973)3月25日

発行 昭和48年(1973)3月30日

発行者 理化学研究所

代表者 星 野 敏 雄

351 埼玉県和光市広沢2番1号

電話(0484)62-1111

編集者 理化学研究所サイクロトロン運営委員会

委員長 浜 田 達 二

印刷所 丸 星 印 刷 株 式 会 社

101 東京都千代田区

神田神保町1丁目42番地

定価 2,000円

理化学研究所

埼玉県 和光市 広沢